**Energy Conversion from Gradients across Bio-Inspired Membranes**

by

Thomas Byron Hipps Schroeder

A dissertation submitted in partial fulfillment
of the requirements for the degree of
Doctor of Philosophy
(Chemical Engineering)
in the University of Michigan
2017

Doctoral Committee:

Professor Michael Mayer, Adolphe Merkle Institute, Co-Chair
Professor David Sept, Co-Chair
Professor Erdogan Gulari
Professor Ronald G. Larson
Professor Jens-Christian Meiners
Professor Max Shtein

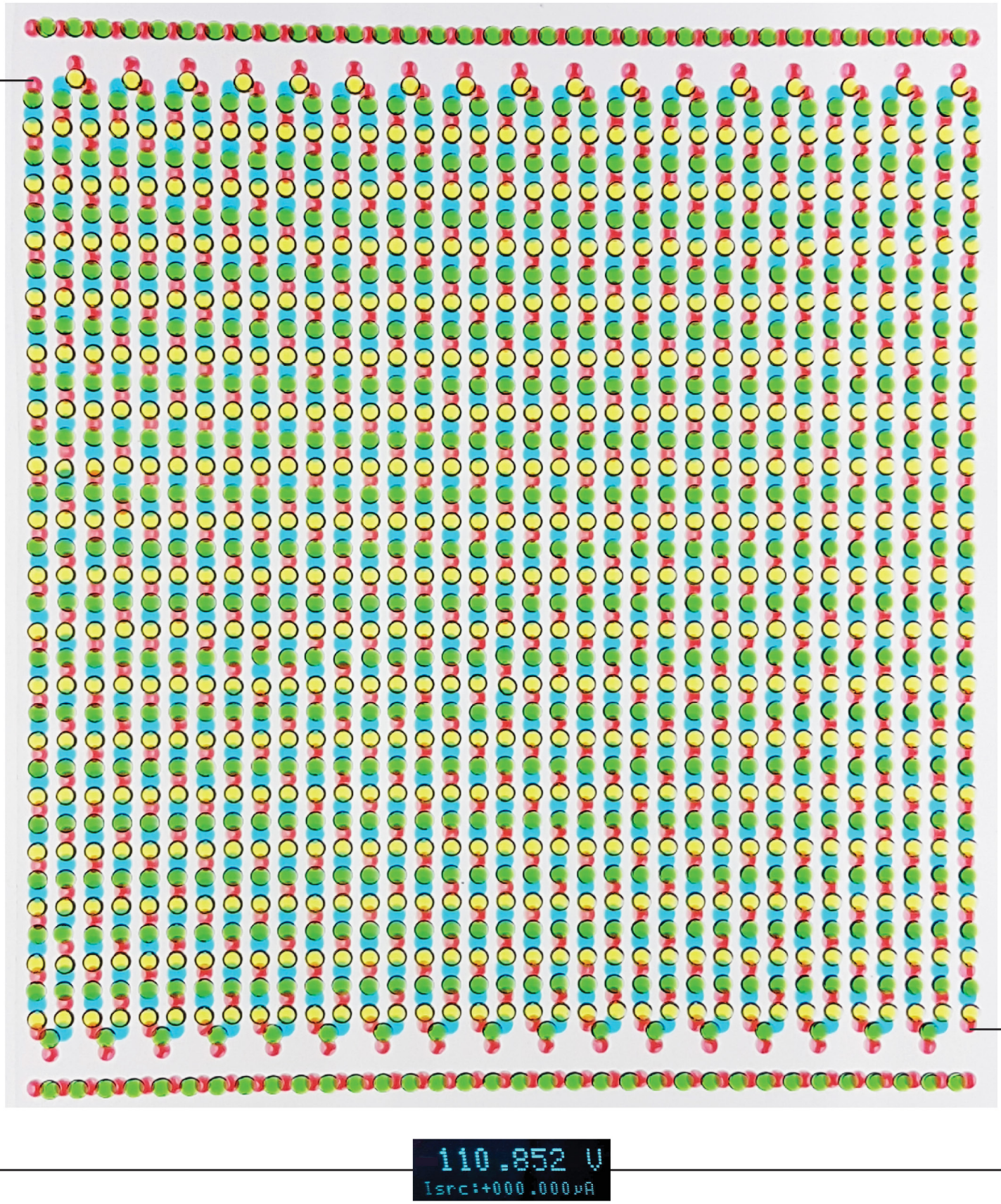
110.852 V
Isrc:+000.000nA

Thomas B. H. Schroeder

tomschro@umich.edu

ORCID iD: 0000-0003-2795-1730

## ACKNOWLEDGMENTS

The work presented in this dissertation was funded by a National Science Foundation EFRI-BSBA grant (#0937323), an Air Force Office of Scientific Research grant (#FA9550-12-1-0435), the National Institutes of Health (grant #T32GM008353) via the University of Michigan's Cellular Biotechnology Training Program, and the Adolphe Merkle Institute.

Many people have provided me with help and guidance over the course of my Ph.D. In particular, I would like to thank:

My advisor, Prof. Michael Mayer, who shaped me into the scientist I am today. His enthusiasm for science is boundless and contagious, and I've learned many lessons from his expertise, leadership, and creative vision. Our discussions over the past five years have been thought-provoking, motivating, and a lot of fun. Michael also offered me the life-changing opportunity to move to Switzerland with his research group; the past two years in Fribourg have been a fantastic adventure that has broadened my horizons and connected me with a global community of scientists.

My co-advisor, Prof. David Sept, who has been another constant source of guidance, and who assisted with the statistical analyses and molecular dynamics simulations in this dissertation.

My other collaborators, including Profs. Max Shtein, Jerry Yang, Kon-Well Wang, and members of their respective groups, who have all been a pleasure to work with and provided valuable advice along the way.

Profs. Jens-Christian Meiners, Ronald Larson, and Erdogan Gulari, who form the remainder of my dissertation committee, for taking the time to review this thesis and evaluate my progress at several meetings over the years.

The Whitesides group (particularly Filip Ilievski), who provided us with the soft robot featured in Chapter 2.

The Mycek group, who let me use their spectrofluorometer for the work in Chapter 3.

Profs. Barbara Rothen-Rutishauser and Alke Petri-Fink, whose 3D bioprinter enabled the high-voltage iteration of the artificial electric organ presented in Chapter 4. Additionally, Fritz

Bircher's iPrint lab at the Haute École d'Ingénierie et d'Architecture Fribourg, particularly Florian Bourguet and Mathieu Soutrenon, graciously donated time towards adapting a printer for our use and helped us understand the intricacies of microvalve printing systems. We also used the laser cutter at Fablab Fribourg, a wonderful community makerspace.

Everyone involved with the Cellular Biotechnology Training Program, which provided me with two years of funding, a community of peers in the biological sciences, and the opportunity to spend a summer working in industry -- an invaluable experience for an academic to have. In particular, Prof. Andrew Putnam, who coordinates the program, has been a reliable source of counsel over the years, and his course on cellular biotechnology provided valuable context about various ways in which contemporary scientists make their way in the "real world."

Everyone at Sophion, the biotechnology company in Copenhagen where I spent the summer of 2015. In particular, I'd like to thank Morten Sunesen for deciding to take a chance on me as an intern after we met at a Biophysical Society meeting, my supervisor Sandra Wilson for her support of my project, and Peder Skafte-Pedersen, Lasse Homann, Mette Christensen, and Sune Hørlück for advising me along the way. During this time, Prof. Bo Wegge Laursen at the University of Copenhagen also generously lent me lab space for a side project; Marco Santella helped me out while I was there.

Prof. Charles Monroe, one of the most extraordinarily gifted instructors to ever have taught me. His lectures on transport and mathematics presented difficult material with clarity, thoroughness, and a logical progression; I have referred back to the slides and videos from the three courses I took with him many times over the course of my Ph.D.

Prof. Phillip Savage, who served as the department's graduate chair when I joined. I first met him during my senior year of college after being accepted to the program; during this meeting, he gave me the very strong impression that the department seemed like a friendly and welcoming place to be, which played no small part in my decision to attend U of M.

All the staff members who have helped me out over the course of the past five years. Susan Hamlin, Nancy Paskievitch, and Susan Douglas at Michigan and Catherine Jungo at AMI have all been particularly helpful and accommodating.

Everyone at the Adolphe Merkle Institute, which is a friendly community of scientists from all over the world with diverse research interests and scientific backgrounds. The past two years have been some of the most productive of my career, and this has been enabled in part by

the access to various kinds of expertise and ideas that the institute provides. It's been a great place to work.

Brandon Bruhn, for serving as an important scientific mentor and good friend during my first several years in the Mayer group. I've learned a lot from Brandon's drive, rigor, and engineering skills; I'm lucky to have had him as a role model.

Gogol Guha, Olivia Eggenberger, and Jared Houghtaling, fellow Ph.D. students who all moved with me from Ann Arbor to Fribourg. The transition was a lot easier because we all made it together. In particular, Gogol and I worked together for years on the project discussed in Chapter 4 of this thesis, and I've never had a more fun or productive working partnership.

The undergraduates, high school students, and interns who have all tolerated me as a mentor on various projects, including Kathryn Haengel, Claire Wang, Mitchell Johnson, Sarah Grunsfeld, and Sandra Stangeland-Molo.

All the rest of my colleagues in the Mayer group, including Erik Yusko, Haiyan Liu, Nikita Lomis, Anirudh Vinnakota, Aziz Fennouri, Simon Mayer, Julie Ducrey, Lennart de Vreede, Cuifeng Ying, Jonathan List, Peter Nirmalraj, and Saurabh Awasthi. Thanks for making the group a great environment.

All the great friends I've made in Ann Arbor, Fribourg, and elsewhere, who are too numerous to list here but who have brought me immeasurable joy.

Finally, I'd like to thank my parents, who have been overflowing with love and support every step of the way – even when their son broke the news that he wanted to finish his Ph.D. on the other side of the Atlantic! Without their wisdom, encouragement, and love, I would not be the person I am today.

## PREFACE

"If these tremendous events are random combinations of matter run amok, the yield of millions of monkeys at millions of typewriters, then what is it in us, hammered out of those same typewriters, that they ignite? We don't know. Our life is a faint tracing on the surface of mystery, like the idle, curved tunnels of leaf miners on the face of a leaf. We must somehow take a wider view, look at the whole landscape, really see it, and describe what's going on here. Then we can at least wail the right question into the swaddling band of darkness, or, if it comes to that, choir the proper praise."

- Annie Dillard, *Pilgrim at Tinker Creek*

## TABLE OF CONTENTS

## LIST OF TABLES

## LIST OF FIGURES

## ABSTRACT

Membranes are fundamentally important barriers that enable the processes of life by slowing the dissipation of gradients and transducing usable energy from entropic driving forces. This dissertation presents three investigations of gradient equilibration across bio-inspired membranes, with a focus on permeability and geometric considerations in membrane-based energy transduction systems.

The first study models the dynamics of pressure generation from osmotic gradients in an expandable compartment based on mass transport principles. Using an osmotic working fluid composed of aqueous polyethylene glycol inside commercially available dialysis cassettes whose membranes exclude polymer solutes, we validated this model and explored the importance of cassette geometry, restrictions on expansion, and membrane porosity characteristics on pressure generation rates over time. The model made it possible to predict the kinetics of nastic motions caused by osmotically-induced shifts in turgor pressure in plants such as *Mimosa pudica*; the model's projections based on plant cell dimensions agree well with published time scales. These cassettes are "waterable" pressure generators available to the general public; we demonstrated their utility by actuating a soft robotic gripper and published our characterization algorithm as an open-source tool.

The second study investigates the relationship between the chemical structures of a class of tethered membrane-spanning lipids found in hyperthermoacidophilic archaea and the proton/hydroxide permeability of self-assembled monolayer membranes that the lipids form. We

determined permeability values by measuring the fluorescence of solutions of liposomes containing pH-sensitive dyes over time after a step change in the external pH. The presence of isoprenoid methyl groups led to reductions in permeability values, and the length of the transmembrane tether unexpectedly displayed a direct correlation with the permeability, leading us to speculate about the importance of hydrophobic crowding in the membrane interior. Surprisingly, the presence of a transmembrane tether had no significant effect on the permeability at room temperature. We observed a strong positive correlation between the permeability of a membrane and the probability of observing water molecules spontaneously clustering inside the hydrophobic region of a simulated membrane of identical composition using molecular dynamics, providing a predictive parameter obtainable without any "wet" experimentation that may be useful for the design of membrane compositions with specific permeability characteristics.

The third study presents a novel hydrogel-based reverse-electrodialytic energy transduction scheme inspired by the electric eel. As in the biological system (but unlike traditional batteries), the "artificial electric organ" presented here is a soft, flexible, potentially biocompatible means of generating electricity using only a repeating arrangement of ionic gradients across selective membranes. The artificial electric organ generates numerous additive voltages at the same time in order to produce a large transient electric signal; while the biological system accomplishes this synchronicity through neural signaling, the artificial setup uses geometries that allow simultaneous mechanical registration of the gels. This scheme is flexible enough that we were able to implement it in three distinct ways: fluidically, through the printing of large arrays (enabling the generation of over 100 V), and using a *Miura-ori* folding geometry that assembles planar films, which achieved a power density of 27 mW $m^{-2}$.

The work presented here draws inspiration from biological systems and earlier industrial efforts to extract electrical power from salinity gradients. Membrane-based strategies are well-suited for the local generation of usable energy on small scales and may be useful in the microelectromechanical systems and implantable devices of the future.

# CHAPTER 1

## Introduction

Self-assembled lipid membranes are among the most important structural motifs in biology. They are present in every living organism and are perhaps best-known as the primary structural component of the cellular envelope, which serves as an important physical boundary between cells and their environment. Less obviously, biological membranes have another fundamentally important function as energy transduction mechanisms. On the most basic level, a membrane serves to separate two regions and mediate the exchange of molecules and energy between those regions. When the two regions differ in chemical concentration, pressure, or electrical potential energy (or more generally in their *chemical potential*, which combines these effects), the energy gradient manifests as forces, which cause fluxes that bring the system toward equilibrium. Molecular machines in biological membranes are able to harness these driving forces to perform work.[1]

The importance of membrane-based energy storage and conversion in biology cannot be overstated. Two examples of this general scheme are mostly responsible for the manner in which all energy flows between living organisms. In photosynthesis, chlorophyll-bearing membrane proteins harness sunlight to build up a gradient of protons; another membrane protein uses the energy from the diffusion of protons down this gradient in order to synthesize adenosine triphosphate (ATP), the "energy currency" of cells, which is later used to convert atmospheric $CO_2$ into organic matter.[2] In cellular respiration, another ATP-producing proton gradient is

formed using the energy from metabolizing the organic matter produced by photosynthesis; the resulting ATP is used for vital biological functions. These mechanisms provide organisms with energy in a robust manner distributed throughout the body; humans turn over approximately their own body weight of ATP every day.[3] The consequences of these processes extend beyond biology: photosynthesis is responsible for the existence of oxygen in the Earth's atmosphere as well as most of the organic matter on the planet.[4–6]

Given the ubiquity and significance of biological membrane systems as gradient-supporting energy storage mechanisms, they are worth our attention both in the study of biology and as templates for engineered innovations, particularly in light of the growing need for sustainable energy sources. In the nearly 4 billion years since life began in the oceans, evolution by natural selection has driven the development of a wide variety of incrementally optimized solutions that allow fitness despite an array of threats from the environment and other organisms.[7] I have found the notion that biology offers problem-solving insight to those who pay attention to be one of the most compelling themes driving my career thus far.

This dissertation presents three projects that each characterize the equilibration of gradients across bio-inspired membranes; further, two of the three implement these membranes as energy transducers. The remainder of this first chapter is intended to describe the theory and the background literature pertinent to the chapters that follow.

## 1.1 The physics of gradient equilibration across membranes

The thermodynamic properties used to characterize systems can be classified as extensive or intensive. *Extensive* quantities, such as volume, number of molecules, and charge, each describe or depend on the size of the system. Each has a corresponding *intensive* quantity

(pressure, chemical potential, and electrical potential, respectively) that is independent of system size; the quantities are paired such that the product of each pair has units of work. The first and second laws of thermodynamics dictate that *gradients of intensive quantities between connected systems drive flows of the corresponding extensive quantities until equilibrium is reached*. Transport theory connects these thermodynamic (entropic) driving forces to the kinetics of equilibration using constitutive equations called *flux laws*. Flux, expressed as *j*, is the area-normalized rate of flow of an extensive quantity and is typically linearly dependent on the gradient(s) of the intensive quantity or quantities. In the context of membranes, flux laws are often simplified by assuming the intensive quantities in question to be constant in the bulk solution on either side of the membrane and by only considering gradients and fluxes in the direction normal to the membrane.[8]

A very basic example of a flux law is shown by the Hagen-Poiseuille formula, Equation 1.1, which describes laminar flow of water (or any incompressible fluid) through a cylindrical pipe in response to a pressure difference:

$$J_v = \frac{\pi a^4}{8\eta l}\Delta p \tag{1.1}$$

where $J_v$ ($m^3$ $s^{-1}$) is the volumetric flow rate of the fluid through the pipe, $a$ (m) is the pipe's radius, $\eta$ (Pa s) is the pipe's viscosity, $l$ (m) is the pipe's length, and $\Delta p$ (Pa) is the pressure difference between the two ends.[9] Applying this relation to the context of a membrane of thickness $l$ with cylindrical pores of radius $a$ at a density of $n$ pores per $m^2$ gives Equation 1.2:

$$j_v = \frac{\pi a^4 n}{8\eta l}\Delta p = L_p \Delta p \tag{1.2}$$

where $j_v$ (m $s^{-1}$) is the volumetric flux (an area-normalized expression of $J_v$ above) and $L_p$ (m $Pa^{-1}$ $s^{-1}$) is the hydraulic permeability, a material property that accounts for the pore characteristics and the viscosity of water.[9]

Equation 1.2 describes water fluxes resulting from gradients of hydrostatic pressure, but the formulation can be extended in the case where the solution on one side of the membrane contains solute molecules that are too large to pass through the membrane's pores. According to the so-called molecular kinetic theory of osmosis, in this scenario the membrane exerts a force on the solute molecules that collide with it during normal Brownian motion, providing the solute with momentum away from the membrane that is dissipated through viscous interactions into the solution as a whole. Solvent from the other side of the membrane freely crosses the membrane in response to the resulting local pressure drop, building up the bulk hydrostatic pressure of the compartment until the force exerted by the membrane is balanced.[1,9,10] This driving force is expressed as the osmotic pressure $\Pi$ (Pa) and obeys the van't Hoff relation (Equation 1.3) in dilute solutions of non-polymeric solutes, which makes the connection to thermal motion explicit:

$$\Pi = k_B T c_{solute} \tag{1.3}$$

where $k_B$ (J $K^{-1}$) is the Boltzmann constant, $T$ (K) is temperature, and $c_{solute}$ is the concentration of the solute (molecules $m^{-3}$).[10] A gradient in osmotic pressure can be expressed alongside a gradient in hydrostatic pressure in the flux law (Equation 1.4) as another force that drives the flux of solvent:

$$j_v = L_p(\sigma \Delta\Pi - \Delta p) \tag{1.4}$$

where $\sigma$ (dimensionless) is the osmotic reflection coefficient, a measure of the membrane's selectivity against of the solute.[9] When the membrane completely rejects solute passage, $\sigma$ = 1, while a membrane that cannot discriminate at all between the solute and solvent has $\sigma$ = 0, collapsing the flux law back to Equation 1.2. Equation 1.4 is the central flux law in Chapter 2 of this work.

Flux laws describe the movement of solutes as well as solvents in response to various gradients. Fick's first law, which can be derived completely from a statistical consideration of Brownian motion,[9] describes the flux ($j_s$, mol $m^{-2}$ $s^{-1}$) of solute *s* in response to a concentration gradient. When formulated in a membrane context (Equation 1.5), replacing the familiar diffusion coefficient *D* ($m^2$ $s^{-1}$) with a membrane permeability $P_s$ (m $s^{-1}$) according to $P_s = KD/l$ where *K* (dimensionless) is the solute partition coefficient into the membrane and *l* (m) is the membrane's thickness, Fick's first law becomes nearly identical to Equation 1.2:

$$j_s = P_s \Delta c_s \tag{1.5}$$

where $c_s$ (mol $m^{-3}$) is the concentration of the solute;[2] this is the primary flux equation appearing in Chapter 3. Kohlrausch's law (Equation 1.6), which relates the flux of charged solutes to a gradient in electrical potential, looks quite similar as well:

$$j_s = \frac{u_s c_s}{l} \Delta\varphi \tag{1.6}$$

where $u_s$ ($m^2$ $V^{-1}$ $s^{-1}$) is the electrical mobility of *s* in the membrane (another repackaged diffusion coefficient containing charge information), *l* is the membrane thickness, and $\Delta\varphi$ is the electrical potential difference across the membrane. (This linear relationship is consistent with Ohm's law).[11] Combining Equations 1.5 and 1.6 yields the Nernst-Planck equation (Equation 1.7):

$$j_s = P_s \left( \Delta c_s + \frac{F z_s}{RT} c_s \Delta\varphi \right) \tag{1.7}$$

where *F* (C $mol^{-1}$) is the Faraday constant, *R* (J $K^{-1}$ $mol^{-1}$) is the gas constant, and $z_s$ (dimensionless) is the valence of the solute. The Nernst-Planck equation has fundamental implications in the contexts of electrophysiology and ion exchange across semipermeable membranes,[11,12] which are both explored further in Chapter 4 of this work.

In each of the cases listed above, a transport rate across a membrane is linearly related to its driving gradient by a permeability factor. Measuring and comparing this material property is therefore central to characterizing permeation across both biological and synthetic membranes. Geometric parameters are also important to this end. The permeability factors contain some geometric considerations such as membrane thickness and porosity; additionally, when considering the rate at which a system is being brought to equilibrium by flux of an extensive parameter, one must consider the general continuity equation (Equation 1.8):

[*Accumulation rate over time*] = [*Inflow rate*] – [*Outflow rate*] + [*Generation rate*] (1.8)

In the absence of generation, the rate at which an extensive parameter accumulates in a system is governed by absolute flow rates, which require multiplying flux by membrane area. In the case of concentration gradients, the extensive parameter in question (number of molecules) is normalized by volume, making the surface-area-to-volume ratio of a membrane-enclosed system a critical parameter for estimating the time scale of equilibration. As the surface-area-to-volume ratio of a sphere is inversely proportional to its radius, cells (which typically have dimensions on the scale of microns) are well-constructed for quick equilibration.

We are interested in the rate at which work can be performed by the flux across the membrane. This quantity is generally obtainable by multiplying the flux of an extensive quantity by its driving force again, which returns an area-normalized power density ($W$, W $m^{-2}$). This equation typically takes the form of Equation 1.9:[13]

$$W = J_x \Delta Y = P_x (\Delta Y)^2 \quad (1.9)$$

where $J_x$ is the flux of an extensive quantity across a membrane, $\Delta Y$ is the driving gradient of the corresponding intensive quantity, and $P_x$ represents a permeability. This form is particularly familiar when the intensive quantity is electrical potential, the extensive quantity is charge, the flux is current, and the permeability is electrical conductivity.

## 1.2 Industrial-scale power generation from salinity gradients

The use of large-scale membrane-based energy transduction to contribute electricity to a power grid has been considered for a long time. Interest has particularly grown in recent decades as anthropogenic climate change, pollution, increasing demand, and dwindling petrochemical resources have provided incentives for the development of sustainable energy sources. Selective membranes allow engineers to generate power from any chemical potential difference arising between two reservoirs or streams. An obvious such difference can be found wherever a river meets the ocean – such sites are nicknamed "silent waterfalls," as they dissipate energy equivalent to approximately 270 m of hydraulic head as waste heat without any fanfare or practical utility.[13] The annual global river discharge is $3.7 \times 10^{13}$ cubic meters of fresh water;[14] from this, it has been estimated that an upper limit of around 2.6 TW of energy could theoretically be extracted,[15] enough to meet the world's energy demands as of 2011.[16]

In 1954, Pattle first published the idea of using selective membranes to extract energy from the gradient in chemical potential between river and ocean water.[17] Though a few patents followed,[18,19] publishing on this topic largely fell dormant until the 1973 oil crisis, whereupon interest in the idea bloomed. During this period, two major strategies were developed that use semipermeable membranes to extract energy from salinity gradients. The most thoroughly considered of these is pressure retarded osmosis (PRO), which exploits the difference in osmotic

pressure between two streams to perform mechanical work. The other, reverse electrodialysis (RED), takes advantage of the mutual dependence of concentration and potential when considering the flux of charged particles (Equation 1.7) in order to generate electrical current directly. Both of these technologies were developed as the reverse of filtration processes that consume energy in order to concentrate a solute; membranes developed from these processes were already available and could be used for energy extraction.[13,20] I will review these technologies here, both because they are among the first examples of artificial power generation from chemical gradients and because they harness the same driving forces as I consider in this dissertation using similar semipermeable membranes.

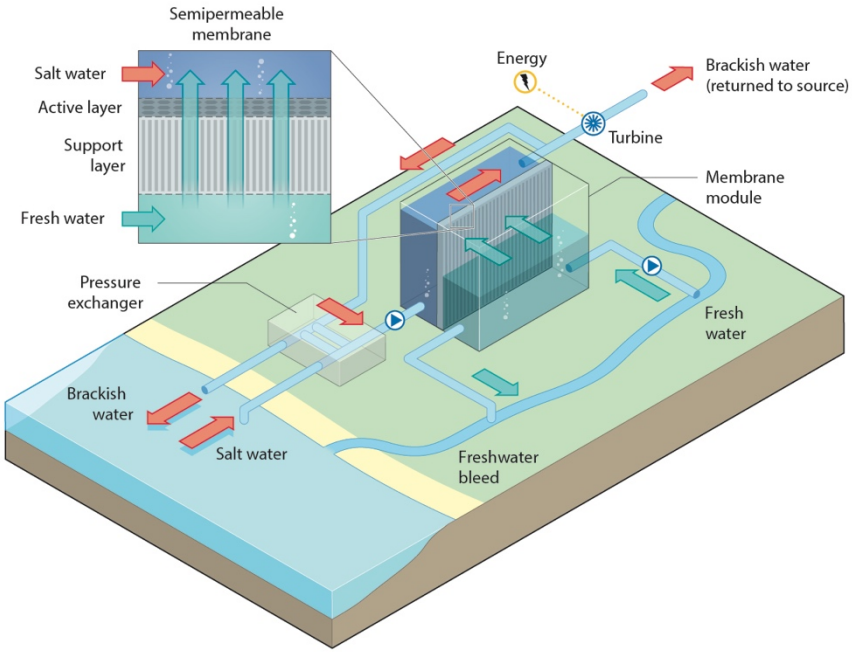


**Figure 1.1.** Process diagram of pressure retarded osmosis (PRO); see main text for description. Reprinted by permission from Macmillan Publishers Ltd: *Nature*,[21] copyright 2012.

PRO was first proposed in 1974 by Norman;[22] the first experimental results were published two years later by Loeb *et al.*[23] A scheme of the PRO process is shown in Figure 1.1. In this process, a porous salt-excluding membrane separates streams of fresh and salt water; the

osmotic pressure difference between the two streams creates a hydrostatic head according to Equation 1.4, which is used to turn a turbine or water wheel that produces electric power.[13,24] During initial studies, the membranes used were made for the opposite process, a desalination scheme known as reverse osmosis in which a pressure is applied to a reservoir of salt water on one side of a salt-sieving membrane, overcoming the osmotic pressure to extract pure water from the other side.[20,25] Substantial optimization of purpose-built PRO membranes has proceeded since that time.[26–30] In 2009, the Norwegian state-owned energy company Statkraft opened a 10 kW pilot-scale plant following Loeb's original proposed plant configuration.[20,31,32]

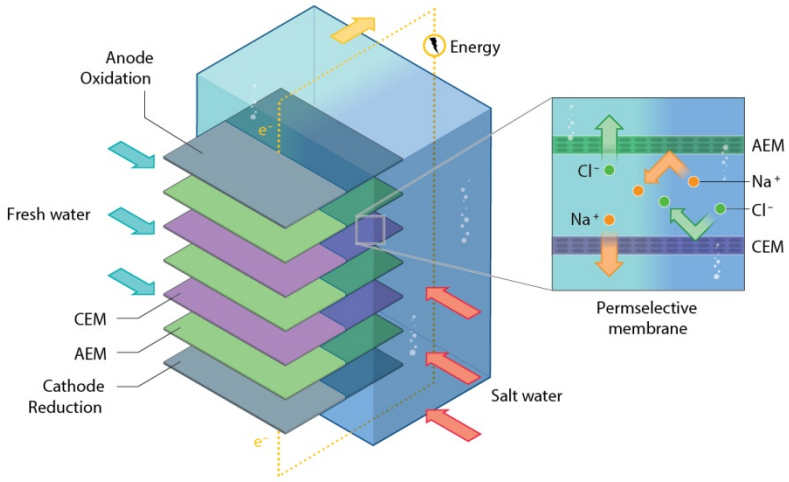


**Figure 1.2.** Scheme of reverse electrodialysis (RED); see main text for description. Reprinted by permission from Macmillan Publishers Ltd: *Nature*,[21] copyright 2012.

RED was first suggested by Pattle in 1954; the process is illustrated in Figure 1.2.[17] In an RED setup, alternating cation-selective and anion-selective membranes separate alternating streams of fresh water and seawater. The resulting electrolyte gradients across the charge-selective membranes produce electrical currents according to Equation 1.10, the Goldman-Hodgkin-Katz (GHK) current equation, which is derived from Equation 1.7. The charge-selective membranes are differentially permeable to cations and anions due to the presence of

fixed charges that allow mobile counter-ions to pass while restricting the movement of co-ions, a principle known as Donnan exclusion.[12]

$$I = \frac{VF^2\left[\left(\sum_i^{cations} P_i c_{i,cis} + \sum_j^{anions} P_j c_{j,trans}\right) - \left(\sum_i^{cations} P_i c_{i,trans} + \sum_j^{anions} P_j c_{j,cis}\right) e^{-VF/RT}\right]}{RT\left(1 - e^{-VF/RT}\right)} \quad (1.10)$$

Here, $I$ (A m$^{-2}$) represents the electrical current density, $V$ (V) is the voltage, $c_{s,cis}$ and $c_{s,trans}$ (mol m$^{-3}$) are the concentrations of species $s$ on either side of the membrane. The GHK equation is a functional relation that relates the current and the voltage across each membrane; the position of the system on the resulting "I-V" curve is determined by the connected resistive load. Considering the open-circuit condition illustrates the importance of the membranes' charge-selectivity; the GHK voltage equation (Equation 1.11, derived from Equation 1.10 and expressed here two different ways) relates the ratio of a membrane's permeabilities to sodium and chloride to the voltage that membrane produces when no current is flowing:

$$V_{OC} = \frac{RT}{F} \ln\left(\frac{P_{Na}\left[\mathrm{Na^+}\right]_{trans} + P_{Cl}\left[\mathrm{Cl^-}\right]_{cis}}{P_{Na}\left[\mathrm{Na^+}\right]_{cis} + P_{Cl}\left[\mathrm{Cl^-}\right]_{trans}}\right); \qquad \frac{P_{Na}}{P_{Cl}} = \frac{\left[\mathrm{Cl^-}\right]_{trans} e^{V_{OC}F/RT} - \left[\mathrm{Cl^-}\right]_{cis}}{\left[\mathrm{Na^+}\right]_{trans} - \left[\mathrm{Na^+}\right]_{cis} e^{V_{OC}F/RT}} \quad (1.11)$$

where $V_{OC}$ (V) is the open-circuit voltage. The current produced by an RED system scales with the area of the membranes; the voltage scales with the number of membrane pairs in a stack.

RED has the advantage that it produces electric current directly rather than requiring the transduction of mechanical work as in PRO. A significant number of lab-scale studies on RED have been published in recent years. A 50-kW pilot installation has been designed for implementation at the Afsluitdijk, a 32-km dam in the Netherlands between a freshwater lake and the ocean;[33] the plant opened in 2014, but no data on the success of the installation have been published.[34,35] A separate pilot installation in Sicily extracts power from the salinity gradient between sea water and brines produced by the Ettore-Infersa saltworks; using solutions with higher ionic strength lowers allows the system to operate with lower internal resistance.

This plant opened in 2015 and recently successfully scaled up its power output from tens to hundreds of watts by adding additional membrane modules.[36,37]

Following recent surges of interest (contemporary with the framing of the Kyoto Protocol in 1997 and the 2008 crude oil price spike)[20] and early optimism based on experiments using small membrane areas, the past few years have seen the publication of several feasibility studies which report a less-than-optimistic outlook for salinity-gradient power following an announcement that Statkraft was terminating its investment in PRO technology in 2013.[38] Despite considerable advances in optimizing the permeability, selectivity, and mechanical characteristics of membranes specific to PRO,[26] energy densities available via PRO processes are quite low,[39,40] and the tendency of the membranes to grow fouling biofilms[41] requires energy-expensive pretreatment processes that render facility-scale energy outputs minimal[42] or even negative[43] for streams of river and ocean water. The process-scale energy costs of RED are less well-studied, but the maximum theoretical power output is lower than in PRO[44] and has less room for performance improvement as existing membranes are nearly optimal, though they are currently orders of magnitude more expensive than they would need to be for the cost of RED power to be competitive.[13] Some studies suggest that both PRO and RED may be more useful power generation strategies when more concentrated streams are used, such as hypersaline reservoirs and the waste streams of industrial processes.[36,37,39,43,45–48]

### 1.3 Small-scale biological membrane-based energy transduction systems

If the prospects of widespread power generation from PRO and RED are disappointing, it is due in large part to difficulties with scaling up results obtained with small systems to industrial

proportions.[13,43] Municipal power grids are not the only scenario in which energy flows must be modulated, however, and a small system size is perfectly sufficient and even required for small-scale applications such as performance *in vivo*. Natural systems, for example, quite successfully allow organisms to survive and reproduce using mostly membrane-based energy transduction.

In the beginning of this chapter, I mentioned that photosynthesis and cellular respiration use proton gradients across membranes in order to generate ATP. These and other natural membrane-based transduction mechanisms such as neural signal propagation are effective because of membrane proteins, which are molecular machines that sit in the membrane and act as highly selective and monodisperse gatekeepers that can convert concentration or potential gradients into chemical energy. In the case of photosynthesis and respiration, the enzyme ATP synthase converts proton flux into a torque using a rotor mechanism similar to a windmill, providing the energy to induce a state change in the enzyme's catalytic regions that leads to ATP synthesis from ADP and inorganic phosphate.[49,50] The flux of four protons produces an ATP molecule, a process with nearly 100% efficiency.[51,52] Interestingly, certain extremophiles that thrive in hot, low-pH environments present ATP synthase on their cell membranes to generate ATP as protons rush into the near-neutral cell interior. The internal pH is actively maintained through various efflux mechanisms, and substantial passive proton influx bypassing the ATP synthase would likely collapse the proton gradient and kill the cell; the cell membranes of these extremophiles are therefore particularly impermeable to protons.[53,54] The membranes of these archaea are discussed in further detail in Chapter 3.

Not all functional membrane fluxes in biology generate chemical fuel. Plants maintain osmotic gradients via the transport of sugars and ions in order to distribute water throughout the body.[55] The resulting internal pressure, known as turgor, can reach tens of megapascals, a value

significantly higher than other living organisms. Shifts in turgor can produce swelling motions in plants on the time scale of hours or, when coupled with structural buckling instabilities, fast (nastic) motions on the time scale of seconds or below.[56,57] Famous examples of nastically moving plants are the Venus flytrap (*Dionaea muscipula*)[58] and the sensitive plant (*Mimosa pudica*).[59] These systems are analogous to PRO in that both schemes produce pressure-volume work using energy from osmotic gradients; Chapter 2 presents a model and mimic of the dynamic action of systems such as these.

Another biological membrane system where fluxes directly produce an effect (rather than generating ATP for later use) can be found in electric fish of various types, which have convergently evolved specialized organs that produce electric fields outside the body used for sensation and hunting.[60] Perhaps the most well-known of these is the electric eel, *Electrophorus electricus*, a knifefish native to South America that is capable of generating open-circuit voltages over 600 V and currents over 1 A.[61] *Electrophorus*'s electric organ is composed of long stacks of thin cells; in each cell, the membrane on the front side is permanently potassium-permeable, whereas the membrane on the back has sodium channels that open and potassium channels that close in response to a neural signal. Steep opposing gradients of sodium and potassium exist between the cells and the extracellular lumen. To produce a shock, the eels signal each cell in the organ at the same time, briefly turning the organ into an RED stack composed of a sequence of thousands of membranes that alternate in permselectivity for sodium and potassium.[61] Chapter 4 prevents a new small-scale reverse electrodialytic system that takes inspiration from the eel in a number of ways.

## 1.4 Small-scale artificial membrane-based energy transduction systems

To the best of my knowledge, no currently existing technology is able to directly transduce momentum from gradient equilibration across a membrane into usable energy in the manner of ATP synthase without using biological or bioengineered molecular machines. There has, however, been a significant amount of research in which molecular machines have been used to build up or speed the equilibration of gradients to exert osmotic or electrical influence on a system. Perhaps most significantly, the entire field of optogenetics is based around engineering light-sensitive ion channels (rhodopsins) that modulate the ion permeability of membranes, causing sufficient gradient equilibration on command to induce action potentials in living organisms.[62,63] This technique, which was originally proposed by Francis Crick,[64] can control neurons with high temporal resolution, enabling detailed study and engineering of neural networks.[65–69] The work of Vishnu-Baba Sundaresan is also relevant to this theme. In 2007-8, Sundaresan *et al*. created microactuators using planar lipid bilayers laden with proton-sucrose co-transporters. In the presence of ATP, the transporters actively pumped solutes across a membrane into a chamber in order to cause deflections in a flexible element of the chamber walls.[70,71] In 2010, Sundaresan *et al*. used ATP synthase (which can operate in reverse to pump protons and consume ATP) in a similar setup to actively create proton gradients across a membrane which could then be harnessed in the manner of RED in order to generate electrical power. Finally, building on work by Holden *et al*.,[72] in 2010-11 Xu *et al*. created "protocells" from droplet-interface lipid bilayers laden with ion channels that could generate power via RED.[73–75]

Non-lipid membranes have also been used quite successfully for energy transduction at small scales. Implantable and orally bioavailable mechanical actuators that respond to osmotic gradients have long been considered in the context of controlled drug delivery. In 1955, Rose

and Nelson developed a "continuous long-term injector" out of a rigid capsule whose hollow interior held a drug reservoir separated from a compartment of high osmotic pressure by an impermeable but flexible diaphragm. This osmotic driver was connected to an aqueous solution across a semipermeable membrane; over time, the osmotic compartment swelled, pushing the drug formulation out of a small aperture in the capsule (Figure 1.3, top right).[76] Since then, a number of improvements on this general principle have been implemented; these are shown in Figure 1.3.[77]

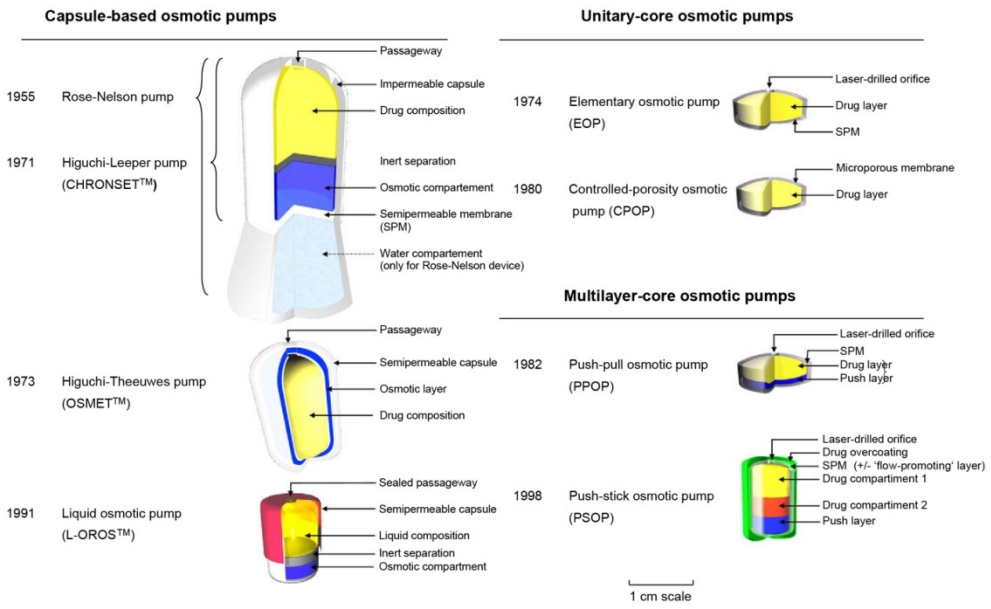


**Figure 1.3**. The evolution of osmotic pumps for controlled drug release. Yellow material represents drug formulation; blue material represents osmotic agent. Note that unitary-core osmotic pumps use the drug formulation itself as an osmotic driver. Reprinted from European Journal of Pharmaceutics and Biopharmaceutics, Vincent Malaterre *et al*, "Oral osmotically driven systems: 30 years of development and clinical use," p. 311-323, Copyright 2009, with permission from Elsevier.[77]

Today, over 30 commercially available drug formulations are marketed with osmotic release mechanisms.[77–80] Drug delivery with an osmotic pump offers a number of advantages over other controlled release schemes, and is ideal for drugs with a short half-life of circulation and long desired duration of exposure. This approach can provide extremely customizable

release profiles over time, from a constant (zero-order) delivery rate to delayed or pulsed delivery from one or multiple compartments. Osmotic release profiles are highly predictable and customizable, and are typically independent of variable parameters such as gastric pH and the presence of food that can interfere with other release strategies.[78]

Particularly since the turn of the century, a need has been recognized for small, green, efficient energy transducers for the distributed generation of electric power to microelectromechanical systems, implantable devices, and the other fruits of the miniaturization trend in modern technology.[81,82] In recent years, silicon-based membranes with micro-to-nano-scale channels bearing a surface charge have become the subject of some attention as energy sources. In 2003, Yang *et al*. published a manuscript reporting power generation from pressure gradients across microporous glass.[83] The negatively-charged surface of the pore interior attracts a boundary layer of electrolytes that becomes more diffuse and less tightly bound to the surface with greater distance according to the Gouy-Chapman-Stern model. The ion composition of the boundary layer in a small-scale channel is different than in bulk solution and nonhomogeneous with respect to radial position in the pore such that pressure-driven flow carries some ions in excess, causing the flow of so-called streaming current.[84] Development of streaming current-based power generation from hydrostatic and osmotic pressure gradients across nanoporous membranes has continued over the years;[85,86] recently, Feng *et al*. reported the use of "2-D" molybdenum disulfide membranes containing a nanopore that powered an integrated transistor in this way.[87] In 2010, Kim *et al*. first used charge-selective silica nanochannels to generate electric power in response to electrolyte gradients via RED (Figure 1.4); the mechanism of ion-selectivity again relates to the boundary layer within the nanopores.[88,89] Since then, RED has

been performed using conical nanopores,[90,91] nanoporous membranes made of alumina[92] and track-etched polycarbonate,[93] and plugs of charged nanoparticles.[94,95]

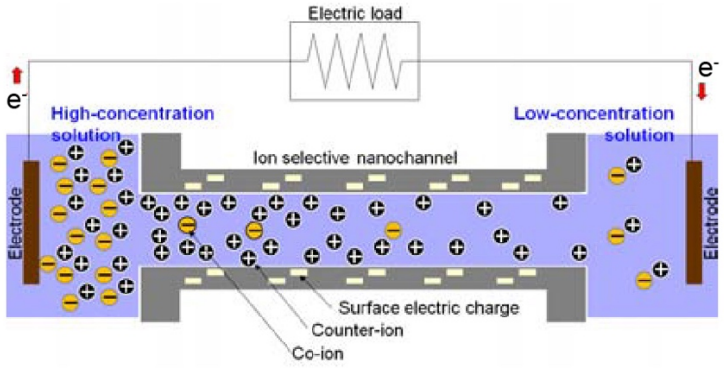


**Figure 1.4**. Illustration of RED in ion-selective nanopores. Note that streaming potential-based power generation operates using a similar mechanism, except that the driving force across the membrane is a pressure gradient. Reprinted from Journal of Mechanical Science and Technology, "Numerical study of power generation from reverse electrodialysis in ion-selective nanochannels," Vol. 25, 2011, p. 5-10, Dong-Won Kim, with permission of Springer.[89]

## 1.5 Summary of dissertation

In the subsequent chapters of this dissertation, I present three projects concerned with the equilibration of gradients across semipermeable membranes of various types. Each case takes inspiration from a natural membrane system.

In Chapter 2, a membrane-bound compartment converts gradients in osmotic pressure into hydrostatic pressure that can be used for the actuation of soft robotic devices, whose mechanism of action resembles that of the guard cells that open and close plant stomata. This process is similar to PRO, but is transient rather than steady-state. We therefore used a mathematical model to describe the dynamics of osmotically-driven pressure generation, exploring the importance of hydraulic permeability, surface-area-to-volume ratio, and restrictions on volume expansion on the rate of pressure change. We validated the model on a simple prototype pressure generation scheme composed of commercial dialysis membranes and a working solution of polyethylene glycol; the model also accurately describes the triggered

pressure changes that drive the fast motion of plants such as *Mimosa pudica*. The prototype pressure generator is intended as a device that can be "watered" like a plant to perform mechanical tasks; we tested its ability to actuate a soft robot and deliver fluid through an open tube.

Chapter 3 is a study of structure-function relationships in a special class of synthetic bolaamphiphilic lipids inspired by compounds found in the cell membrane of extremophiles in the kingdom *Archaea* that live in hot, acidic environments. These lipids, which self-assemble to form monolayer membranes rather than bilayers, contained systematic variations in the continuity and length of their transmembrane tether and the abundance of branching methyl groups on the lipid tails, enabling an examination of the importance of these structural motifs on the proton/hydroxide permeability of liposomes composed of these lipids. We measured the proton/hydroxide permeability of these membranes by imposing a pH gradient across the liposome membranes and measuring the kinetics of equilibration using a pH-sensitive fluorescent dye. We found a strong positive correlation between the experimentally-determined permeability and the frequency of spontaneous water penetration events into the membrane observed in molecular dynamics simulations, which is consistent with the hypothesized water-mediated mechanism of pH equilibration across lipid membranes.

Chapter 4 presents a power generation strategy that mimics the electric organs of the electric eel *Electrophorus electricus* mentioned earlier. We developed an entirely hydrogel-based system that similarly creates large series of ion gradients across selective membranes all at once. Neutral hydrogels with alternating high and low salinity are connected over alternating cation- and anion-selective hydrogels with fixed charges to generate additive potentials of arbitrary magnitude via RED; we were able to achieve voltages exceeding 100 V using thousands of gels

connected in series. Gel precursor solutions containing monomers and a radical photoinitiator are positioned as liquids using a printer or fluid handling device before being polymerized with UV light and brought into mechanical contact as a sequence of tetrameric repeating units. This artificial electric organ scheme is general enough that we were able to implement it in three distinct architectures; in particular, a design using a substrate that folded in a *Miura-ori* pattern proved able to stack thin gel films, producing a 40-fold improvement in power generation by altering the geometry of the system.

In Chapter 5, I describe the implications and logical future extensions of the projects described here.

**References**


1. Nelson, P. *Biological Physics: Energy, Information, Life*. (W. H. Freeman and Company, 2004).
2. Gennis, R. *Biomembranes: Molecular Structure and Function*. (Springer-Verlag, 1989).
3. Törnroth-Horsefield, S. & Neutze, R. Opening and closing the metabolite gate. *Proc. Natl. Acad. Sci. U. S. A.* **105,** 19565–19566 (2008).
4. Dismukes, G. C. *et al.* The origin of atmospheric oxygen on Earth: The innovation of oxygenic photosynthesis. *Proc. Natl. Acad. Sci.* **98,** 2170–2175 (2001).
5. Catling, D. C., Zahnle, K. J. & McKay, C. P. Biogenic Methane, Hydrogen Escape, and the Irreversible Oxidation of Early Earth. *Science* **293,** 839–843 (2001).
6. Lyons, T. W., Reinhard, C. T. & Planavsky, N. J. The rise of oxygen in Earth/'s early ocean and atmosphere. *Nature* **506,** 307–315 (2014).
7. Benyus, J. M. *Biomimicry: Innovation inspired by nature*. (Perennial New York, 2002).
8. Monroe, C. Intermediate Transport Phenomena. (2013).
9. Benedek, G. B. & Villars, F. M. H. *Physics with Illustrative Examples from Medicine and Biology: Statistical Physics*. (Springer-Verlag, 2000).
10. Kramer, E. M. & Myers, D. R. Five popular misconceptions about osmosis. *Am. J. Phys.* **80,** 694–699 (2012).

11. Hille, B. *Ion Channels of Excitable Membranes*. (Sinauer Associates, Inc., 2001).

12. Helfferich, F. *Ion exchange*. (McGraw-Hill, 1962).

13. Ramon, G. Z., Feinberg, B. J. & Hoek, E. M. V. Membrane-based production of salinity-gradient power. *Energy Environ. Sci.* **4,** 4423–4434 (2011).

14. Dai, A. & Trenberth, K. E. Estimates of Freshwater Discharge from Continents: Latitudinal and Seasonal Variations. *J. Hydrometeorol.* **3,** 660–687 (2002).

15. Długołęcki, P., Gambier, A., Nijmeijer, K. & Wessling, M. Practical Potential of Reverse Electrodialysis As Process for Sustainable Energy Generation. *Environ. Sci. Technol.* **43,** 6888–6894 (2009).

16. European Commission & Statistical Office of the European Communities. *The EU in the world 2014: a statistical portrait*. (2014).

17. Pattle, R. E. Production of Electric Power by mixing Fresh and Salt Water in the Hydroelectric Pile. *Nature* **174,** 660–660 (1954).

18. Pattle, R. E. Improvements relating to electric batteries. (1953).

19. Manecke, G. Source of current. (1955).

20. Achilli, A. & Childress, A. E. Pressure retarded osmosis: From the vision of Sidney Loeb to the first prototype installation — Review. *Desalination* **261,** 205–211 (2010).

21. Logan, B. E. & Elimelech, M. Membrane-based processes for sustainable power generation using water. *Nature* **488,** 313–319 (2012).

22. Norman, R. S. Water Salination: A Source of Energy. *Science* **186,** 350–352 (1974).

23. Loeb, S., Van Hessen, F. & Shahaf, D. Production of energy from concentrated brines by pressure-retarded osmosis: II. Experimental results and projected energy costs. *J. Membr. Sci.* **1,** 249–269 (1976).

24. Jia, Z., Wang, B., Song, S. & Fan, Y. Blue energy: Current technologies for sustainable power generation from water salinity gradient. *Renew. Sustain. Energy Rev.* **31,** 91–100 (2014).

25. Cath, T. Y., Childress, A. E. & Elimelech, M. Forward osmosis: Principles, applications, and recent developments. *J. Membr. Sci.* **281,** 70–87 (2006).

26. Han, G., Zhang, S., Li, X. & Chung, T.-S. Progress in pressure retarded osmosis (PRO) membranes for osmotic power generation. *Prog. Polym. Sci.* **51,** 1–27 (2015).

27. Achilli, A., Cath, T. Y. & Childress, A. E. Power generation with pressure retarded osmosis: An experimental and theoretical investigation. *J. Membr. Sci.* **343,** 42–52 (2009).

28. McCutcheon, J. R. & Elimelech, M. Influence of concentrative and dilutive internal concentration polarization on flux behavior in forward osmosis. *J. Membr. Sci.* **284,** 237–247 (2006).

29. Thorsen, T. & Holt, T. The potential for power production from salinity gradients by pressure retarded osmosis. *J. Membr. Sci.* **335,** 103–110 (2009).

30. Xu, Y., Peng, X., Tang, C. Y., Fu, Q. S. & Nie, S. Effect of draw solution concentration and operating conditions on forward osmosis and pressure retarded osmosis performance in a spiral wound module. *J. Membr. Sci.* **348,** 298–309 (2010).

31. Skilhagen, S. E., Dugstad, J. E. & Aaberg, R. J. Osmotic power — power production based on the osmotic pressure difference between waters with varying salt gradients. *Desalination* **220,** 476–482 (2008).

32. Crown Princess of Norway to open the world's first osmotic power plant | Statkraft. Available at: https://www.statkraft.com/media/press-releases/Press-releases-archive/2009/crown-princess-mette-marit-to-open-the-worlds-first-osmotic-power-plant/. (Accessed: 3rd October 2017)

33. Post, J. W. *et al.* Towards implementation of reverse electrodialysis for power generation from salinity gradients. *Desalination Water Treat.* **16,** 182–193 (2010).

34. dutchwatersector.com. Dutch King opens world's first RED power plant driven on fresh-salt water mixing. *Dutch Water Sector* Available at: https://www.dutchwatersector.com/news-events/news/12388-dutch-king-opens-world-s-first-red-power-plant-driven-on-fresh-salt-water-mixing.html. (Accessed: 3rd October 2017)

35. Moreno, J., de Hart, N., Saakes, M. & Nijmeijer, K. CO2 saturated water as two-phase flow for fouling control in reverse electrodialysis. *Water Res.* **125,** 23–31 (2017).

36. Tedesco, M. *et al.* Performance of the first reverse electrodialysis pilot plant for power production from saline waters and concentrated brines. *J. Membr. Sci.* **500,** 33–45 (2016).

37. Tedesco, M., Cipollina, A., Tamburini, A. & Micale, G. Towards 1kW power production in a reverse electrodialysis pilot plant with saline waters and concentrated brines. *J. Membr. Sci.* **522,** 226–236 (2017).

38. Statkraft halts osmotic power investments | Statkraft. Available at: https://www.statkraft.com/media/news/News-archive/2013/Statkraft-halts-osmotic-power-investments. (Accessed: 30th September 2017)

39. Lin, S., P. Straub, A. & Elimelech, M. Thermodynamic limits of extractable energy by pressure retarded osmosis. *Energy Environ. Sci.* **7,** 2706–2714 (2014).

40. Straub, A. P., Lin, S. & Elimelech, M. Module-Scale Analysis of Pressure Retarded Osmosis: Performance Limitations and Implications for Full-Scale Operation. *Environ. Sci. Technol.* **48,** 12435–12444 (2014).

41. Bar-Zeev, E., Perreault, F., Straub, A. P. & Elimelech, M. Impaired Performance of Pressure-Retarded Osmosis due to Irreversible Biofouling. *Environ. Sci. Technol.* **49,** 13050–13058 (2015).

42. O'Toole, G. *et al.* River-to-sea pressure retarded osmosis: Resource utilization in a full-scale facility. *Desalination* **389,** 39–51 (2016).

43. Straub, A. P., Deshmukh, A. & Elimelech, M. Pressure-retarded osmosis for power generation from salinity gradients: is it viable? *Energy Environ. Sci.* **9,** 31–48 (2016).

44. Yip, N. Y. & Elimelech, M. Comparison of Energy Efficiency and Power Density in Pressure Retarded Osmosis and Reverse Electrodialysis. *Environ. Sci. Technol.* **48,** 11002–11012 (2014).

45. Tedesco, M. *et al.* Reverse electrodialysis with saline waters and concentrated brines: A laboratory investigation towards technology scale-up. *J. Membr. Sci.* **492,** 9–20 (2015).

46. Tedesco, M., Cipollina, A., Tamburini, A., Bogle, I. D. L. & Micale, G. A simulation tool for analysis and design of reverse electrodialysis using concentrated brines. *Chem. Eng. Res. Des.* **93,** 441–456 (2015).

47. Tedesco, M., Cipollina, A., Tamburini, A., van Baak, W. & Micale, G. Modelling the Reverse ElectroDialysis process with seawater and concentrated brines. *Desalination Water Treat.* **49,** 404–424 (2012).

48. Farrell, E. *et al.* Reverse electrodialysis powered greenhouse concept for water- and energy-self-sufficient agriculture. *Appl. Energy* **187,** 390–409 (2017).

49. Romanovsky, Y. M. & Tikhonov, A. N. Molecular energy transducers of the living cell. Proton ATP synthase: a rotating molecular motor. *Phys.-Uspekhi* **53,** 893 (2010).

50. Yoshida, M., Muneyuki, E. & Hisabori, T. Atp Synthase -- a Marvellous Rotary Engine of the Cell. *Nat. Rev. Mol. Cell Biol. Lond.* **2,** 669–77 (2001).

51. Elston, T., Wang, H. & Oster, G. Energy transduction in ATP synthase. *Nature* **391,** 510 (1998).

52. Yasuda, R., Noji, H., Kinosita, K. & Yoshida, M. F1-ATPase is a highly efficient molecular motor that rotates with discrete 120 degree steps. *Cell* **93,** 1117–1124 (1998).

53. Baker-Austin, C. & Dopson, M. Life in acid: pH homeostasis in acidophiles. *Trends Microbiol.* **15,** 165–171 (2007).

54. Konings, W. N., Albers, S.-V., Koning, S. & Driessen, A. J. M. The cell membrane plays a crucial role in survival of bacteria and archaea in extreme environments. *Antonie Van Leeuwenhoek* **81,** 61–72 (2002).

55. Stroock, A. D., Pagay, V. V., Zwieniecki, M. A. & Holbrook, N. M. The Physicochemical Hydrodynamics of Vascular Plants. *Annu. Rev. Fluid Mech.* (2013).

56. Dumais, J. & Forterre, Y. "Vegetable Dynamicks": The Role of Water in Plant Movements. *Annu. Rev. Fluid Mech.* **44,** 453–478 (2012).

57. Guo, Q. *et al.* Fast nastic motion of plants and bioinspired structures. *J. R. Soc. Interface* **12,** 20150598 (2015).

58. Forterre, Y., Skotheim, Jan M., Dumais, J. & Mahadevan, L. How the Venus flytrap snaps. *Nature* **433,** 421–425 (2005).

59. Allen, R. D. Studies of the Seismonastic Reaction in the Main Pulvinus of Mimosa Pudica. (University of California, Los Angeles, 1967).

60. Bennett, M. V. L. Electric Organs. in *Fish Physiology* (ed. Randall, W. S. H. and D. J.) **5,** 347–491 (Academic Press, 1971).

61. Gotter, A. L., Kaetzel, M. A. & Dedman, J. R. Electrophorus electricus as a model system for the study of membrane excitability. *Comp. Biochem. Physiol. A. Mol. Integr. Physiol.* **119,** 225–241 (1998).

62. Pastrana, E. Optogenetics: controlling cell function with light. *Nat. Methods N. Y.* **8,** 24–25 (2011).

63. Method of the Year 2010. *Nat. Methods* **8,** 1–1 (2011).

64. Crick, F. The impact of molecular biology on neuroscience. *Philos. Trans. R. Soc. B* **354,** 2021–2025 (1999).

65. Deisseroth, K. Optogenetics. *Nat. Methods* **8,** 26–29 (2011).

66. Fenno, L., Yizhar, O. & Deisseroth, K. The Development and Application of Optogenetics. *Annu. Rev. Neurosci.* **34,** 389–412 (2011).

67. Yizhar, O., Fenno, L. E., Davidson, T. J., Mogri, M. & Deisseroth, K. Optogenetics in Neural Systems. *Neuron* **71,** 9–34 (2011).

68. Toettcher, J. E., Voigt, C. A., Weiner, O. D. & Lim, W. A. The promise of optogenetics in cell biology: interrogating molecular circuits in space and time. *Nat. Methods* **8,** 35–38 (2011).

69. Deisseroth, K. Optogenetics: 10 years of microbial opsins in neuroscience. *Nat. Neurosci.* **18,** 1213–1225 (2015).

70. Sundaresan, V. B., Homison, C., Weiland, L. M. & Leo, D. J. Biological transport processes for microhydraulic actuation. *Sens. Actuators B Chem.* **123,** 685–695 (2007).

71. Sundaresan, V. B. & Leo, D. J. Modeling and characterization of a chemomechanical actuator using protein transporter. *Sens. Actuators B Chem.* **131,** 384–393 (2008).

72. Holden, M. A., Needham, D. & Bayley, H. Functional Bionetworks from Nanoliter Water Droplets. *J. Am. Chem. Soc.* **129,** 8650–8655 (2007).

73. Xu, J. & Lavan, D. A. Designing artificial cells to harness the biological ion concentration gradient. *Nat. Nanotechnol.* **3,** 666–670 (2008).

74. Xu, J., Sigworth, F. J. & LaVan, D. A. Synthetic Protocells to Mimic and Test Cell Function. *Adv. Mater.* **22,** 120–127 (2010).

75. Xu, J., Vanderlick, T. K. & LaVan, D. A. Energy Conversion in Protocells with Natural Nanoconductors. *Int. J. Photoenergy* **2012,** e425735 (2011).

76. Rose, S. & Nelson, J. F. A Continuous Long-Term Injector. *Aust. J. Exp. Biol. Med. Sci.* **33,** 415–420 (1955).

77. Malaterre, V., Ogorka, J., Loggia, N. & Gurny, R. Oral osmotically driven systems: 30 years of development and clinical use. *Eur. J. Pharm. Biopharm.* **73,** 311–323 (2009).

78. Gupta, B. P., Thakur, N., Jain, N. P., Banweer, J. & Jain, S. Osmotically Controlled Drug Delivery System with Associated Drugs. *J. Pharm. Pharm. Sci.* **13,** 571–588 (2010).

79. Conley, R., Gupta, S. K. & Sathyan, G. Clinical spectrum of the osmotic-controlled release oral delivery system (OROS), an advanced oral delivery form. *Curr. Med. Res. Opin.* **22,** 1879–1892 (2006).

80. Santus, G. & Baker, R. W. Osmotic drug delivery: a review of the patent literature. *J. Controlled Release* **35,** 1–21 (1995).

81. Majumdar, A. & Tien, C.-L. Micro Power Devices. *Microscale Thermophys. Eng.* **2,** 67–69 (1998).

82. Pennathur, S., Eijkel, J. C. T. & van den Berg, A. Energy conversion in microsystems: is there a role for micro/nanofluidics? *Lab. Chip* **7,** 1234–1237 (2007).

83. Yang, J., Lu, F., Kostiuk, L. W. & Kwok, D. Y. Electrokinetic microchannel battery by means of electrokinetic and microfluidic phenomena. *J. Micromechanics Microengineering* **13,** 963 (2003).

84. Olthuis, W., Schippers, B., Eijkel, J. & van den Berg, A. Energy from streaming current and potential. *Sens. Actuators B Chem.* **111,** 385–389 (2005).

85. van der Heyden, F. H. J., Bonthuis, D. J., Stein, D., Meyer, C. & Dekker, C. Power Generation by Pressure-Driven Transport of Ions in Nanofluidic Channels. *Nano Lett.* **7,** 1022–1025 (2007).

86. Siria, A. *et al.* Giant osmotic energy conversion measured in a single transmembrane boron nitride nanotube. *Nature* **494,** 455–458 (2013).

87. Feng, J. *et al.* Single-layer MoS2 nanopores as nanopower generators. *Nature* **536,** 197–200 (2016).

88. Kim, D.-K., Duan, C., Chen, Y.-F. & Majumdar, A. Power generation from concentration gradient by reverse electrodialysis in ion-selective nanochannels. *Microfluid. Nanofluidics* **9,** 1215–1224 (2010).

89. Kim, D.-K. Numerical study of power generation by reverse electrodialysis in ion-selective nanochannels. *J. Mech. Sci. Technol.* **25,** 5–10 (2011).

90. Yeh, H.-C., Chang, C.-C. & Yang, R.-J. Reverse electrodialysis in conical-shaped nanopores: salinity gradient-driven power generation. *RSC Adv.* **4,** 2705–2714 (2014).

91. Hsu, J.-P., Lin, S.-C., Lin, C.-Y. & Tseng, S. Power generation by a pH-regulated conical nanopore through reverse electrodialysis. *J. Power Sources* **366,** 169–177 (2017).

92. Kim, J., Kim, S. J. & Kim, D.-K. Energy harvesting from salinity gradient by reverse electrodialysis with anodic alumina nanopores. *Energy* **51,** 413–421 (2013).

93. Kwon, K., Lee, S. J., Li, L., Han, C. & Kim, D. Energy harvesting system using reverse electrodialysis with nanoporous polycarbonate track-etch membranes. *Int. J. Energy Res.* **38,** 530–537 (2014).

94. Kang, B., Kim, M., Joo, H., Kim, H. J. & Kim, D.-K. Experimental study on energy harvesting from salinity gradient by reverse electrodialysis in Ag/AgCl deposited AAO nanochannel array. in *ASME 2013 International Mechanical Engineering Congress and Exposition* V010T11A066–V010T11A066 (American Society of Mechanical Engineers, 2013).

95. Choi, E., Kwon, K., Kim, D. & Park, J. Nanofluidic reverse electrodialysis platform using controlled assembly of nanoparticles for high power energy generation. in *2014 IEEE 27th International Conference on Micro Electro Mechanical Systems (MEMS)* 421–424 (2014). doi:10.1109/MEMSYS.2014.6765666

# CHAPTER 2

## Osmosis-Based Pressure Generation: Dynamics and Application

This section describes osmotically-driven pressure generation in a membrane-bound compartment while taking into account volume expansion, solute dilution, surface area to volume ratio, membrane hydraulic permeability, and changes in osmotic gradient, bulk modulus, and degree of membrane fouling. The emphasis lies on the dynamics of pressure generation; these dynamics have not previously been described in detail. Experimental results are compared to and supported by numerical simulations, which we have made accessible as an open source tool. This approach reveals unintuitive results about the quantitative dependence of the speed of pressure generation on the relevant and interdependent parameters that will be encountered in most osmotically-driven pressure generators. For instance, restricting the volume expansion of a compartment allows it to generate its first 5 kPa of pressure seven times faster than without a restraint. In addition, this dynamics study shows that plants are near-ideal osmotic pressure generators, as they are composed of many small compartments with large surface area to volume ratios and strong cell wall reinforcements. Finally, we demonstrate two applications of an osmosis-based pressure generator: actuation of a soft robot and continuous volume delivery over long periods of time. Both applications do not need an external power source but rather take advantage of the energy released upon watering the pressure generators.

This work was published in *PLOS ONE* in 2014.[1]

## 2.1 Introduction

The osmotic pressure gradient across a semipermeable membrane separating compartments of differing solute concentrations generates an important driving force in nature. This gradient, represented as $\Delta\Pi$, quantifies the entropically-driven tendency of the solvent in such systems to flow into the region of higher solute concentration; its value is equal to the pressure gradient that must be applied across the membrane to counteract this flow. As osmotic pressure varies with concentration, a concentration gradient established across a semipermeable membrane will create a pressure gradient if volume expansion on one side of the membrane is limited, as in an enclosed chamber. Plants in particular exploit this phenomenon, extensively employing osmotically-generated pressure gradients (known as turgor) for support and transport of water and solutes (Figure 2.1A).[2] In addition, certain specialized plants have evolved the ability to change the turgor inside different cells in response to external stimuli. These turgor shifts actuate for instance the opening and closing of guard cells in leaves or the swift nastic motions of the "sensitive plant" *Mimosa pudica* (Figure 2.1B) in response to touch via clusters of motor cells called pulvini.[3]

Two classes of osmotic processes are relevant here: forward osmosis (FO) and pressure retarded osmosis (PRO). FO processes are driven by an osmotic gradient $\Delta\Pi$ in the absence of a pressure gradient $\Delta P$ and are often used to concentrate a solute on one side of a membrane. FO's applications include desalination, purification, and concentration of solute.[4] PRO processes also make use of $\Delta\Pi$ as the dominant driving force; here, $\Delta\Pi$ is used to generate a $\Delta P$ in the opposite direction. The hydrostatic pressure generated by osmosis can be used to generate electric power using only fresh and salt water; this is a very clean alternative energy source.[5–7] A 10kW power

plant has recently been built in Tofte, Norway using PRO technology; a megawatt-scale plant is in the works.[8]

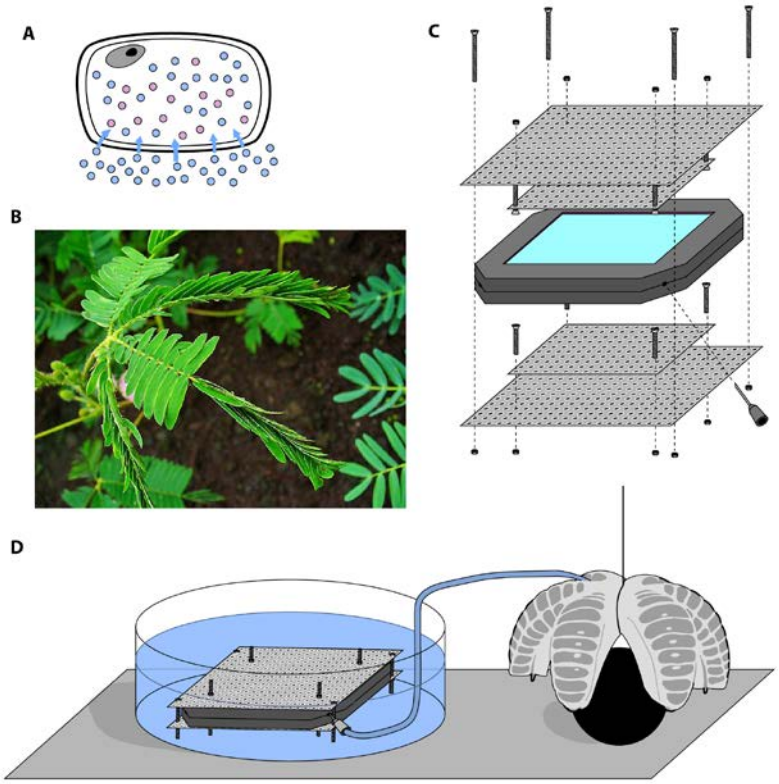


**Figure 2.1.** Biological and bioinspired pressure generation and actuation. A. Generation of turgor pressure due to an osmotic gradient across the semi-permeable cell membrane of a plant. Blue circles represent water molecules; red circles represent solute molecules. B. The sensitive plant, *Mimosa pudica*, in the middle of folding in response to touch. © H. Zell / Wikimedia Commons / CC-BY-SA-3.0 C. Prototype pressure generator consisting of a restrained dialysis cassette filled with working fluid used in this work. D. Schematic of the pressure generator being used to actuate a soft robotic gripper.

Herein we consider osmosis as a driving force for pressure and shape changes in small devices. Given that approximately 1.3 billion people worldwide lacked access to electricity as of 2012, the development and characterization of devices that can perform tasks without an external power source is critical.[9] Inspired by plants that use osmotic gradients to accomplish mechanical work, we propose that an osmosis-driven device with a high-osmolarity working fluid could similarly serve as a means of liberating usable potential energy from the chemical potential of

the fluid via pressure generation simply upon watering the device (Figure 2.1D). The mathematical model that we used and tested against experimental results revealed a dependency of the speed of pressure generation on volume expansion and membrane area to volume ratio not immediately apparent from the well-known relation between solvent flux and osmotic gradient:[10–12]

$$J_v = L_p(\sigma \Delta \Pi - \Delta P) \quad (1)$$

where $J_v$ (m $s^{-1}$) is the volumetric flux of water across the membrane, $L_p$ is the membrane's hydraulic permeability or filtration coefficient (m $Pa^{-1}$ $s^{-1}$), $\sigma$ is the dimensionless osmotic reflection coefficient representing the outward diffusion of the osmotic agent, $\Delta\Pi$ (Pa) is the difference in osmotic pressure between the working fluid compartment and the external solution (e.g. water), and $\Delta P$ (Pa) is the pressure difference across the membrane.

PRO and FO have largely been explored as industrial processes with parameters ($\Delta\Pi$, $\Delta P$) that are kept constant via circulation mechanisms. By contrast, the pressure generation that occurs in plant cells and our proposed devices is a transient process that builds up a continually increasing pressure gradient in opposition to the osmotically-driven influx of water into the compartment. To our surprise, a review of the literature revealed few previous studies of the *dynamics* of osmotically-driven pressure generation despite the potential usefulness of this information to actuate shape-changing materials and other devices. In 2007, Good *et al.* examined and modeled the displacement of liquid by an expanding (i.e. osmotically swelling) hydrogel compartment in a micropump over time.[13] The modeling, however, was based on the dynamics of polymer swelling rather than osmotic pressure generation. Swelling osmotic compartments have been developed[14–16] and modeled[11,12,17] for drug delivery applications, but the focus of the modeling has been on the displacement of a pharmaceutical agent rather than

internal pressure or volume. Microactuators powered by osmosis have been reported, such as in 2002 by Su *et al.*[18] and in 2007 by Sundaresan *et al*., who also published volume-focused modeling of the dynamics of actuation.[19,20]

## 2.2 Materials and Methods

*General Procedure for Pressure Generation Experiments*: To provide simple and accessible systems for studying the dynamics of osmotically-driven pressure generation, we constructed a restraint around commercially available 3 mL Slide-A-Lyzer dialysis cassettes (Thermo Scientific) with a molecular weight cutoff (MWCO) of 2,000 Da (Product #66203) or 3,500 Da (Product #66330) using perforated stainless steel plates (see Figure 2.1C,D). After bolting the dialysis cassette into the restraint, we hydrated it in water (Millipore Milli-Q purification system) for at least 2 min. We produced a working fluid of the desired concentration by diluting a 50% w/v (125 mM) aqueous poly(ethylene glycol) solution (PEG-4000, Hampton Research, HR2-529) with Milli-Q water, then added 3 mL to the restrained cassette. We attached a pressure transducer (ICU Medical, Transpac IV Disposable Pressure Transducer) to a length of rigid tubing with a needle at the end, filled this transducer setup with working fluid, and inserted the needle into the cassette through one of its ports, taking care to ensure that no air bubbles were allowed into the system. We monitored the pressure continuously via a custom-built LabView VI after connecting the transducer to a DAQ board (National Instruments BNC-2110) and a DC power supply (Hewlett Packard E3612A) at 6 V. Prior to submerging the cassette, we added working fluid via syringe until the internal pressure reached approximately 5 kPa. At this point, we lowered the restrained cassette into a large reservoir containing Milli-Q water to start pressure generation. Recording proceeded until failure of the cassette or of a fluidic connection.

For the experiments in Figure 2.2, we generally used 3 mL cassettes with a 3.5 kDa MWCO and initial PEG concentration of 70 mM. In Figure 2.2A, we varied the initial PEG concentration; in Figure 2.2B, we submerged one cassette without restraint; in Figure 2.2C, we varied the cassette size; in Figure 2.2D, we varied the MWCO of the dialysis membrane. Note that the initial membrane area to volume ratios for the 3 mL cassettes used were usually approximately 400 $m^{-1}$ while the ratio for 30 mL cassette was approximately 170 $m^{-1}$.

*Pumping Experiment for $L_{p,0}$ Determination:* For each MWCO, we restrained and hydrated a 3 mL cassette as described before, filled it slightly over capacity with pure water, and resubmerged it in a water bath. We attached a length of thin, rigid tubing of known diameter to the cassette. The other end of the tubing was connected to a constant-pressure pump (Nanion Suction Control Pro). Upon attachment to the cassette, the excess water from the cassette filled the tubing to a large extent before the meniscus stopped moving. The tubing was laid against a ruler and the pump was set to 30 kPa. The meniscus began moving toward the cassette; when it reached the ruler, its time and position were periodically recorded to obtain a volumetric flux.

*Volume Delivery Experiment*: After filling the dialysis cassette slightly over capacity with working fluid (PEG concentration 125 mM), we attached a length of rigid tubing of known volume filled with the same fluid to the cassette via a needle. We suspended the other end of the tubing above a graduated cylinder. We allowed fluid to exit the tube until the pressure inside the overfilled cassette fully equilibrated to atmospheric pressure. We emptied and replaced the graduated cylinder, then wrapped the cylinder opening and tubing loosely with parafilm to slow

evaporation. We submerged the cassette in Milli-Q water and periodically recorded the time and volume of fluid in the cylinder.

*Soft Robot Actuation Experiment*: We submerged a soft robotic gripper[21] obtained from the Whitesides group in water (Millipore Milli-Q purification system) and put it under vacuum until all air bubbles had escaped. We then fitted the gripper with rigid tubing and a needle filled with Milli-Q water. We prepared the osmotic pressure generator and pressure transducer as described in the pressure generation section, although for this experiment we used a 30 mL Slide-A-Lyzer dialysis cassette (Thermo Scientific) with a molecular weight cutoff of 3,500 Da (Product #66130), pre-filling it with 18 mL of solution. Just prior to initiating pressure generation, we attached the gripper to the cassette. We set up a camera to take images of the gripper every 20 seconds, then lowered the restrained cassette into the water and promptly initiated pressure recording and photography. Recording proceeded until failure of a fluidic connection to the gripper. The gripper depressurized upon failure or disconnection from the cassette.

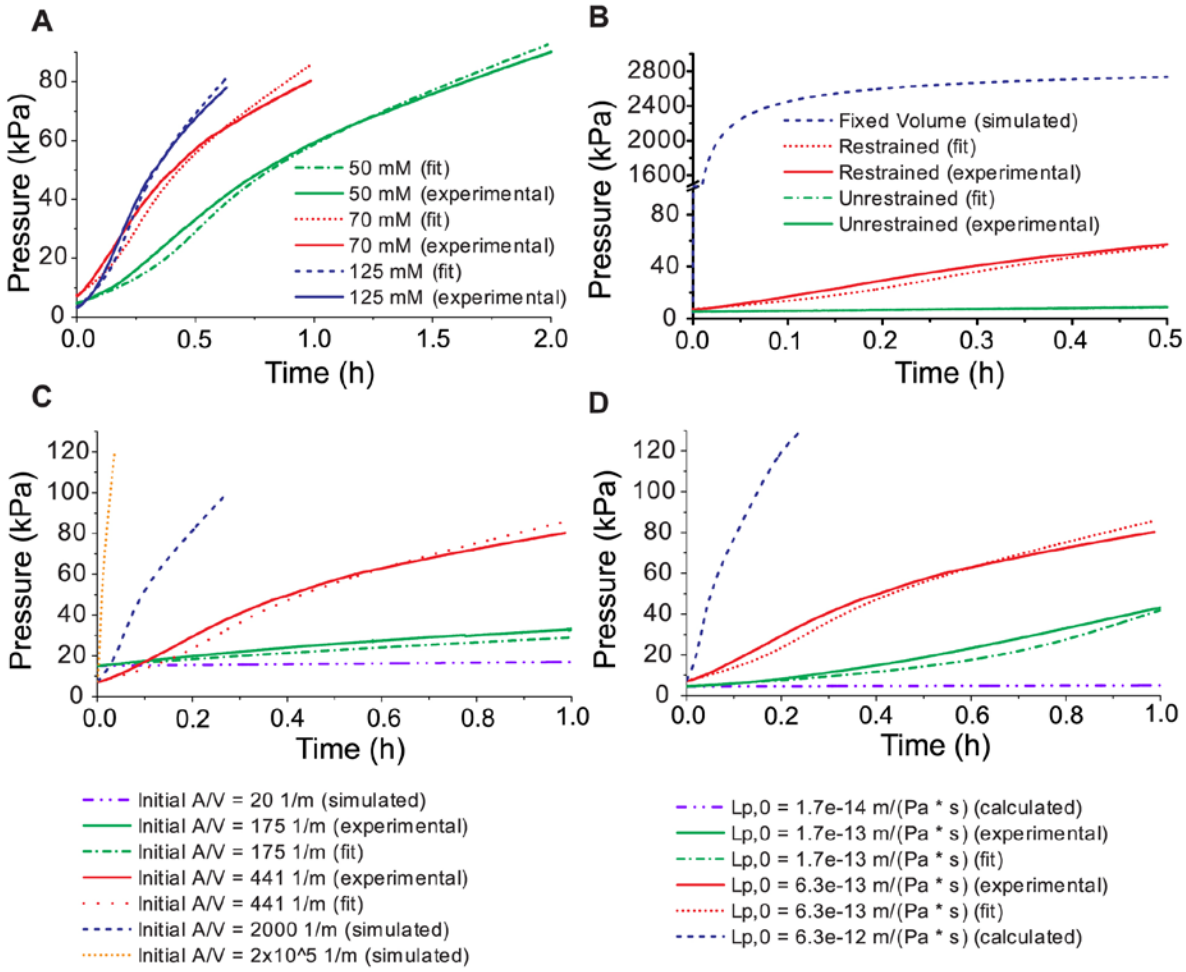


**Figure 2.2**: Dynamics of osmotically-driven pressure generation and comparison of the model based on Equation 2.4 with experimental data. **A**. Time-dependent pressure generation as a function of PEG-4000 concentration inside the dialysis cassette. **B**. Time-dependent pressure generation as a function of various mechanical constraints of the volume inside the dialysis cassette. **C**. Pressure generation dynamics as a function of various initial surface area to volume ratios. The dashed orange curve represents an initial *A/V* ratio taken from extensor cells of the plant *Phaseolus coccineus*.[28] **D**. Pressure generation dynamics as a function of various $L_{p,0}$ values.

## 2.3 Results and Discussion

We constructed prototypical pressure generators using commercially available dialysis cassettes with MWCOs of 2,000 and 3,500 Da and various concentrations of aqueous PEG-4000 as a working fluid. Dialysis cassettes are commercially available and easy to set up as pressure generators; PEG solution was chosen as a working fluid due to its compatibility with the

cassettes. We restrained the dialysis membranes of these cassettes with a porous steel screen to delay membrane failure and restrict volume expansion (Figure 2.1C). Upon submersion, the device generated pressure as shown in Table 2.1 and Figure 2.2.

**Table 2.1.** Dynamics of pressure generation as a function of various parameters. Each row represents one experiment.

| Membrane Cutoff (kDa) | Initial volume ($10^{-6}$ m$^3$) | Initial *A/V* ratio (m$^{-1}$)[a] | Initial [PEG] (mM) | Initial osmotic pressure ($10^6$ Pa) | Time to gain 10 kPa (min) | Time to gain 50 kPa (min) | Calculated *A* (cm$^2$) |
|---|---|---|---|---|---|---|---|
| 2.0 | 5.03 | 435.4 | 30 | 0.38 | 28 | 206 | 21.9 |
| 2.0 | 4.93 | 444.2 | 50 | 1.31 | 26 | 132 | 23.0 |
| 2.0 | 4.73 | 463.0 | 70 | 3.09 | 23 | 75 | 32.3 |
| 2.0 | 4.75 | 461.1 | 70 | 3.09 | 14 | 58 | 41.3 |
| 2.0 | 4.52 | 484.5 | 125 | 14.73 | 26 | 53 | 41.4 |
| 2.0 | 4.66 | 470.0 | 125 | 14.73 | 10 | 38 | 51.9 |
| 2.0 [unrestrained] | 6.47 | 338.5 | 70 | 3.09 | 134 | [n/a] [b] | 18.9 |
| 3.5 | 5.98 | 366.2 | 30 | 0.38 | 15 | 104 | 21.2 |
| 3.5 | 5.92 | 369.9 | 50 | 1.31 | 14 | 54 | 20.4 |
| 3.5 | 5.99 | 365.6 | 70 | 3.09 | 6 | 30 | 26.4 |
| 3.5 | 6.28 | 348.7 | 70 | 3.09 | 5 | [n/a] [b] | 21.4 |
| 3.5 | 5.88 | 372.4 | 125 | 14.73 | 6 | 22 | 22.3 |
| 3.5 | 5.86 | 369.9 | 125 | 14.73 | 6 | [n/a] [b] | 23.9 |
| 3.5 [30mL] | 35.2 | 170.5 | 70 | 3.09 | 27 | 311 | 61.5 |
| 3.5 [unrestrained] | 6.97 | 314.2 | 70 | 3.09 | [n/a] [b] | [n/a] [b] | 36.2 |
| Pulvinus extensor cell | $3.23\times10^{-7}$ [c] | $6.27\times10^{4}$ [c] | [c] | 1.98[d] | 5[d] | 8[d] | $2.03\times10^{-4}$ [c] |

[a] Initial membrane area was assumed to be 21.9 cm$^2$ for 3mL cassettes, 60.0 cm$^2$ for 30mL.
[b] [n/a] indicates failure before pressure point.
[c] Extensor cell surface area and volume taken from *Phaseolus coccineus* [28]; $L_p$ ($3.63\times10^{-14}$ m Pa$^{-1}$ s$^{-1}$) taken from *Samanea Saman* in the evening.[29]
[d] Osmolality of an active pulvinar cell ≈ 1000 mOsm/kg.[30] This calculation was made using the van't Hoff equation rather than Equation S2.1 in Appendix S2.1 as the osmotic agents in a plant cell are primarily sugars and ions rather than polymers. The fouling factor was assumed to be zero for the same reason.

To characterize the dynamics of the system, we modeled the pressure generation by using two differential equations for the change in mass within the cassette over time. First,

$$\frac{dm}{dt} = A*\rho_{solvent} * J_v = A*\rho_{solvent} * L_p * \left(\Delta\Pi - P_{in}\right) \quad (2)$$

where $A$ ($m^2$) is the total membrane area and $\rho_{solvent}$ (kg $m^{-3}$) is the density of water. This equation assumes that the reflection coefficient $\sigma$ equals one, representing a leak-free membrane over the course of the entire experiment. For ideal solutions, $\Pi$ is known to vary linearly with concentration according to the van't Hoff relation. However, polymer solutions often deviate from this linearity; the slope of $\Pi$ versus concentration increases as a function of concentration.[22] Using a freezing-point depression osmometer, we established that the osmotic pressure of aqueous PEG-4000 solutions increases as a function of PEG concentration following a third-order polynomial function ($N$ = 14, $R^2$ > 0.99, see Appendix S2.1 and Figure S2.1). PEG's favorably non-linear osmotic pressure curve and large size make it an attractive osmotic working fluid. A 0.125 M solution of PEG-4000 generates an osmotic driving force comparable to that of a solution of NaCl at its solubility limit of 5.28M[23] while being easily retained by a dialysis cassette with a MWCO in the kDa range.

Additionally, we determined from a series of volume delivery experiments that the effective $L_p$ decreases drastically with increasing PEG concentration (see Appendix S2.2 and Figure S2.2). We conjecture that PEG molecules bind to the pores in the dialysis membrane, impeding the flux of water. Such membrane fouling is one of two phenomena observed in industrial osmotic processes that could cause a similar reduction in $L_p$ – the other, concentration polarization, is considered negligible across dialysis membranes such as ours (see Appendix S2.3).[24,25] We therefore split $L_p$ into two parameters according to $L_p = L_{p,0}(1 - f)$, where $L_{p,0}$ is the $L_p$ value in the absence of PEG and $f$ is a "fouling factor" that represents the percentage of blocked pores. We found that $f$ varies as a function of PEG concentration and is described well by the Hill equation for cooperative binding ($R^2$ > 0.98, see Appendix S2.3).

Second, from the definition of bulk modulus $K$ (Pa), while $K >> P_{in}$ we obtain

$$\frac{\partial m}{\partial t} = \frac{\partial}{\partial t}\left(\rho_{in} V_{in}\right) = \frac{\partial}{\partial t}\left(\frac{\rho_{atm} V_{in}}{1 - P_{in}/K}\right) \tag{3}$$

where "in" denotes a characteristic of the cassette's interior, $\rho_{atm}$ (kg m$^{-3}$) is the density of the working fluid at atmospheric pressure. We determined the bulk modulus of aqueous PEG solutions with different concentrations and at various pressures by measuring the velocity of a pressure wave in solution and found that $K$ follows a second-order polynomial function with respect to PEG concentration and varies linearly with pressure ($N$ = 58, $R^2$ = 0.93, see Appendix S4 and Figures S3 and S4 in Bruhn, Schroeder, *et al*. 2014[1]). Finally, we measured the pressure-dependent volume expansion $V_{in}(P_{in})$ for each type of cassette and restraint using a procedure described in Appendix S2.4. Considering volume expansion as a function of pressure ensures that time-dependent changes in the PEG concentration (i.e. solute dilution) as well as the resulting implications for $\Delta\Pi$, $K$, $f$, and $P_{in}$ are accounted for.

Combining Equation 2.2 and Equation 2.3 yields a governing equation:

$$\frac{\partial}{\partial t}\left(\frac{\rho_{atm} V_{in}}{1 - P_{in}/K}\right) = A * \rho_{solvent} * L_{p,0}\left(1 - f\right)\left(\Delta\Pi T - P_{in}\right) \tag{2.4}$$

This differential equation has no simple analytical solution for $P_{in}$ versus $t$ even when all parameters are fixed, so we solved Equation 2.4 numerically using a variable step Runge-Kutta method in MATLAB (the ode45 function). In order to solve for $P_{in}(t)$, we needed to find values or functional relations for each of the other parameters in Equation 2.4. We used the $V_{in}(P_{in})$ relationship and the initial PEG concentration to obtain an expression for the concentration of the working fluid, which is simply the ratio of the number of moles of PEG inside the cassette (assumed to be constant) over the volume of the cassette, $V_{in}(P_{in})$. Since the $K$, $f$, and $\Delta\Pi$ functions determined previously are dependent on concentration, it was then possible to express

each as a function of $P_{in}$. We used the density of water[26] for $\rho_{solvent}$ and a density calculated as a function of initial PEG concentration at atmospheric pressure for $\rho_{atm}$.[27] We assumed that the membrane hydraulic permeability $L_{p,0}$, which we obtained in a manner described in Appendix S2.3, would stay constant over the course of the experiment. The $L_{p,0}$ value obtained for dialysis cassettes with a MWCO of 3.5 kDa was 6.26 x $10^{-13}$ m $Pa^{-1}$ $s^{-1}$, over three times the value obtained for cassettes with a MWCO of 2.0 kDa, which had an $L_{p,0}$ of 1.70 x $10^{-13}$ m $Pa^{-1}$ $s^{-1}$. This analysis confirms the expectation that membranes with a large MWCO are more permeable than membranes with a smaller MWCO.

After defining these values and relations, the parameter most difficult to obtain a definite value for is $A$, as it is unclear from observation whether the available membrane area increases with bulging upon pressurization or decreases due to blocking by the restraint. To determine $A$ for each experiment, we ran a fitting script with a set of experimental data in which the area was allowed to vary. The script returns the $A$ value that minimizes the residual sum of squares between the experimental data of $P_{in}$ as a function of time and the pressure generation curve predicted by Equation 2.4. In this way, we are able to determine $A$ based on $P_{in}(t)$ data or predict a $P_{in}(t)$ curve for a given $A$ in compartments of known $L_{p,0}$, fouling behavior, and $V_{in}(P_{in})$ relationship. For 3 mL cassettes, the mean area of the 2.0 kDa MWCO membranes was determined to be 35.3 ± 11.7 $cm^2$ while the mean area of the 3.5 kDa MWCO membranes is 22.1 ± 2.5 $cm^2$. For reference, the estimated bulging membrane area is approximately 21.9 $cm^2$, so the calculated $A$ values are in reasonably good agreement, especially for the 3.5 kDa MWCO cassettes. These values indicate that the steel mesh does not reduce the membrane area available for flux.

The variation between the $A$ values shown in Table 2.1 that were obtained by fitting data from experiments using membranes of the same type is likely a result of simplifications in our model's assumptions. Since $A$ is the only fitting parameter, any discrepancy between our modeled $P_{in}(t)$ curve and the experimental data will be reflected in the best-fit value of $A$. Hence, $A$ may vary between experiments as it compensates for a number of different factors. Commercial dialysis cassettes are not designed to be pressurized; we had to assemble and disassemble an external reinforcement for experiments. As a result, $V_{in}(P_{in})$ may vary between cassettes of the same type, but the model does not account for such variation. Further, the possible expansion of dialysis membranes upon pressurization as a function of time could increase the effective MWCO of the membrane. Our model assumes that $L_{p,0}$ and $A$ remain constant over the course of the experiment and that the reflection coefficient $\sigma$ remains 1. The polynomial equation for $\Delta\Pi$ as a function of PEG concentration may also introduce some error at concentrations above 80 mM, which are above the range of our osmometer. At low concentrations, the $\Delta\Pi$ driving force is less dominant than in experiments using a concentrated PEG solution, so artifacts caused by small variations in the experimental setup such as air bubbles or slight inaccuracies in initial volume and concentration would have a more noticeable effect. Considering that one or several of these factors may influence the determination of $A$, the observed variations of $A$ seem to be within a reasonable range and are generally accurate within a factor of two.

Solving Equation 2.4 for $P_{in}(t)$ yielded excellent fits of pressure generation curves to the experimental data (Figure 2.2A). The agreement between the data and the fits validates the approach and shows that solving Equation 2.4 iteratively makes it possible to predict the pressure generation dynamics for a range of osmotic driving forces and relevant parameters. For example,

we were able to predict the dynamics of osmotic pressure generation in chambers with the dimensions and $L_p$ values of plant cells and compare them to our systems; see Figure 2.2C and Figure 2.2D. This comparison revealed, for instance, the importance of restraining the cassettes as shown in Figure 2.2B: restricting $V_{in}(P_{in})$ accelerates pressure generation dramatically. The hypothetical constant volume case would be capable of generating megapascals of pressure within seconds. For practical reasons, a constant $V_{in}(P_{in})$ relationship is more readily attainable on a small scale. In addition, scaling down the compartment for the working fluid increases the initial membrane-area-to-volume ratio ($A/V$) of the system, as $A/V$ for any object is inversely proportional to characteristic length. A high $A/V$ value is beneficial for rapid pressure generation as displayed in Figure 2.2C: the projected pressure generation curve using the $A/V$ value of plant motor cells (extensors in *Phaseolus coccineus*)[28] increases so quickly that the curve appears completely vertical when plotted on the timescale shown in the figure.

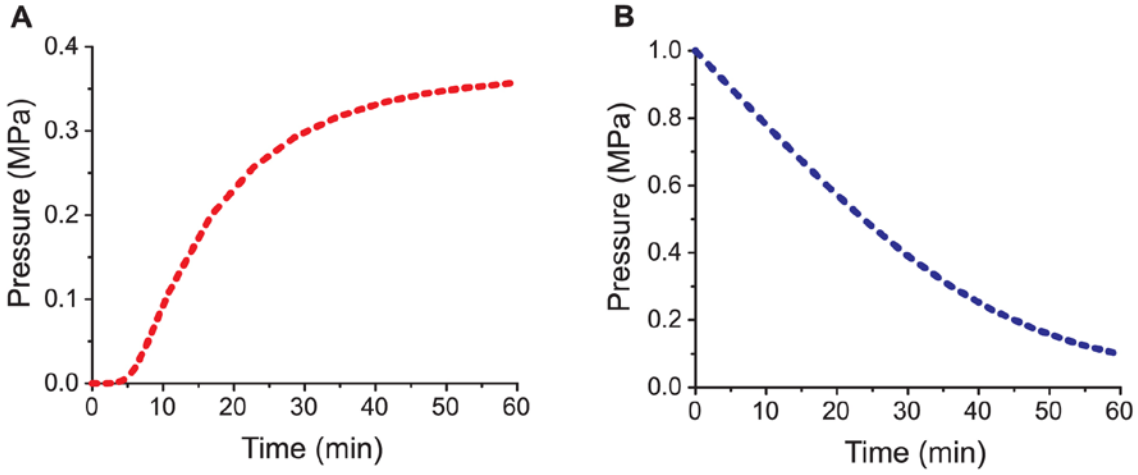


**Figure 2.3**: Dynamics of pressure buildup and release in plant extensor cells as calculated with Equation 2.4 and parameters based on literature values. The $L_{p,0}$ value used in the calculations was 3.6 x $10^{-14}$ m $Pa^{-1}$ $s^{-1}$,[29] the cell volume was 3.23 x $10^{-13}$ $m^3$, the surface area was 2.02 x $10^{-8}$ (both estimated from [28]), and $V_{in}(P_{in})$ was $V_{in}$ = (3.23 x $10^{-13}$)exp[1.06x$10^{-6}$ $P_{in}$ + 0.047 ln($P_{in}$)] (developed from literature bulk elastic modulus values[28] and the definition of bulk elastic modulus[31]). In these calculations $\Delta\Pi$ followed the van't Hoff relation and $f$ was assumed to be zero. **A**. Pressure buildup upon sudden introduction of an osmotic gradient with an initial $\Delta\Pi$ of 1 MPa[23] **B**. Pressure release upon sudden disappearance of an osmotic gradient. Initial $P_{in}$ was 1 MPa.[23, 24] The difference between the maximum pressure from the pressurization curve and the starting pressure from the depressurization curve can be accounted for by the fact that our model assumes no significant biochemical regulation of osmotic pressure during this fast pressurization. As a consequence, the influx of water leads to a decrease in $\Delta\Pi$.

Using the dimensions,[28] $L_p$ value,[29] the final $\Delta\Pi$ value[30] from plant pulvini, and a $f$ value of zero, along with a $V_{in}(P_{in})$ curve developed from values of bulk elastic modulus in *Phaseolus coccineus* extensor cells [28] and the definition of bulk elastic modulus[31], we used Equation 2.4 to predict the dynamics of pressure generation in these motor cells (Figure 2.3A). As summarized in Table 1, this approach suggests that these plant motor cells are able to generate 50 kPa within 8 minutes. This rate is threefold faster than the fastest pressure generators tested here. We point out, however, that the mechanism of motor cell function in mimosa pudica and other plants that undergo fast motions is slightly different than the devices presented here. In fast-moving plants, turgid cells are prefilled with osmotic agents (often potassium and chloride ions) via protein-mediated active transport, an energy-intensive process that takes place on the time scale of minutes to hours.[32] Upon receiving a stimulus, ion channels open in these cells, causing the osmotic agents to equilibrate with the extracellular fluid.[33] This flux eliminates the osmotic driving force necessary to maintain turgor, so the cells depressurize. A demonstration of this effect assuming instantaneous working fluid equilibration is shown in Figure 2.3B. The same parameters were used as in the calculated $P_{in}(t)$ curve in Figure 2.3A, but the initial pressure $P_{in}(0)$ was set to 1 MPa[34,35] and upon stimulation $\Delta\Pi$ was set to zero. This approach predicts that cells with these characteristics are able to lose 10% of their osmotic pressure (~100 kPa) in 4.5 minutes. By comparison, *mimosa pudica* extensor cells lose 10% of their pressure within 5 minutes.[36] In principle, strategies for generating an osmotic gradient on-demand such as electro-osmosis and ion transport via membrane proteins could be explored in membrane-bound synthetic actuators and described by our model. The implementation of these methods is beyond the scope of our research.

After modeling the dynamics of pressure generation, we created a bio-inspired actuator system by attaching a 30 mL cassette filled with saturated (125 mM PEG-4000) working fluid to a soft robotic gripper (Figure 2.1D).[21] Each arm of the gripper is filled with channels that run perpendicular to its length (Figure 2.4A). The inside walls of the channels are thicker than the outside walls so that when positive pressure is applied, the outer walls deform more than the walls on the interior. When such channels are lined up in a row, the system curves upon pressurization, causing the arms of the gripper to bend inward.[21,37–39] Guard cells open and close plant stomata using a similar mechanism. On each pair of guard cells, the cell wall that faces the pore is thicker than the wall on the outside of the stoma. When coupled with microfibrils that restrict the guard cell circumference to remain relatively constant, this wall architecture causes the cells to curve into an "O" shape when pressure is delivered via osmosis, thus opening the pore in response to external stimuli (Figure 2.4B).[40]

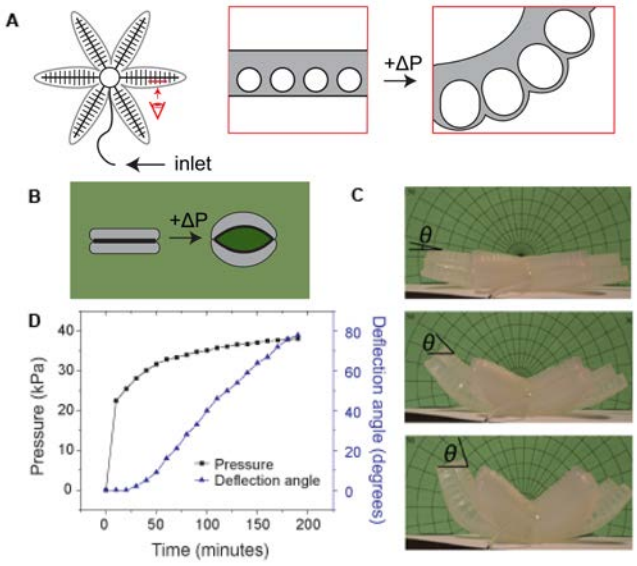


**Figure 2.4.** Bioinspired application of an osmotic pressure generator for actuation of a soft robot. **A.** Design concept of a previously described elastomeric soft robot whose arms curve and can grip objects in response to pressurization of parallel channels with boundaries of differing thickness. Adapted from Ilievski *et al*.[21] **B.** Guard cells in their open and closed states. Thick interior walls make guard cells curl when osmotically pressurized, opening stomata.[32] **C**. Actuation of the soft robotic gripper used in this work in response to watering an attached osmotic pressure generator. The extent of deflection is shown after 1, 2, and 3 hours. **D**. System pressure and deflection angle (as defined in C) of the gripper as a function of time.

We recorded the pressure and deflection angle of the soft robot over time (Figure 2.4C,D, Video S2.1). Full deflection took approximately three hours, after which the fluidic connection to the gripper sprang a leak. The slow timescale of this actuation was noteworthy, especially considering the quick action of the mimosa plant. Our model confirmed that using larger compartments with lower *A/V* ratios such the prototypes and robot used here slows down pressure generation more dramatically than intuition may suggest (Figure 2.2C).

Using these relatively large commercially available dialysis cassettes does, however, also have its advantages. First, this system is sufficiently simple and inexpensive that any laboratory could set up a pressure generator with ease – large-scale industrial production of the cassettes should also result in relatively constant values of parameters such as initial *A/V* ratio, $L_{p,0}$ value, $V_{in}(P_{in})$, etc. Second, near-instantaneous pressure generation is only useful in some scenarios and may not be the most important parameter for a given application. Slow but continuous volume delivery is, for instance, another interesting application of these devices. A 30 mL cassette with a lower initial *A/V* ratio than the 3 mL cassettes typically used in this work took significantly longer to generate pressure as expected (Table 2.1), but in our volume delivery experiment these larger cassettes were able to pump 86 mL of fluid over approximately two days compared to the smaller cassette which pumped 13 mL in the same time (Figure 2.5). This kind of extended self-powered pump activity might be particularly attractive for microfluidic applications[41–46], which often require flow rates of only nanoliters to microliters per hour. For instance, almost a week after starting an experiment, a generator with 3 mL of initial working fluid was still delivering a flow of greater than 1 µL/min. Additionally, after an initial leveling-off period of approximately 30 h, the flow rate stayed remarkably constant for 3 days, with an average decrease of only 0.4% per hour (Figure 2.5A).

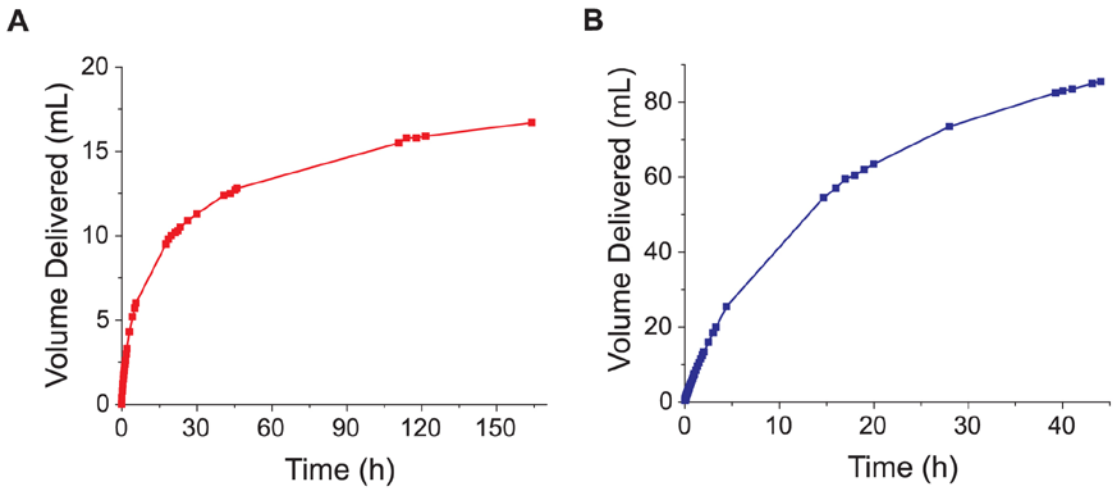


**Figure 2.5**: Time-dependent volume delivery using an osmotically-driven pressure generator as a pump. **A**. Cumulative volume delivered by a 3 mL dialysis cassette. **B**. Cumulative volume delivered by a 30 mL cassette. Both cassettes were restrained and filled with a 125 mM PEG-4000 solution and had a MWCO of 3.5 kDa.

Restricting volume expansion is another important aspect that should be considered depending on the application of osmotically-driven pressure generators. Allowing the volume of a container to expand causes its internal pressure to rise much more slowly compared to the restricted case (Figure 2.2B), but a system that swells to accommodate a large volume of pressurized fluid stores more energy than a system with a smaller volume at the same pressure. Consider the pressure-volume work done on the cassette over the course of pressure generation as representative of the energy stored. When we allowed the cassette to expand without a restraint, the first 5 kPa generated from osmosis took five to ten times longer to generate than it did with the restraint. Once this pressure was reached, however, the volume of pressurized fluid in the vessel was much bigger. In this way an unrestrained cassette at 5 kPa stores approximately an order of magnitude more energy than a restrained one at the same pressure. Volume expansion additionally may be desirable if a constant pressure is needed in an osmotic system. During the soft robot experiment, the period from 50 minutes through the end of the experiment saw a relatively constant pressure accompanied by the most rapid deflection of the gripper

(Figure 2.4D). Based on these phenomena, we demonstrate that a volume-expanding element can be used analogously to a capacitor in an electrical system: it can both store energy and stabilize the difference in potential (pressure) between two points. Flexible membranes with fluidic capacitance have been used in microfluidic devices to these ends.[47–54]

## 2.4 Conclusions

The diversity of tasks for which plants use osmosis represents a rich field of potential technological advancements that harness the same driving force to actuate materials and devices.[55] We have shown that an osomotically-driven pressure generator can be constructed from materials that are low-cost and readily available. In addition, the model based on Equation 2.4 can be used to predict the dynamics of pressure generation for anyone seeking to create devices with the capability to generate pressure or deliver volume for a range of applications. The MATLAB code used for the calculated pressure generation curves in this work is available on SourceForge (https://sourceforge.net/projects/osmoticpressurization_dynamics/files/). If an aqueous PEG-4000 solution is used as the working fluid, there are three parameters needed to calculate $P_{in}(t)$: the membrane hydraulic permeability, which is attainable from the pumping experiment described in Appendix S2.3, the dependence of $f$ on PEG concentration, which is attainable from the volume delivery experiments described in Appendix S2.2, and the dependence of $V_{in}(P_{in})$, which is attainable by measuring the pressure of the device's reservoir while adding known volumes as described in Appendix S2.5. If the type of cassettes described here are used, these values and relations are described in this work and do not need to be measured once again. Other solutes can be used as well if the relationship between $\Delta\Pi$ and concentration is known. If precisely determined, $A$ can also be input; otherwise the code can load

an experimental data set of pressure versus time and find the best-fitting *A* value. We hope other researchers will find this model and the effects shown in Figure 2.2 useful for defining the dimensions and parameters of pressure generators of their own construction.

One compelling property of the osmotic pressure generators described in this work is that they can generate pressure and fluid flow without access to external power. Simply "watering" the device initiates the process in a manner similar to watering a plant. The novelty of the work presented here – in addition to providing insight into the fundamental and unintuitive time dependence of establishing or releasing turgor pressure in plants (Figures 2.2 and 2.3) – lies in a detailed characterization of the dynamics of these engineered osmotic pressure generators such that they may be used in microfluidics and microactuation with predictable outcomes.

## 2.5 **Contributions of Others**

Brandon Bruhn, Suyi Li, and Yazan Billeh performed all bulk elastic modulus measurements; a description of this procedure can be found in Appendix S4 and Figures S3 and S4 in Bruhn, Schroeder, *et al*. 2014.[1] Brandon Bruhn assisted me in pressure generation experiments; he and I co-wrote the MATLAB pressure generation code. Filip Ilievski and the Whitesides Group at Harvard University provided the soft robotic gripper used here. This project was conceived by Michael Mayer and Kon-Well Wang.

## Chapter 2 Appendix

### S2.1. Osmotic Pressure Measurements:

Measurements of the non-ideal osmotic character of aqueous PEG solutions were obtained from freezing point depression using an Advanced Instruments Model 3320 Micro-Osmometer. Curves were obtained from a cubic fit bound to the origin.

The osmometer is limited to taking measurements of species it is able to freeze, which restricts our measurements to concentrations of 80 mM and below. The function obtained from a cubic fit is:

$$\Pi = \left(5.86\ \text{Pa mol}^3\ \text{m}^{-9}\right)*[PEG]^3 + \left(196.94\ \text{Pa mol}^2\ \text{m}^{-6}\right)*[PEG]^2 + \left(1634.14\ \text{Pa mol m}^{-3}\right)*[PEG] \quad \text{(S2.1)}$$

($N = 15$, $R^2 > 0.99$)

and is shown in Figure S2.1. $\Pi$ is measured in Pa, [*PEG*] is measured in mol $m^{-3}$.

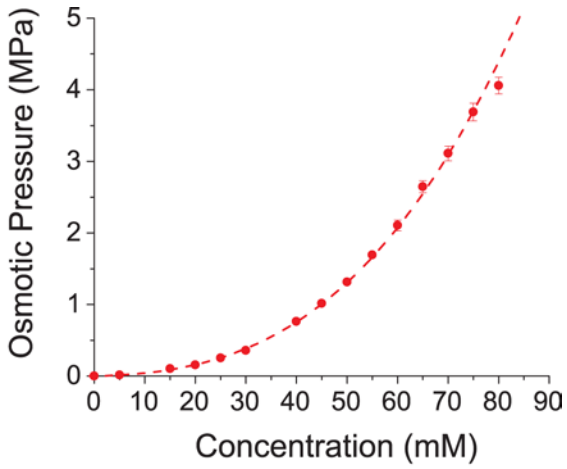


**Figure S2.1.** Osmotic pressure as a function of PEG concentration.

### S2.2 Determining $L_p$ from Volume Delivery

A straightforward method for determining the hydraulic permeability ($L_p$) of a dialysis cassette membrane is to perform a volume delivery experiment as described in the experimental

section. Assuming minimal cassette expansion and/or pressure generation within the cassette, the first derivative of volume delivered with respect to time will equal the volumetric flow rate ($Q$) into the cassette, which is equal to $J_v * A$. These assumptions are more likely to be valid at the beginning of data collection as the influence of extenuating factors like imperfect mixing in the cassette upon influx of water, evaporation, and working fluid loss will grow over time.

From Equation 2.1 in the main text where $\sigma = 1$ and $\Delta P = 0$, we obtain

$$L_p = \frac{Q}{A * \Delta\Pi} \tag{S2.2}$$

The membrane area, $A$, can be measured for each device. $Q$ is equal to the initial slope of the volume delivered *vs.* time curve, which can easily be determined by fitting the initial portion of this data with a line after any artifacts resulting from cassette submersion have passed. $\Delta\Pi$ can be determined from the initial concentration of the working fluid and the relation in Appendix S2.1. The filtration coefficient, $L_p$, can then be obtained from Equation S2.2.

**S2.3. Discussion of Correction to $L_p$**

The trend in effective $L_p$ observed from volume delivery experiments can be seen in Figure S2.2A. Processes involving semipermeable membranes often involve concentration polarization (CP) or membrane fouling; each of these conditions lowers the osmotic driving force and could explain the trend.[24]

First, we considered CP, of which there are four types. The conditions of our experiment led us to rule out some of these: we did not use an asymmetric membrane containing an active layer and a support layer, nor did we have an appreciable amount of solute in our "feed" solution.[4] With these considerations, the only type of CP that applies to our experiments is called dilutive external CP, in which the incoming water displaces the solute near the membrane inside

the cassette. The correction that accounts for this involves multiplying the $\Delta\Pi$ term in Equation 2.1 by a CP modulus:

$$\frac{\pi_{\mathrm{D,m}}}{\pi_{\mathrm{D,b}}} = e^{\frac{-J_v\, d_h}{Sh\, D}} \tag{S3}$$

For our experimental conditions, the CP modulus is approximately 1, meaning the effects of CP are negligible.[25] This agrees with an assertion made in Ullmann's Encyclopedia of Industrial Chemistry that the laminar boundary layer inside which CP takes place in is too thin compared to the thickness of a dialysis membrane to have a strong effect.[24]

Membrane fouling effects involve blockage of flow via the accumulation of solute at the membrane surface and are complex, diverse, and difficult to model.[24] We decided to determine the $L_p$ for each MWCO in the absence of PEG ($L_{p,0}$) by following the "Pumping Experiment for $L_{p,0}$ Determination" procedure in the Materials and Methods section of the main text. This yielded a flux value, $\frac{dz}{dt}$, which could be converted into an $L_{p,0}$ according to a modified version of Equation S2.2:

$$L_{p,0} = \frac{dz/dt\, A_{tube}}{A_{mem} * \Delta P} \tag{S2.4}$$

where $A_{tube}$ is the cross-sectional area of the thin tubing where the meniscus was monitored, $A_{mem}$ is the estimated total membrane area, and $\Delta P$ is the applied pressure.

As predicted, $L_{p,0}$ was higher than the effective $L_p$ values measured for both MWCO membranes in the presence of PEG (Figure S2.2A). As a result, we modeled the effective $L_p$ value as $L_{p,0}(1 - f)$, where $f$ is a scaling factor that describes the decrease in effective $L_p$ with increasing PEG concentration. When plotted against PEG concentration, $f$ was well-described by the Hill equation ($R^2 > 0.98$), which describes cooperative binding of ligands to binding sites and

takes the form $f = \frac{[PEG]^n}{[PEG]^n + k^n}$ (Figure S2.2B).[56] This adherence to a binding curve supports the hypothesis that the membrane is being fouled by PEG molecules, so we named *f* the "fouling factor."

The best-fit values of the Hill equation fitting parameters for each MWCO are as follows:

2.0 kDa: $n$ = 2.397, $k$ = 0.322, $R^2$ = 0.98, N = 5

3.5 kDa: $n$ = 1.613, $k$ = 0.0139, $R^2$ = 0.999, N = 5

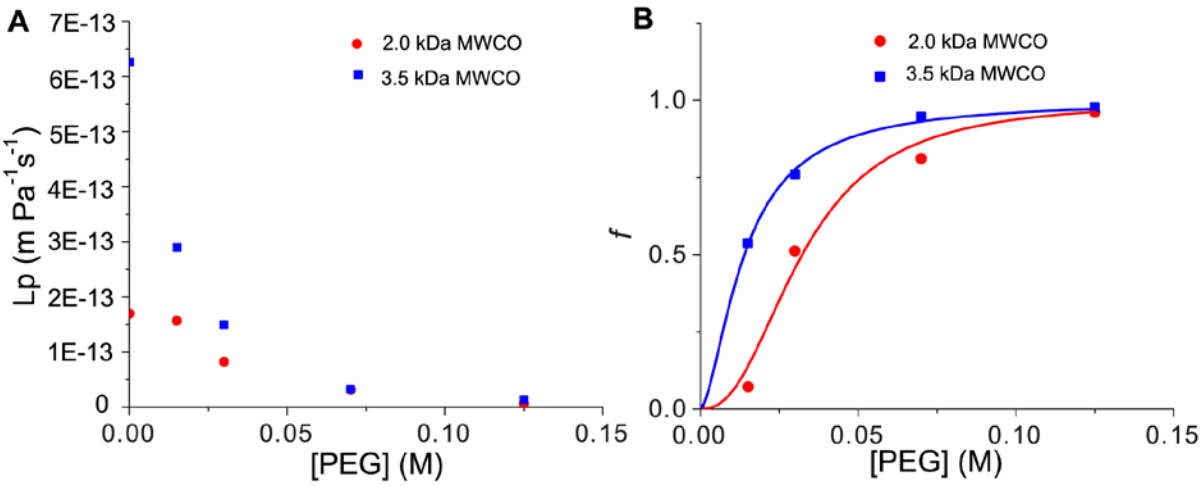


**Figure S2.2.** Effects of Membrane Fouling at Increasing PEG Concentrations. **A**. Effective $L_p$ values calculated from volume delivery experiments as described in Appendix S2 at different PEG concentrations and MWCOs. The $L_p$ value in the absence of PEG, $L_{p,0}$, was determined by the procedure in Appendix 3. **B**. The fouling factor *f* at different PEG concentrations and MWCOs. *f* is determined by $f = 1 - \frac{L_p}{L_{p,0}}$ and has been fit with the Hill equation.

### S2.4. Determination of $V_{in}(P_{in})$

*General Procedure*: The dialysis cassette and pressure transducer were prepared as described in the Experimental Section, although water was used as the working fluid and the cassettes were initially filled to their advertised capacity (3 or 30 mL). A syringe filled with

Milli-Q water was fitted with rigid tubing and a needle was connected to the submerged dialysis cassette. A syringe pump was used to compress the syringe at a rate of 1 mL/minute; simultaneously, pressure was recorded. The procedure was repeated for each cassette and restraint condition. Recording continued until cassette failure. The line representing $V_{in}$(t) was plotted against $P_{in}$(t) and fitted with a fifth-order polynomial representing $V_{in}(P_{in})$.

*Curves*:

0.5-3 mL, 2 kDa MWCO cassettes, restrained:

$$V_{in} = \left(4.4214 * 10^{-6}\ \mathrm{m}^3\right) + \left(8.04609 * 10^{-11}\ \mathrm{m}^3\ \mathrm{Pa}^{-1}\right) P_{in} + \left(-3.07174 * 10^{-15}\ \mathrm{m}^3\ \mathrm{Pa}^{-2}\right) P_{in}^{\ 2} + \left(6.68335 * 10^{-20}\ \mathrm{m}^3\ \mathrm{Pa}^{-3}\right) P_{in}^{\ 3} + \left(-7.40082 * 10^{-25}\ \mathrm{m}^3\ \mathrm{Pa}^{-4}\right) P_{in}^{\ 4} + \left(3.40544 * 10^{-30}\ \mathrm{m}^3\ \mathrm{Pa}^{-5}\right) P_{in}^{\ 5}$$

0.5 – 3 mL, 3.5 kDa MWCO cassettes, restrained:

$$V_{in} = \left(5.7711 * 10^{-6}\ \mathrm{m}^3\right) + \left(3.69131 * 10^{-11}\ \mathrm{m}^3\ \mathrm{Pa}^{-1}\right) P_{in} + \left(-1.16582 * 10^{-15}\ \mathrm{m}^3\ \mathrm{Pa}^{-2}\right) P_{in}^{\ 2} + \left(2.1355 * 10^{-20}\ \mathrm{m}^3\ \mathrm{Pa}^{-3}\right) P_{in}^{\ 3} + \left(-1.6605 * 10^{-25}\ \mathrm{m}^3\ \mathrm{Pa}^{-4}\right) P_{in}^{\ 4} + \left(4.73849 * 10^{-31}\ \mathrm{m}^3\ \mathrm{Pa}^{-5}\right) P_{in}^{\ 5}$$

0.5-3 mL, 2 kDa MWCO cassettes, unrestrained:

$$V_{in} = \left(6.03765 * 10^{-6}\ \mathrm{m}^3\right) + \left(1.69831 * 10^{-11}\ \mathrm{m}^3\ \mathrm{Pa}^{-1}\right) P_{in} + \left(-6.64465 * 10^{-15}\ \mathrm{m}^3\ \mathrm{Pa}^{-2}\right) P_{in}^{\ 2} + \left(1.93811 * 10^{-19}\ \mathrm{m}^3\ \mathrm{Pa}^{-3}\right) P_{in}^{\ 3} + \left(-2.65978 * 10^{-24}\ \mathrm{m}^3\ \mathrm{Pa}^{-4}\right) P_{in}^{\ 4} + \left(1.38578 * 10^{-29}\ \mathrm{m}^3\ \mathrm{Pa}^{-5}\right) P_{in}^{\ 5}$$

0.5-3 mL, 3.5 kDa MWCO cassettes, restrained:

$$V_{in} = \left(4.49345 * 10^{-6}\ \mathrm{m}^3\right) + \left(7.50511 * 10^{-10}\ \mathrm{m}^3\ \mathrm{Pa}^{-1}\right) P_{in} + \left(-7.76213 * 10^{-14}\ \mathrm{m}^3\ \mathrm{Pa}^{-2}\right) P_{in}^{\ 2} + \left(5.07533 * 10^{-18}\ \mathrm{m}^3\ \mathrm{Pa}^{-3}\right) P_{in}^{\ 3} + \left(-1.55112 * 10^{-22}\ \mathrm{m}^3\ \mathrm{Pa}^{-4}\right) P_{in}^{\ 4} + \left(1.85547 * 10^{-27}\ \mathrm{m}^3\ \mathrm{Pa}^{-5}\right) P_{in}^{\ 5}$$

For all curves, $P_{in}$ is measured in Pa, $V_{in}$ is measured in $m^3$ and $R^2 > 0.999$.

**Video S2.1. Actuation of soft robot attached to a pressure generator.**

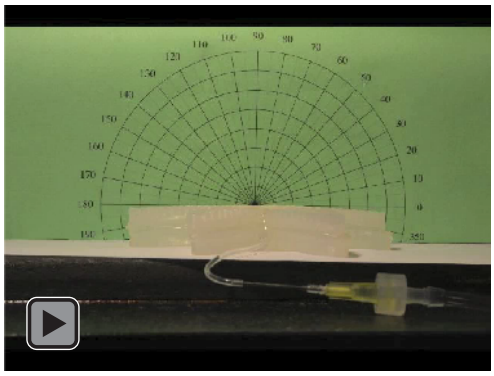

## References


1. Bruhn, B. R. *et al.* Osmosis-Based Pressure Generation: Dynamics and Application. *PLoS ONE* **9,** e91350 (2014).

2. Stroock, A. D., Pagay, V. V., Zwieniecki, M. A. & Holbrook, N. M. The Physicochemical Hydrodynamics of Vascular Plants. *Annu. Rev. Fluid Mech.* (2013).

3. Dumais, J. & Forterre, Y. "Vegetable Dynamicks": The Role of Water in Plant Movements. *Annu. Rev. Fluid Mech.* **44,** 453–478 (2012).

4. Cath, T. Y., Childress, A. E. & Elimelech, M. Forward osmosis: Principles, applications, and recent developments. *J. Membr. Sci.* **281,** 70–87 (2006).

5. McGinnis, R. L., McCutcheon, J. R. & Elimelech, M. A novel ammonia–carbon dioxide osmotic heat engine for power generation. *J. Membr. Sci.* **305,** 13–19 (2007).

6. Achilli, A., Cath, T. Y. & Childress, A. E. Power generation with pressure retarded osmosis: An experimental and theoretical investigation. *J. Membr. Sci.* **343,** 42–52 (2009).

7. Logan, B. E. & Elimelech, M. Membrane-based processes for sustainable power generation using water. *Nature* **488,** 313–319 (2012).

8. Achilli, A. & Childress, A. E. Pressure retarded osmosis: From the vision of Sidney Loeb to the first prototype installation — Review. *Desalination* **261,** 205–211 (2010).

9. International Energy Agency. *World energy outlook.* (International Energy Agency, 2012).

10. Benedek, G. B. & Villars, F. M. H. *Physics with Illustrative Examples from Medicine and Biology: Statistical Physics*. (Springer-Verlag, 2000).

11. Theeuwes, F. Elementary osmotic pump. *J. Pharm. Sci.* **64,** 1987–1991 (1975).

12. Theeuwes, F. & Yum, S. I. Principles of the design and operation of generic osmotic pumps for the delivery of semisolid or liquid drug formulations. *Ann. Biomed. Eng.* **4,** 343–353 (1976).

13. Good, B. T., Bowman, C. N. & Davis, R. H. A water-activated pump for portable microfluidic applications. *J. Colloid Interface Sci.* **305,** 239–249 (2007).

14. Rose, S. & Nelson, J. F. A Continuous Long-Term Injector. *Aust. J. Exp. Biol. Med. Sci.* **33,** 415–420 (1955).

15. Will, P. C., Cortright, R. N. & Hopfer, U. Polyethylene Glycols as Solvents in Implantable Osmotic Pumps. *J. Pharm. Sci.* **69,** 747–749 (1980).

16. Liu, L. & Wang, X. Solubility-modulated monolithic osmotic pump tablet for atenolol delivery. *Eur. J. Pharm. Biopharm.* **68,** 298–302 (2008).

17. Swanson, D. R., Barclay, B. L., Wong, P. S. & Theeuwes, F. Nifedipine gastrointestinal therapeutic system. *Am. J. Med.* **83,** 3–9 (1987).

18. Yu-Chuan Su, Liwei Lin & Pisano, A. P. A water-powered osmotic microactuator. *J. Microelectromechanical Syst.* **11,** 736–742 (2002).

19. Sundaresan, V. B., Homison, C., Weiland, L. M. & Leo, D. J. Biological transport processes for microhydraulic actuation. *Sens. Actuators B Chem.* **123,** 685–695 (2007).

20. Sundaresan, V. B. & Leo, D. J. Modeling and characterization of a chemomechanical actuator using protein transporter. *Sens. Actuators B Chem.* **131,** 384–393 (2008).

21. Ilievski, F., Mazzeo, A. D., Shepherd, R. F., Chen, X. & Whitesides, G. M. Soft Robotics for Chemists. *Angew. Chem. Int. Ed.* **50,** 1890–1895 (2011).

22. Money, N. P. Osmotic pressure of aqueous polyethylene glycols relationship between molecular weight and vapor pressure deficit. *Plant Physiol.* **91,** 766–769 (1989).

23. Pinho, S. P. & Macedo, E. A. Solubility of NaCl, NaBr, and KCl in Water, Methanol, Ethanol, and Their Mixed Solvents. *J. Chem. Eng. Data* **50,** 29–32 (2005).

24. Strathmann, H. Membrane Separation Processes, 4. Concentration Polarization and Membrane Fouling. in *Ullmann's Encyclopedia of Industrial Chemistry* (Wiley-VCH Verlag GmbH & Co. KGaA, 2000).

25. McCutcheon, J. R. & Elimelech, M. Influence of concentrative and dilutive internal concentration polarization on flux behavior in forward osmosis. *J. Membr. Sci.* **284,** 237–247 (2006).

26. CRC Handbook of Chemistry and Physics. in (ed. Haynes, W. M.) (CRC Press, 2013).

27. Eliassi, A., Modarress, H. & Mansoori, G. A. Densities of poly (ethylene glycol)+ water mixtures in the 298.15-328.15 K temperature range. *J. Chem. Eng. Data* **43,** 719–721 (1998).

28. Mayer, W.-E., Flach, D., Raju, M. V. S., Starrach, N. & Wiech, E. Mechanics of circadian pulvini movements in Phaseolus coccineus L. *Planta* **163,** 381–390 (1985).

29. Moshelion, M. *et al.* Plasma Membrane Aquaporins in the Motor Cells of Samanea saman. *Plant Cell* **14,** 727–739 (2002).

30. Gorton, H. L. Water Relations in Pulvini from Samanea saman: I. Intact Pulvini. *Plant Physiol.* **83,** 945–950 (1987).

31. Zimmermann, U. & Steudle, E. Physical Aspects of Water Relations of Plant Cells. in *Advances in Botanical Research* (ed. H.W. Woolhouse) **Volume 6,** 45–117 (Academic Press, 1979).

32. Hill, B. S. & Findlay, G. P. The power of movement in plants: the role of osmotic machines. *Q. Rev. Biophys.* **14,** 173–222 (1981).

33. Samejima, M. & Sibaoka, T. Changes in the extracellular ion concentration in the main pulvinus of Mimosa pudica during rapid movement and recovery. *Plant Cell Physiol.* **21,** 467–479 (1980).

34. Fleurat-Lessard, P. Structural and Ultrastructural Features of Cortical Cells in Motor Organs of Sensitive Plants. *Biol. Rev.* **63,** 1–22 (1988).

35. Allen, R. D. Studies of the Seismonastic Reaction in the Main Pulvinus of Mimosa Pudica. (University of California, Los Angeles, 1967).

36. Kagawa, H. & Saito, E. A Model on the Main Pulvinus Movement of Mimosa Pudica. *JSME Int. J.* **43,** 923–928 (2000).

37. Martinez, R. V., Fish, C. R., Chen, X. & Whitesides, G. M. Elastomeric Origami: Programmable Paper-Elastomer Composites as Pneumatic Actuators. *Adv. Funct. Mater.* **22,** 1376–1384 (2012).

38. Martinez, R. V. *et al.* Robotic Tentacles with Three-Dimensional Mobility Based on Flexible Elastomers. *Adv. Mater.* **25,** 205–212 (2013).

39. Shepherd, R. F. *et al.* Multigait soft robot. *Proc. Natl. Acad. Sci.* **108,** 20400–20403 (2011).

40. Sharpe, Peter J. H., Wu, Hsin-i & Spence, Richard D. Stomatal Mechanics. in *Stomatal Function* (eds. Zeiger, E., Farquhar, G. D. & Cowan, I. R.) (Stanford University Press, 1987).

41. Iverson, B. D. & Garimella, S. V. Recent advances in microscale pumping technologies: a review and evaluation. *Microfluid. Nanofluidics* **5,** 145–174 (2008).

42. Walker, G. M. & Beebe, D. J. A passive pumping method for microfluidic devices. *Lab. Chip* **2,** 131–134 (2002).

43. Bessoth, F. G., deMello, A. J. & Manz, A. Microstructure for efficient continuous flow mixing. *Anal. Commun.* **36,** 213–215 (1999).

44. Erbacher, C., Bessoth, F. G., Busch, M., Verpoorte, E. & Manz, A. Towards Integrated Continuous-Flow Chemical Reactors. *Microchim. Acta* **131,** 19–24 (1999).

45. Kopp, M. U., Mello, A. J. de & Manz, A. Chemical Amplification: Continuous-Flow PCR on a Chip. *Science* **280,** 1046–1048 (1998).

46. Laurell, T., Drott, J. & Rosengren, L. Silicon wafer integrated enzyme reactors. *Biosens. Bioelectron.* **10,** 289–299 (1995).

47. Huang, S.-B., Wu, M.-H., Cui, Z., Cui, Z. & Lee, G.-B. A membrane-based serpentine-shape pneumatic micropump with pumping performance modulated by fluidic resistance. *J. Micromechanics Microengineering* **18,** 045008 (2008).

48. Kim, Y., Kuczenski, B., LeDuc, P. R. & Messner, W. C. Modulation of fluidic resistance and capacitance for long-term, high-speed feedback control of a microfluidic interface. *Lab. Chip* **9,** 2603 (2009).

49. Leslie, D. C. *et al.* Frequency-specific flow control in microfluidic circuits with passive elastomeric features. *Nat. Phys.* **5,** 231–235 (2009).

50. Mescher, M. J. *et al.* Fabrication Methods and Performance of Low-Permeability Microfluidic Components for a Miniaturized Wearable Drug Delivery System. *J. Microelectromechanical Syst.* **18,** 501–510 (2009).

51. Sewell, W. F. *et al.* Development of a Microfluidics-Based Intracochlear Drug Delivery Device. *Audiol. Neurotol.* **14,** 411–422 (2009).

52. Herz, M., Horsch, D., Wachutka, G., Lueth, T. C. & Richter, M. Design of ideal circular bending actuators for high performance micropumps. *Sens. Actuators Phys.* **163,** 231–239 (2010).

53. Gong, M. M., MacDonald, B. D., Vu Nguyen, T. & Sinton, D. Hand-powered microfluidics: A membrane pump with a patient-to-chip syringe interface. *Biomicrofluidics* **6,** 044102 (2012).

54. Kim, S.-J., Yokokawa, R. & Takayama, S. Microfluidic oscillators with widely tunable periods. *Lab. Chip* **13,** 1644 (2013).

55. Mayer, M., Genrich, M., Künnecke, W. & Bilitewski, U. Automated determination of lactulose in milk using an enzyme reactor and flow analysis with integrated dialysis. *Anal. Chim. Acta* **324,** 37–45 (1996).

56. Hill, A. V. The possible effects of the aggregation of the molecules of haemoglobin on its dissociation curves. PROCEEDINGS OF THE PHYSIOLOGICAL SOCIETY: January 22, 1910. *J. Physiol.* **40,** i–vii (1910).

# CHAPTER 3

## Effects of Transmembrane Tethers in Extremophile-Inspired Lipid Membranes on $H^+/OH^-$ Flux at Room Temperature

This work explores the proton/hydroxide permeability ($P_{H+/OH-}$) of membranes that were made of synthetic extremophile-inspired phospholipids with systematically varied structural elements. A fluorescence-based permeability assay was optimized to determine the effects on the $P_{H+/OH-}$ through liposome membranes with variations in the following lipid attributes: transmembrane tethering, tether length, and the presence of isoprenoid methyl groups on one or both lipid tails. All permeability assays were performed in the presence of a low concentration of valinomycin (10 nM) to prevent buildup of a membrane potential without artificially increasing the measured $P_{H+/OH-}$. The presence of a transmembrane tether did not impact $P_{H+/OH-}$ at room temperature. Among tethered lipid monolayers, $P_{H+/OH-}$ increased with increasing tether length if the number of carbons in the untethered acyl tail was constant. Untethered lipids with two isoprenoid methyl tails led to lower $P_{H+/OH-}$ values than lipids with only one or no isoprenoid tails. Molecular dynamics simulations revealed a strong positive correlation between the probability of observing clusters of water molecules in the hydrophobic core of these lipid membranes and their proton permeability.

This work is reprinted from Biophysical Journal, Vol. 110, Thomas B. H. Schroeder *et al.*, "Effects of Lipid Tethering in Extremophile-Inspired Lipid Membranes on $H^+/OH^-$ Flux at Room Temperature," pages 2430-2440, copyright 2016, with permission from Elsevier.[1]

## 3.1 Introduction

Acidophilic archaea have adapted to thrive in environments with very low pH.[2] These organisms often rely on the acidity of their habitats to survive; archaea of the *Picrophilus* family, for example, have an optimal exterior pH of 0.7 and cannot grow above pH 3.5.[3] A large pH gradient (ΔpH) across the cell membrane is necessary both to maintain a near-neutral internal pH and to drive vital cell functions such as energy transduction with membrane-bound ATPases which use proton flux driven by ΔpH to drive ATP production.[4,5]

Acidophiles have evolved a number of mechanisms to maintain a gradient of several pH units across the cell membrane. For one, many such organisms express a variety of active transport systems to pump protons out of the cell;[5–7] genetic evidence suggests that some form of proton efflux system exists in all acidophiles whose genomes have been sequenced.[5] Additionally, unlike cells that grow in neutral environments, many acidophiles display a positive membrane potential that opposes proton influx.[5] Finally, the cell membrane itself is often composed of lipids with unique structural characteristics thought to reduce proton permeability.[5,8] These lipids usually contain ether bonds connecting the head glycerol group to the tails, increasing their chemical stability and potentially inhibiting the formation of transient hydrogen-bonded water chains compared to the ester bonds in standard phospholipids.[9] Archaeal lipid tails often contain methyl branches in a repeating isoprenoid pattern as well as cyclopentane and cyclohexane rings. Most unusually, many acidophile lipids are membrane-spanning structures with two tethered hydrophilic head groups; typically these are macrocycles with two tethering alkyl chains, but some have one tether and one free-hanging tail attached to each head group.[10] Both the tethered/untethered ratio[11] and ring count[12–14] of lipids in thermoacidophilic archaea have been shown to increase with culture temperature, implying that these adaptations

and the related biosynthetic pathways are related to heat-stability. In addition, membranes formed from extracts of archaeal lipids are more resistant to ΔpH relaxation than those formed from *E. coli* extracts even at room temperature.[8]

Passive permeation of protons across membranes in aqueous systems is mechanistically different and significantly faster than permeation of other polar or charged molecules, though the exact mechanism is still not known. In this context, it is important to note that discussion of "proton permeation" actually represents a discussion of the permeation of protons, hydroxide ions, or both, as it is practically impossible to distinguish between a flux of protons in one direction and a flux of hydroxide ions in the other. The proposed modes of $H^+/OH^-$ flux that have historically received the most attention tend to rely on the ability of protons to "hop" between hydrogen-bonded water molecules, an idea first described by Grotthuss in 1806.[15] Despite this long history, the specifics of this mechanism are still being resolved,[16] but most membrane $H^+/OH^-$ permeation models propose the formation of short-lived clusters or wires of water across the membrane.[17–19] Paula *et al*. presented data consistent with this model in systems of liposome membranes with thin hydrophobic regions (< 3.1 nm), whereas thicker hydrophobic regions (≥ 3.4 nm) were better described by a solubility-diffusion mechanism involving $H_9O_4^+$.[20] In 2010, Nichols and Abercrombie proposed a five-step "transmembrane condensation model" in which a proton and a hydroxide anion spontaneously appear on either side of a membrane, interact electrostatically across the membrane, and in rare cases one species or the other overcomes its Born energy barrier and penetrates into the hydrophobic core, likely in the form of a cluster of water molecules (rendering it potentially consistent with the transient water wire hypothesis).[21] Whatever the mechanism, the permeation of protons or hydroxide ions is conventionally described by a permeability coefficient $P_{H+/OH-}$ in units of cm $s^{-1}$ defined by Fick's law (Eq. 1):

$$J = P_{H^+/OH^-} \times \Delta C \quad (1)$$

where $J$ (mol $m^{-2}$ $s^{-1}$) is the inward flux of solute across the membrane, $P_{H+/OH-}$ (m $s^{-1}$) is the permeability of the membrane, and $\Delta C$ (mol $m^{-3}$) is the concentration gradient across the membrane.

Widely varying values of $P_{H+/OH-}$ have been observed both between and within laboratories. Reported $P_{H+/OH-}$values for membranes composed of the lipid POPC, for example, include values on the order of $10^{-1}$ cm $s^{-1}$,[22] $10^{-2}$ cm $s^{-1}$,[23] $10^{-5}$ cm $s^{-1}$,[24] and $10^{-7}$ cm $s^{-1}$;[25,26] these disparate values were all similarly obtained by subjecting liposomes to a stepwise ΔpH and observing proton flux over time. Mathai *et al*. attribute at least some of this orders-of-magnitude variability to differences in the size of the gradient imposed during the assays, prescribing the use of a small ΔpH of 0.5.[9] Recommendations such as this are sensible; there is a clear need for a standard, well-defined assay for permeation of $H^+/OH^-$ across membranes so that $P_{H+/OH-}$values obtained by different groups can be compared. However, Kuyper *et al*. analyzed $H^+/OH^-$ permeation across hundreds of single vesicles in parallel and observed a high degree of variation in $P_{H+/OH-}$ between liposomes in the same experiment without observing correlation with liposome size or any other observable parameter, indicating that broad distributions of $P_{H+/OH-}$ values may be unavoidable.[25] This result was obtained from ensemble measurements as well; Van de Vossenberg *et al*. recorded a spread of nearly an order of magnitude in permeation rate constants in liposomes containing lipids from *B. subtilis*.[27]

In an attempt to obtain consistent readings of this notoriously fickle parameter, we have optimized an established liposome-based assay for $P_{H+/OH-}$ developed by Paula *et al*. that tracks

the fluorescence decay of an encapsulated pH-sensitive dye in response to a step change in the external pH.[20] To this end, we have developed a fitting procedure that incorporates empirical measurements of buffering activity and fluorescent response to pH taken during an internal calibration into an algorithm that fits the entire decay curve obtained during each experiment. We have also determined a concentration range in which the ionophore valinomycin is selective for $K^+$ over $H^+$ in order to eliminate the membrane potential that would arise from imposing a concentration gradient on a system with a single mobile ion while minimizing possible artifacts in the measured $H^+/OH^-$ permeability due to valinomycin-induced proton flux.

To enable this study, we synthesized a series of extremophile-inspired lipids composed of two glycerophosphocholine heads connected by a membrane-spanning *n*-alkyl tether with each head ether-bonded to a phytanyl chain (T28, T32, and T36, Fig. 3.1 A-C) as well as several untethered lipids (U16, Di-O-PhyPC, DiPhyPC, and POPC Fig. 3.1 D-G) to seek answers to our questions about structure-permeability relationships of liposomes from pure lipid preparations at room temperature: First, how does the presence of a single tether between two lipid head groups affect $P_{H+/OH-}$ compared to the absence of a tether? Second, how does the length of the tether affect $P_{H+/OH-}$ permeability when the lengths of the untethered phytanyl chains are kept constant at 16 carbons? And third, how does the $P_{H+/OH-}$ of an untethered lipid with a repeating isoprenoid methyl motif on one of its tails compare to that of a lipid with the methyl groups on both tails?

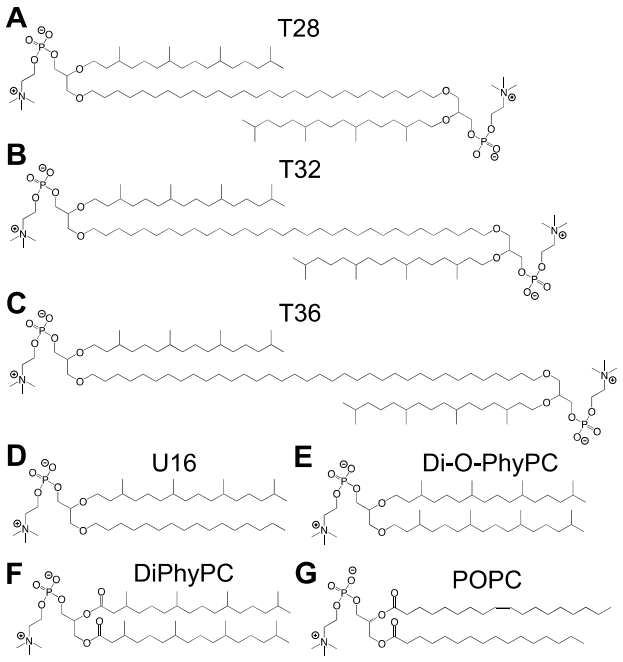


**Figure 3.1**. Extremophilic archaea-inspired lipid structures examined in this work. **A.** Lipid with a tether length of 28 carbons (T28). **B.** Lipid with a tether length of 32 carbons (T32). **C.** Lipid with a tether length of 36 carbons (T36). **D.** Untethered lipid equivalent to half of T32 (U16). **E.** 1,2-di-O-phytanyl-sn-glycero-3-phosphocholine (Di-O-PhyPC) **F.** 1,2-diphytanoyl-*sn*-glycero-3-phosphocholine (DiPhyPC) **G.** 1-palmitoyl-2-oleoyl-sn-glycero-3-phosphocholine (POPC).

## 3.2 Materials and Methods

The lipids shown in Fig. 3.1 A-D were synthesized as shown in the Supporting Material (sections 3-4) of Schroeder *et al.*[1] POPC, DiPhyPC, and Di-O-PhyPC were from Avanti Polar Lipids (Alabaster, Alabama); pyranine was from Sigma-Aldrich.

*Preparation and Sizing of Unilamellar Liposomes*

We formed a homogeneous lipid film on the bottom of a 10 mL round-bottom flask via gentle rotary evaporation of a 1 mL solution of lipid in chloroform (10 mM for lipids with one head group; 5 mM for bipolar lipids). We hydrated the film with 1 mL of a buffered aqueous solution containing 50 μM pyranine, 50 mM $K_2SO_4$, 10 mM N-(2-Acetamido)-2-aminoethanesulfonic acid (ACES), 10 mM 2-(*N*-morpholino)ethanesulfonic acid (MES), 10 mM N-[Tris(hydroxymethyl)methyl]-2-aminoethanesulfonic acid (TES), and 10 mM tricine at pH

7.25 and heated the flask to 37 ºC in a water bath for ≥ 3 hours. After transferring the resulting solution of liposomes to an Eppendorf tube, we performed 15 freeze-thaw cycles in which we alternated between flash-freezing the solution in liquid nitrogen for 30 s and thawing it in a water bath at 45 ºC for three minutes.

Exercising care to avoid the formation of bubbles, we pushed the solution 7 times through a polycarbonate membrane with pores of known diameter with a Mini-Extruder (Avanti Polar Lipids, Alabaster, Alabama). We obtained the resulting size distribution of liposomes within the solution via dynamic light scattering (DLS) using a 90Plus Particle Sizer (Brookhaven Instruments Corporation, Holtsville, New York). We then pushed the liposome solution another 21 times through a polycarbonate membrane with pores of a diameter below the smallest diameters of the size distribution shown on the DLS readout (we usually used 80 nm pores) in order to minimize the probability of liposomes crossing the membrane without breaking into smaller vesicles, thereby maximizing the probability of obtaining a homogeneous solution of unilamellar liposomes.[28] We determined the new size distribution using DLS and used the mode of the distribution to calculate the radius used in the fitting equation. We also determined via DLS that liposomes formed in this way did not undergo significant changes in size distribution for at least three days.

*Optimized Fluorescence-based Permeation Assay*

We removed all extravesicular pyranine by running the liposome solution sequentially through two PD-10 desalting columns (GE Healthcare) with an eluent identical to the incubation buffer solution but without pyranine, collecting fractions of 1 mL each. We found that using one desalting column was insufficient and resulted in a significant concentration of pyranine

remaining outside the vesicles. We transferred a 1 mL fraction containing liposomes to a cuvette, then added 1 µL of a solution of valinomycin (10 µM in DMSO) to reach a final concentration of 10 nM and mixed by gentle pipetting.

After 30 min, we measured the extravesicular pH of the solution with a calibrated Orion 5-Star pH meter (Thermo Scientific). We used a Fluorolog spectrofluorometer (Horiba Jobin Yvon) to collect fluorescence measurements over time. Every 2.5 s, the instrument collected one pH-invariant fluorescence intensity value by exciting the sample with a wavelength of 415 nm and collecting emission at 510 nm and one pH-dependent value by exciting at 450 nm and collecting at 510 nm (excitation and emission band pass = 1 nm, integration time = 0.5 s). Before imposing the ΔpH, we collected an initial fluorescence measurement for 30 s in order to ensure that no discernible change in the fluorescence intensity was occurring over time at either excitation wavelength. We then added 10 µL of an aqueous solution of $H_2SO_4$ (250 mM) to the cuvette, mixed by pipetting up and down, and began collecting fluorescence data as quickly as possible, recording the duration that passed between acid addition and the start of fluorescence data collection. This addition of acid induced a pH change from 7.25 to approximately 6.75.

After the resulting fluorescence decay curve had been recorded, we added 0.67 µL of a solution of the protonophore nigericin in ethanol (100 µM) to render the vesicle membrane permeable to protons, mixed by pipetting up and down, measured and recorded the pH with a pH meter, and continued to record the fluorescence. We then proceeded to add 5 “calibration jumps” of 2 µL aqueous KOH solution (500 mM), measuring the pH and recording the fluorescence until a stable baseline was reached before moving to the next jump. The final pH of the vesicle solution was approximately 7.25.

After data collection was complete, we modified the time values of the fluorescence curves to reflect the delay between acid addition and the start of the fluorescence data and added a point at t = 0 corresponding to the initial fluorescent value measured before the pH jump. We then made scatter plots from the data collected during calibration relating the pH, the ratio of the fluorescence intensities $I_{450}/I_{415}$, and the added acid concentration $[H^+]_{cross}$; we fit these plots with exponential functions to obtain empirical fitting parameters $A_1$, $A_2$, $x_1$, $x_2$, $y_1$, and $y_2$ (Fig. 3.2 B, C). Finally, we plotted $I_{450}/I_{415}$ vs. time and fit the decay portion of the curve up to the addition of nigericin with Eq. 2 (derived in the Calculation section)(Fig. 3.2 A):

$$\frac{I_{ex450}}{I_{ex415}} = A_2\left(\frac{[H^+]_{f,o} - y_1}{A_1 - Ce^{\frac{3P_{H^+/OH^-}(y_1-[H^+]_{f,o})}{rx_1}t}}\right)^{-x_1/x_2} + y_2 \qquad (2)$$

where $[H^+]_{f,o}$ is the exterior proton concentration during the main decay phase obtained from the pH measured after nigericin is added, $A_1$ (mol $m^{-3}$), $A_2$ (unitless), $x_1$ (mol $m^{-3}$), $x_2$ (mol $m^{-3}$), $y_1$ (mol $m^{-3}$), and $y_2$ (unitless) are the empirical fitting parameters from the calibration fits (Fig. 3.2 B-C, explained in Calculation section), $C$ (mol $m^{-3}$) is a constant of integration, $P_{H+/OH-}$ (m $s^{-1}$) is the $H^+/OH^-$ permeability, $r$ (m) is the most probable liposome radius as determined by DLS, and $t$ (s) is time. The parameters $C$ and $P_{H+/OH-}$ are allowed to vary during fitting.

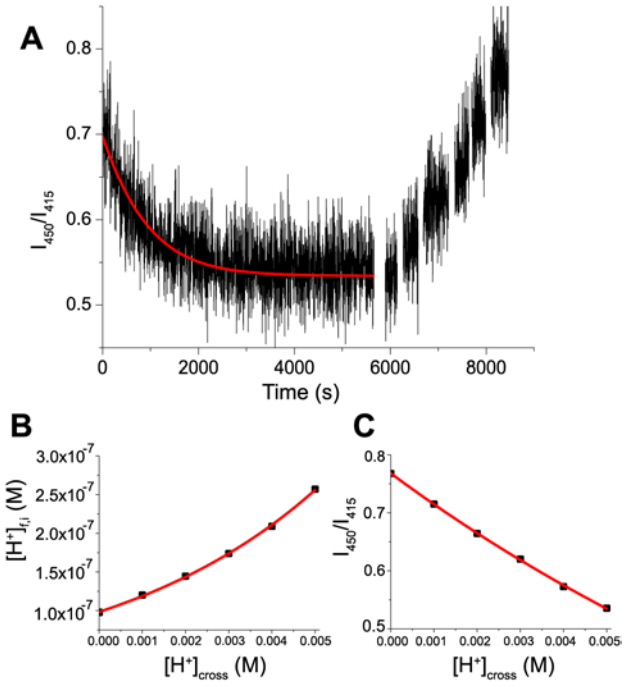


**Figure 3.2.** Determining proton permeability with liposomes that encapsulate the pH-sensitive, ratiometric fluorophore pyranine. **A.** Fluorescence emission ratio $I_{450}/I_{415}$ as a function of time after addition of acid to impose a pH jump with a best curve fit using Eq. 2. Nigericin was added around 5700 s; KOH was added during all subsequent breaks in the trace. **B.** Dependence of $[H+]_{f,i}$ as a function of $[H+]_{added}$ with an exponential curve fit to the equation $[H^+]_{f,i} = A_1 e^{[H^+]_{cross}/x_1} + y_1$. **C.** Dependence of the fluorescence emission ratio $I_{450}/I_{415}$ as a function of $[H+]_{added}$ with an exponential curve fit to the equation $\frac{I_{450}}{I_{415}} = A_2 e^{[H^+]_{cross}/x_2} + y_2$.

*Atomic Force Microscopy on Lipid Monolayers*

Liposomes composed of T28 and T36 were prepared by adding 10 µL of each lipid (10 mg/mL in an 80:20 chloroform:methanol solution) to round bottom flasks and removing the solvent by rotary evaporation; the lipid films were dried under high vacuum for ~1 h. An aqueous solution of 150 mM KCl and 10 mM HEPES at pH 7 was added to resuspend the lipids to a final lipid concentration of 0.1 mg/mL. The suspension was then incubated in a water bath at 50 °C for 30 min. The solutions containing lipids were sonicated for 5 min to form liposome suspensions. The solutions were added to a mica substrate and incubated for 1 h. The liposomes

were fused and ruptured on the mica substrate.[29–31] To remove excess liposomes, the mica surfaces were rinsed 10 times with a 150 mM KCl solution.

Samples were imaged by multimode atomic force microscope using a Nanoscope IV controller (Bruker, Santa Barbara, CA). The tapping mode images were acquired using silicon nitride cantilever tips submerged in buffer. A resonance frequency of ~8 kHz and drive amplitude under 100 mV were used (Asylum Research, Santa Barbara, CA). Nanoscope software was used for depth analysis to estimate the height of the lipid membranes.

*Molecular Dynamics Simulations*

The structural models for the archaea lipids were constructed and minimized using Maestro (Schrödinger LLC, New York, NY). The modeled lipids all had an all-trans conformation along the hydrocarbon chain. The single lipid was then translated and rotated along X and Y directions to build a smaller model membrane system comprising 81 lipids. Upon running equilibration simulations (50 ns) on this smaller membrane model, the equilibrated small membrane model was replicated in X and Y-axes to build a bigger membrane model of 729 total lipids (1458 in the case of U16). The dimensions of the bigger membrane models were in the range of 200 x 200 x 50 Å on average across the different membrane models. VMD was used to make the translations and rotations of lipid in building the membrane.[32] For POPC, we used the built-in membrane tool in VMD and produced a membrane of 1458 total lipids to match the sizes of the other systems. The simulation data from these larger membrane models were used for all subsequent simulations and calculations.

MD simulations for all membrane systems were performed for 100 ns after equilibration at pH 7, 300 K, and an ionic strength of 50 mM under isothermal-isobaric (NpT) ensemble. The

temperature was maintained by using the Nosé-Hoover chain method and the pressure was maintained at 1 atm. All the simulations were carried out using NAMD in explicit water using TIP3P water models.[33] The CHARMM36 lipid force field was used with a 10 Å cut-off for van der Waals with a 8.5 Å switching distance, and Particle Mesh Ewald for long-range electrostatics. Analysis was carried out on the final 50 ns of the simulation.

All post-simulation trajectory analyses were carried out using R (http://www.R-project.org). The bending rigidity, $k_c$, was determined by decomposing the fluctuation in membrane height, $\langle |h_q|^2 \rangle$, in terms of the wave number, q, based on the equation $\left\langle |h_q|^2 \right\rangle = \frac{k_B T}{2}\left(\frac{1}{k_C q^4} + \frac{1}{k_\theta q^2} + \frac{1}{k_\lambda}\right)$.[34] The entropy of the individual lipids was determined using the Schlitter formula $S = \frac{k_B}{2}\ln\det[\mathbf{I} + (kTe^2/\hbar^2)\mathbf{M}\sigma]$ where $\mathbf{M\sigma}$ is the mass-weighted covariance matrix calculated from the simulations.[35] Finally, the diffusion constants $D_1$ and $D_2$ were determined by fitting the mean-square displacement according to the formula $\left\langle x(t)^2 \right\rangle = \frac{4D_1 t r_o^2}{r_o^2 + 4D_1 t} + 4D_2 t$.[36]

To identify water in the core of the membrane, we chose to look for water molecules that penetrated past the ether or ester oxygens of the head groups and into the carbon-rich region. Since the membranes fluctuate in height, we did this search in a grid fashion across the full membrane surface and summed the results. The distributions of water numbers were all consistent with a Poisson process with p-values between 0.26 and 1 from a Kolmogorov-Smirnov test (500 data points each). The mean water per snapshot and its standard error were determined by maximum-likelihood expectation fit of the observed distribution to a Poisson

distribution, again using R. Water clusters were defined as groups of two or more water molecules within the hydrophobic core that were within 5 Å of each other.

### 3.3 Calculation of $H^+/OH^-$ Permeability

The permeability of a membrane to a solute is defined by Eq. 1. In spherical systems such as liposomes, the flux into the compartment can be related to the time derivative of the internal concentration by the continuity equation[37] (Eq. 3) for most solutes:

$$\frac{dC_i}{dt} = J\left(\frac{A}{V}\right) = \frac{3}{r} P_{H^+/OH^-}(C_o - C_i) \tag{3}$$

where $A$ ($m^2$) is the membrane area, $V$ ($m^3$) is the volume of the compartment, $r$ (m) is the radius of the spherical compartment, $C_o$ (mol $m^{-3}$) is the exterior concentration, and $C_i$ (mol $m^{-3}$) is the interior concentration. However, Eq. 3 must be modified to describe protons in buffered systems,[38] as protons on both sides of the membrane exist in chemical equilibrium with the protonated forms of buffering agents, fluorescent pH indicators, and lipid head groups. The protonation or deprotonation of buffer molecules occurs on time scales much faster than transport of protons across the membrane. It is therefore useful when thinking about proton flux to introduce the quantity $[H^+]_{cross}$, the net molar amount of protons that have crossed the membrane expressed as a concentration. The governing equation of the system is then Eq. 4:

$$\frac{d[H^+]_{cross}}{dt} = \left(\frac{3P_{H^+/OH^-}}{r}\right)([H^+]_{f,o} - [H^+]_{f,i}) \tag{4}$$

where $[H^+]_{f,i}$ is the concentration of "free" protons inside the liposome. For our systems, $[H^+]_{f,o}$ is assumed to be constant during the main decay phase of the experiment, as the volume of the liposomes is vanishingly small with respect to the volume of the bulk solution.

To solve differential Eq. 4, a functional relationship between $[H^+]_{f,i}$ and $[H^+]_{cross}$ is needed. Such a function quantifies how the amount of protons crossing the membrane affects the internal free proton concentration after buffering and can be obtained from the pH values gathered at each calibration jump after the liposome membranes have been permeabilized to protons via the addition of nigericin, since $[H^+]_{cross}$ at each jump is calculated from the concentrations of acid and base that have been added to the liposome solution. For example, in these experiments, $[H^+]_{cross}$ is zero before the initial acid aliquot is added and 5 mM after the addition of 2.5 mM $H_2SO_4$ and nigericin since 5 mM $H^+$ has crossed the membrane after it has been permeabilized. Subsequently, $[H^+]_{cross}$ decreases by 1 mM after adding each calibration aliquot of 1 mM KOH. The resulting plot of $[H^+]_{f,i}$ as a function of $[H^+]_{cross}$ (Fig. 3.2 B) can be fit well ($p < 0.0001$) with an exponential growth function with fitting parameters $A_1$, $x_1$, and $y_1$ which yields Eq. 5 when inserted into Eq. 4:

$$\frac{d[H^+]_{cross}}{dt} = \left(\frac{3P_{H^+/OH^-}}{r}\right)\left([H^+]_{f,o} - y_1 - A_1 e^{[H^+]_{cross}/x_1}\right) \tag{5}$$

Solving this ordinary differential equation for $[H^+]_{cross}(t)$ yields Eq. 6:

$$[H^+]_{cross}(t) = x_1 \ln\left(\frac{[H^+]_{f,o} - y_1}{A_1 - Ce^{\frac{3P_{H^+/OH^-}([H^+]_{f,o} - y_1)}{rx_1}t}}\right) \tag{6}$$

where C is a constant of integration. In order to obtain the final fitting formula, we substitute this equation for $[H^+]_{cross}$ into the exponential decay curve with parameters $A_2$, $x_2$, and $y_2$ obtained by fitting the values of $I_{450}/I_{415}$ as a function of $[H^+]_{cross}$ obtained during calibration (Fig. 3.2 C), yielding Eq. 2.

### 3.4 Results and Discussion

*Attempts to optimize an assay for $H^+/OH^-$ permeability*

We have adapted a fluorescence-based assay established by Paula *et al*. for ensemble measurements of the $H^+/OH^-$ permeability of large unilamellar vesicle (LUV) membranes.[20] We took advantage of the ratiometric quality of pyranine, a membrane-impermeant fluorophore whose fluorescence emission intensity at 510 nm varies with pH at an excitation wavelength of 450 nm but not at an excitation wavelength of 415 nm, making it possible to control for variations in dye concentration between liposome preparations by tracking the ratio between the wavelengths rather than a raw intensity value. Rossignol *et al*. used this property of the dye in 1981,[39] as did Grzesiek and Dencher in 1986,[38] but most studies using pyranine since then have neglected it.[8,20,27,40] Next, we developed a fitting function that makes full use of an internal calibration[20] in each experiment to minimize the assumptions we must make about buffer capacity and time-dependent changes in fluorescence intensity upon imposing a ΔpH. While many previous studies have calculated permeability using the initial slope of the fluorescence decay curve,[17,20,41] fitting with Eq. 2 allows us to make use of all the data collected and to validate the model based on quality of fit. Additionally, prior reports assumed linear buffering as pH changes[9,20,25] (often neglecting the buffering effects of lipid phosphate head groups[38]) and

made assumptions about fluorescent response to pH[20] and permeation mechanism [25] based on the fact that a single exponential function does not suffice to fit fluorescence decay curves well. Using each experiment's internal calibration enabled us to incorporate empirical measurements of the relationships between pH, buffering activity, and fluorescence intensity into the fitting function (Eq. 2), which produced excellent fits of the fluorescence decay curves after the addition of acid to the extravesicular solution ($p < 0.0001$). The permeability values we obtained for membranes from POPC and DiPhyPC lipids (Table 3.1) are in reasonable agreement with some literature values reported for POPC, $P_{H+/OH-} = 7 \times 10^{-5}$ cm/s,[24] and for DiPhyPC, $P_{H+/OH-} = 4.0 \times 10^{-6}$ cm/s,[42] $7.0 \times 10^{-6}$ cm/s.[43]

We performed all experiments in the presence of potassium ions and the $K^+$ ionophore valinomycin in solution in order to prevent the buildup of a membrane potential that would likely reduce the measured $H^+/OH^-$ flux.[20] Previous work indicates that at high valinomycin concentrations beginning at ~100 nM, membrane $H^+/OH^-$ permeability increases sharply with increasing valinomycin concentration.[17,44–46] At these elevated concentrations, valinomycin is therefore thought to display protonophoric activity in addition to ferrying $K^+$ ions;[44,45,47] in 2006, Kříž *et al*. provided NMR evidence for the existence of a $H_3O^+$-carrying valinomycin complex, reinforcing this conclusion.[48,49] We decided to experimentally establish an appropriate valinomycin concentration for the system by measuring the $H^+/OH^-$ permeability of POPC vesicles at different valinomycin concentrations. Our goal was to find a range in which liposomes would exhibit $P_{H+/OH-}$ values higher than in the absence of valinomycin, indicating that the buildup of a membrane potential accompanying $H^+$ diffusion was being successfully prevented via $K^+$ diffusion, but in which $P_{H+/OH-}$ was independent of the valinomycin concentration since a positive dependence would indicate protonophoric activity. As

valinomycin is poorly soluble in water, we added it to liposome solutions via concentrated aliquots in DMSO; the resulting plot of $P_{H+/OH-}$ *versus* valinomycin concentration is shown in Fig. 3.3. We chose DMSO as a solvent rather than ethanol (used in Paula *et al.*[20]) because DMSO has a smaller effect on $P_{H+/OH-}$ (Fig. 3.3, leftmost data points). The $H^+/OH^-$ permeability increased from the baseline value following the addition of just 10 fM valinomycin and plateaued with increasing valinomycin concentrations until a point of inflection was reached around 100 nM, at which point $P_{H+/OH-}$ began to increase dramatically in the presence of more valinomycin. We selected a valinomycin concentration of 10 nM for all subsequent experiments.

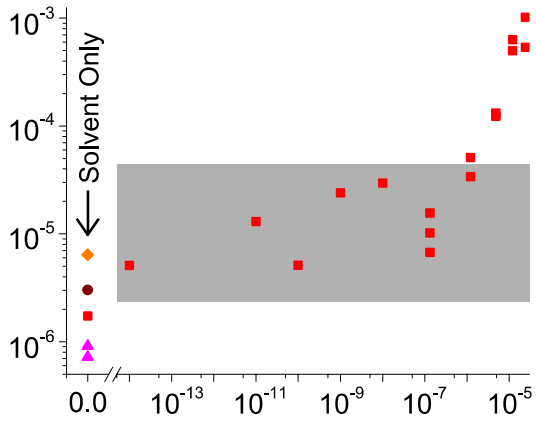


**Figure 3.3**. Valinomycin concentrations up to $10^{-7}$ M prevent membrane potential buildup without causing an increase in $P_{H+/OH-}$. Before the axis break, points represent $P_{H+/OH-}$ after the addition of the solvent vehicle only as indicated by the symbols: red squares – 2.66 µL DMSO, brown circle – 1.33 µL ethanol, orange diamond – 2.66 µL ethanol, pink triangles – no solvent. After axis break, the final concentration of valinomycin indicated on the x-axis was added in 2.66 µL DMSO to a total volume of 1 mL. Red squares within the area shaded in grey represent data within the "plateau" range of valinomycin concentrations. All experiments were run on POPC vesicles extruded through 80 nm filters.

**Table 3.1.** Comparison of various parameters of self-assembled membranes formed by lipids examined in this work.

| Lipid | Thickness (nm) (± SEM) | | Area per lipid ($Å^2$)[a] (± SEM) | Variance in area per lipid ($Å^2$)[a] (± SEM) | $D_1$ ($\times 10^{-11}$ $m^2/s$)[a] (± SEM) | $D_2$ ($\times 10^{-11}$ $m^2/s$)[a] (± SEM) | $D_L$ ($\times 10^{-13}$ $m^2/s$) (± SEM) | Entropy (J $mol^{-1}$ $K^{-1}$)[a] (± SEM) | Bending rigidity (pN nm)[a] | $P_{H+/OH-}$ ($\times 10^{-6}$ cm/s) (95% CI) |
|---|---|---|---|---|---|---|---|---|---|---|
| | MD | AFM | | | | | | | | |
| T28 | 3.78 ± 0.01 | 4.4 ± 0.01 | 63.7 ± 0.02 | 0.047 ± 0.005 | 2.03 ± 0.10 | 0.13 ± 0.004 | 0.6 ± 0.2 | 5080 ± 22 | 5470 | 6.2 (1.3 – 11.0) |
| T32 | 4.01 ± 0.01 | n.d. | 63.1 ± 0.01 | 0.360 ± 0.004 | 2.22 ± 0.17 | 0.16 ± 0.004 | 0.6 ± 0.1 | 5276 ± 20 | 3960 | 11.8 (3.6 – 20.0) |
| T36 | 4.11 ± 0.02 | 4.6 ± 0.01 | 64.4 ± 0.02 | 0.063 ± 0.006 | 1.88 ± 0.09 | 0.12 ± 0.004 | 0.5 ± 0.2 | 5481 ± 20 | 4510 | 26.3 (8.8 – 43.9) |
| U16 | 3.81 ± 0.02 | n.d. | 69.0 ± 0.02 | 0.090 ± 0.009 | 2.99 ± 0.14 | 0.42 ± 0.003 | 9.4 ± 1.1 | 5565 ± 17[b] | 4060 | 7.7 (3.8 – 11.7) |
| Di-O-PhyPC | n.d. | n.d. | n.d. | n.d. | n.d. | n.d. | 2.9 ± 0.5 | n.d. | n.d. | 4.0 (-1.8 – 9.7) |
| DiPhyPC | 3.78 ± 0.03 | Lit: 5.3[50] | 78.6 ± 0.06 Lit: 80.6[51] | 0.193 ± 0.039 | 2.45 ± 0.10 | 0.21 ± 0.004 | 5.7 ± 0.5 | 5459 ± 18[b] | 4470 | 2.8 (0.5 – 5.1) |
| POPC | 3.96 ± 0.02 | Lit: 4.6[52] | 64.2 ± 0.03 Lit: 64.3[51] | 0.213 ± 0.021 | 4.65 ± 0.14 | 0.65 ± 0.002 | 12.0 ± 1.5 | 5531 ± 14[b] | 2670 | 10.6 (4.5 – 16.8) |

[a] Unless otherwise indicated, these values were obtained from MD simulations.

[b] The entropy values of untethered lipids U16, DiPhyPC, and POPC were multiplied by two for comparison to the tethered lipids.

*Systematic variation of a series of Archaea-inspired lipids*

We explored the effect of transmembrane tethering, tether length, and the presence of isoprenoid methyl groups on one or both lipid tails on the $P_{H+/OH-}$ values through liposomes formed from a series of synthetic lipids with small systematic structural variations. T28, T32, and T36 have an unbranched, saturated alkyl tether linked via ether bonds to two glycerophosphocholine head groups that each have one phytanyl tail of 16 carbons (Fig. 3.1 A-C). The lipid U16 (Fig. 3.1 D) is untethered and has a 16-carbon straight chain attached to the head group in place of the tether; it is structurally equivalent to half of T32. The commercially-available lipid Di-O-PhyPC (Fig. 3.1 E) differs from U16 only insofar as it has two phytanyl chains instead of one phytanyl and one n-alkane acyl chain. DiPhyPC (Fig. 3.1 F) is identical to Di-O-PhyPC except that the phytanyl chains are attached to the head groups with ester rather than ether linkages. Fig. 3.4 compares $H^+/OH^-$ permeability values for tethered and untethered archaea-inspired lipids alongside those gathered for POPC (Fig. 3.1 G).

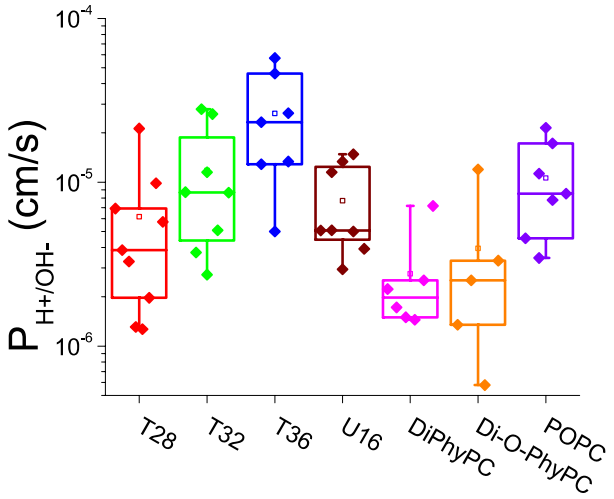


**Figure 3.4**. Box-and-whisker plots showing $P_{H+/OH-}$ values gathered from seven different lipids. Whiskers extend to minimum and maximum values, box covers interquartile range, center line represents median, hollow square represents mean.

*$H^+/OH^-$ permeability of tethered lipids increases with tether length*

The $P_{H+/OH-}$ permeability results from the lipids T28, T32, and T36 indicate that liposome membranes become more permeable to protons as tether length increases if the length of the untethered acyl chain is kept constant (Table 3.1). A Tukey Honest Significant Difference (HSD) test comparing the log-transformed $P_{H+/OH-}$ values of these three lipids found the mean $H^+/OH^-$ permeability of LUVs composed of T28 lipids to be significantly smaller ($p = 0.01$) than that of T36 LUVs. Like prior researchers,[20] we used log-transformed values for all statistical comparisons because the populations of measured $P_{H+/OH-}$ values failed tests of homogeneity of variance (Levene's $p = 0.002$, Brown-Forsythe $p = 0.02$) unless the values were log-transformed (Levene's $p = 0.72$, Brown-Forsythe $p = 0.75$).

*Results from molecular dynamics simulations*

In an attempt to gain insight into the molecular differences that may affect proton permeability through membranes, we conducted molecular dynamics (MD) simulations of membranes composed of each lipid (except Di-O-PhyPC) in order to measure structural parameters such as membrane thickness, area per lipid, lateral diffusion coefficients, conformational entropy, and bending rigidity. Table 3.1 shows the results from MD simulations for these lipids; they agree well with experimentally measured values. For instance, the lateral diffusion coefficients $D_2$ determined by MD simulations were strongly correlated with lateral diffusion coefficients ($D_L$) measured by fluorescence recovery after photobleaching (FRAP) experiments on supported lipid bilayers of the same six lipids (Table 3.1, Pearson correlation coefficient $r = 0.95$ with $p = 0.004$). Additionally, the thicknesses of T28 and T32 membranes as measured by AFM were 0.5 to 0.6 nm larger than those determined by MD, which falls within

the literature range for the thickness of the expected water layer between lipids and the underlying Mica substrate used for AFM measurements (0.4 - 1.7 nm) (Fig. 3.5).[53,54] Previous studies that compared bilayer thickness defined by AFM for POPC and DiPhyPC with the MD data also reported water layer thicknesses in this range (Table 3.1).[50,52] Further, the area per lipid values obtained from MD for POPC and DiPhyPC are within 3% of literature values obtained by Kučerka *et al.* from small-angle X-ray and neutron scattering.[51]

The experimentally measured $H^+/OH^-$ permeability in monolayers of tethered lipids increased with increasing tether length (T28, T32 and T36). The results from MD simulations in Table 3.1 reveal that membrane stiffness decreases and lipid entropy increases with increasing lipid tether length, as well. Shinoda *et al*. and Haines each propose that crowding in the hydrocarbon core of membranes reduces proton leakage.[55,56] In the tethered lipids, the two untethered phytanyl chains have a combined length of 32 methylene groups – four carbons longer than the T28 tether and four carbons shorter than the T36 tether; the differences in $P_{H+/OH-}$ may be attributable to increased hydrocarbon crowding in T28 and the presence of a "gap" in T36. Therefore, the observed reduction in proton permeability in the sequence of membranes from T36 lipids to T32 lipids and T28 lipids could be a result of the increasing crowding, order, and stiffness of the hydrophobic region of the membranes.

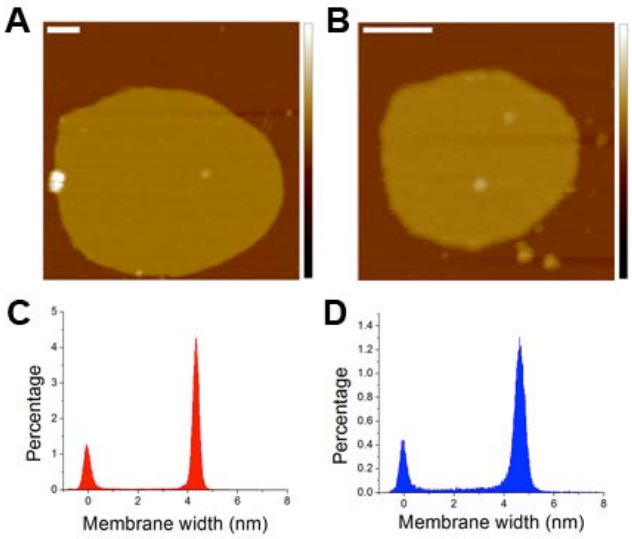


**Figure 3.5.** Atomic force microscopy (AFM) measurements of the thickness of supported lipid membranes comprised of T28 and T36 lipids on a mica surface. **A**. AFM image of a T28 membrane on a mica surface. The dark areas reflect the underlying mica surface, whereas the light areas represent a patch of lipid membrane. **B**. AFM image of a T36 membrane on a mica surface. **C**. Histogram showing the distribution of z-height measurements from the AFM images of T28 lipid membranes. Minimum peak = 0.0 ± 0.3 nm (SD); maximum peak = 4.4 ± 0.3 nm. **D**. Histogram showing the distribution of z-height measurements from the AFM images of T36 lipid membranes. Minimum peak = 0.0 ± 0.3 nm; maximum peak = 4.6 ± 0.4 nm. The minimum peak represents the height of the mica surface, which was set to zero. The errors in the z-height measurements represent full width at half maximum of each histogram peak. The vertical color-coded scale is 15 nm. Scale bars = 100 nm.

MD simulations also reveal that despite the hydrophobic nature of the membrane core, water molecules regularly enter this region as previously found in the literature[57–62] (see Fig. 3.6). Defining a penetration event as an instance when a water molecule moves past the ether or ester oxygen of the nearest lipid into the hydrophobic region, we found penetration frequencies of 8 x $10^{-3}$ to 1.6 x $10^{-2}$ $nm^{-2}$ $ns^{-1}$. These values are similar to the water penetration frequencies reported by Krylov *et al*. from MD simulations of DOPS, DPPC, and DOPC membranes, which ranged from 3.5 x $10^{-3}$ to 4.3 x $10^{-2}$ $nm^{-2}$ $ns^{-1}$.[62] (We note that this discussion is limited to the penetration of water molecules into the hydrophobic region of the membrane rather than water permeation all the way through the bilayer.) The number of water molecules is consistent with a Poisson process, implying that the entry of a given water molecule is independent from other

water molecules. Quantifying the entry of water molecules into the hydrophobic core in all six simulated membranes (including three untethered lipids, Table 3.2) revealed that log $P_{H+/OH-}$ correlated with the total number of water molecules that spontaneously entered the membrane over 50 ns (Pearson coefficient $r = 0.86$, $p = 0.027$). A better correlation was found between log $P_{H+/OH-}$ and the number of observations with at least three water molecules residing anywhere in the hydrophobic core of the membrane (Pearson coefficient $r = 0.99$, $p = 0.0003$, Fig. 3.7 A).

**Table 3.2.** Observation of water molecules in the hydrophobic core of lipid membranes as determined by molecular dynamics simulations over 50 ns.

| Lipid | Total number of water molecules observed in membrane | Mean number of water molecules per snapshot ± SE | Number of observations with at least three water molecules anywhere in the membrane | Number of clusters with two or more water molecules |
|---|---|---|---|---|
| T28 | 307 | 0.614 ± 0.035 | 16 | 17 |
| T32 | 349 | 0.698 ± 0.037 | 25 | 26 |
| T36 | 374 | 0.748 ± 0.039 | 31 | 29 |
| U16 | 346 | 0.692 ± 0.037 | 20 | 20 |
| DiPhyPC | 230 | 0.460 ± 0.030 | 6 | 18 |
| POPC | 391 | 0.782 ± 0.040 | 24 | 26 |

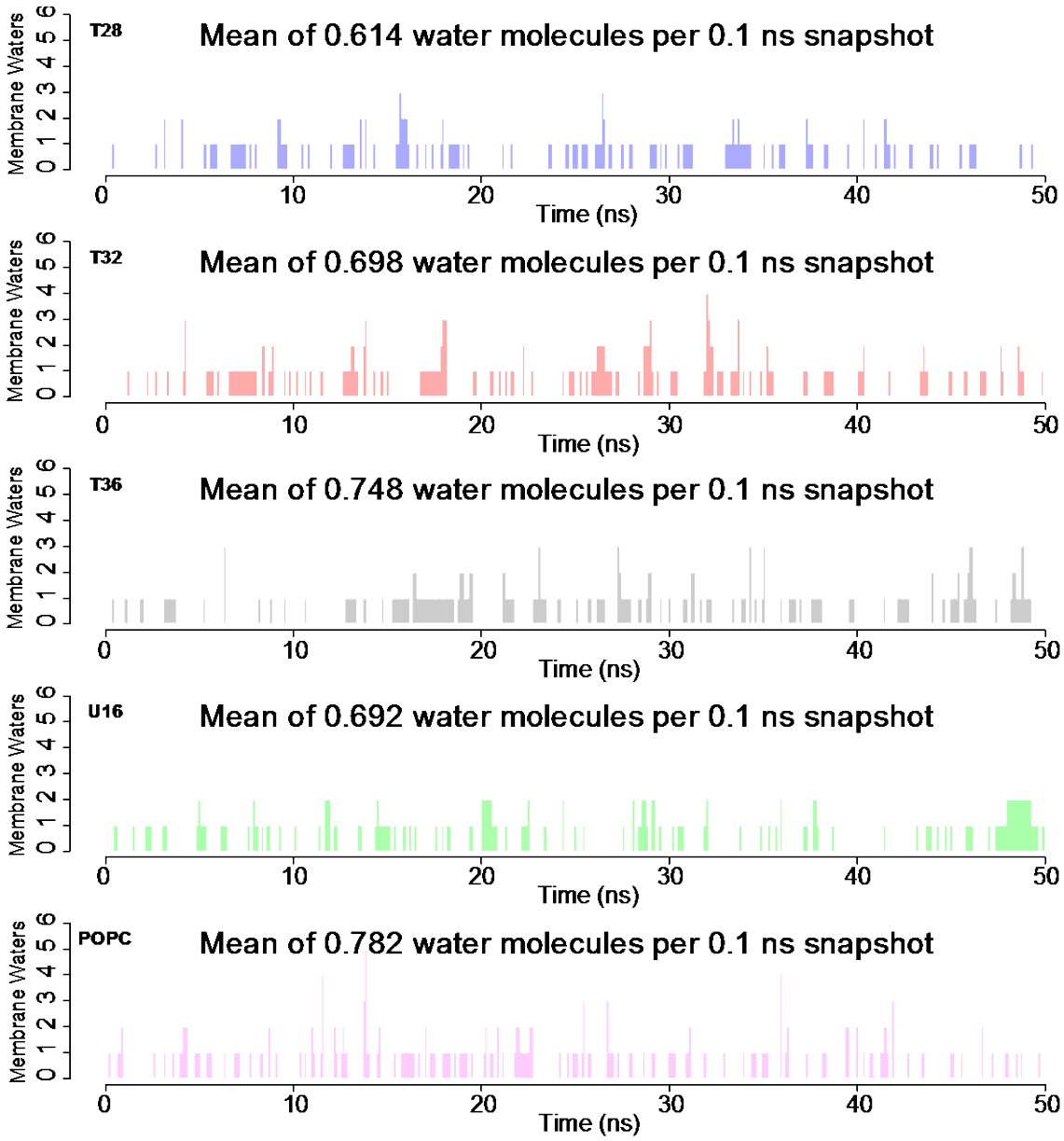


**Figure 3.6.** The number of water molecules in the hydrophobic core of the membrane during 50 ns of MD simulation. Only waters that penetrated beyond the ester/ether oxygens were counted, and statistical analysis showed that water entry was consistent with a Poisson process.

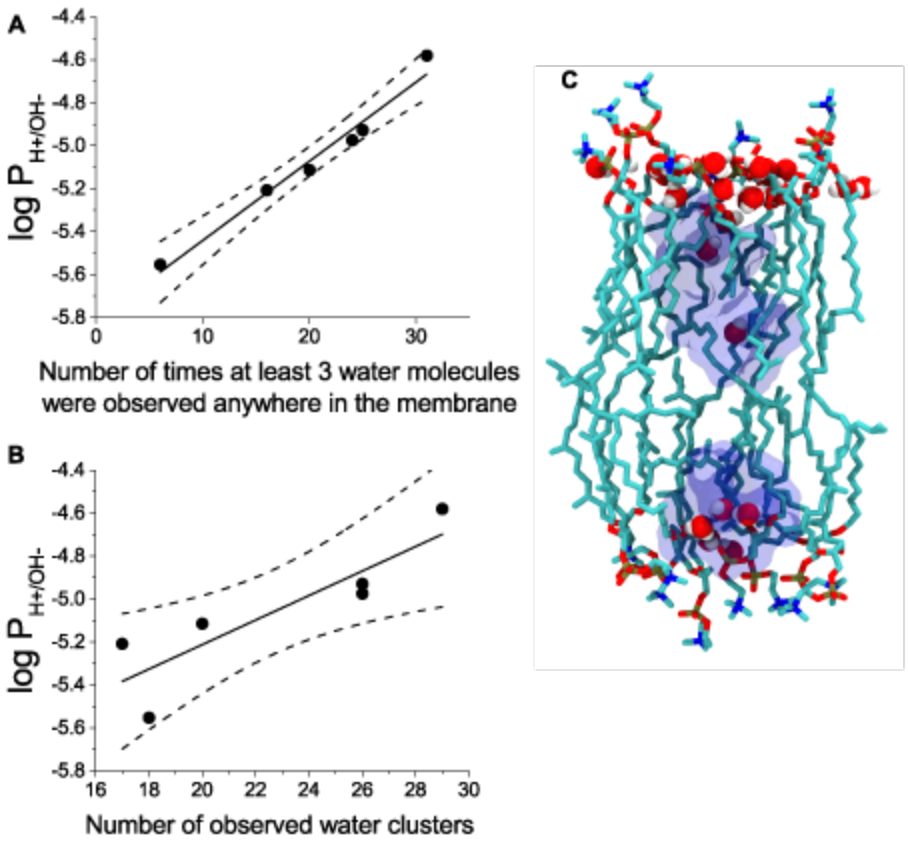


**Figure 3.7.** Water within the hydrophobic region is predictive of log $P_{H+/OH-}$. **a)** Correlation plot of log $P_{H+/OH-}$ as a function of the number of times at least three water molecules simultaneously occupied the hydrophobic region anywhere in the lipid membrane over the course of a 50 ns MD simulation. Pearson coefficient $r$ = 0.99. Solid line is the best fit to a straight line; dotted lines show the 95% confidence interval from the fit. **b)** Correlation plot of log $P_{H+/OH-}$ as a function of the number of times a water cluster appeared in the hydrophobic region of the lipid membrane over the course of a 50 ns MD simulation. Pearson coefficient $r$ = 0.88. **c)** A snapshot from the MD simulation of a membrane from T28 lipids showing the penetration of water molecules into the hydrophobic core of the membrane. Water molecules are shown as van der Waals spheres and the solvent accessible surface area around the waters in the membrane core is shown in blue.

Although we would not expect the distribution of water molecules to be uniform throughout the volume of the hydrophobic core of the lipid membrane (the probability should fall off with increasing distance from the head group into the core[62]), it should be roughly uniform across the surface area of the membrane. Thus, the probability of finding two water molecules in the vicinity of the same lipid head group would be inversely proportional to the number of head groups, which for all of our simulated membranes would be 1/1458 or approximately 0.07%. If

we take the T28 membrane as an example, we find 59 instances of 2 or more water molecules anywhere in the membrane in our simulations (data taken at 0.1 ns intervals over 50 ns, i.e. 500 observations); this value approximates the expected value of 63.3 from the corresponding best-fit Poisson distribution. Interestingly, in 17 of these 59 instances, water molecules were located within 5 Å of each other; we define this condition as a water cluster. This observed clustering probability of 28% is well above the expected 0.07%, leading us to conclude that although water molecules appear to enter the hydrophobic core independently, they have a strong tendency to cluster after entry. As shown in Fig. 3.7 B, the number of observed water clusters also correlates well (Pearson coefficient $r$ = 0.88, $p$ = 0.022) with the measured proton permeability; this observation is consistent with prior observations in the literature.[19,41,56,63]

Indeed, the formation of water chains or clusters is thought to be a primary mechanism for proton shuttling across the membrane,[55] and although our simulations were not long enough to capture water chains that span the entire membrane thickness, we do see the formation of nascent clusters with multiple water molecules (Fig. 3.7 C). Previous MD simulations made similar observations and ultimately concluded that the clustering of water molecules is relevant for the permeation of protons but not water and that the presence of phytanyl groups would serve to disrupt water clusters and decrease proton permeability.[56] Experimental studies using FTIR spectrometry similarly found that the formation of water clusters within the membrane had a strong dependence on the acyl chain composition.[64] Taken together, these results support the idea that water entry and clustering in the hydrophobic core are both relevant metrics for proton permeation. We caution, however, that while the likelihood that this correlation was a result of random chance is very low, this relationship will have to be tested with additional lipids, given the large uncertainty in the measured proton permeabilities and the limited number of six data

pairs in the correlation analysis. We are currently trying to expand the number of tested lipids, however, the synthesis of archaea-inspired lipids is extremely work intensive and MD simulations are time intensive, requiring a separate follow-up study.

*Tethered and untethered lipids are equally $H^+/OH^-$ permeable at room temperature*

Interestingly, tethering itself did not seem to affect $H^+/OH^-$ permeability in our measurements. To observe the effects of tethering, we compared $P_{H+/OH-}$ values from membranes composed of U16 and T32, since T32's structure is identical to two U16 lipids bonded together at the terminal carbons of their unbranched chains (Fig. 3.1 B, D). A two-tailed Student's *t*-test comparing the log-transformed permeability values of T32 LUVs and U16 LUVs (Table 3.1) showed that they were not significantly different ($p = 0.46$); the spread of the U16 $P_{H+/OH-}$ values fell entirely within the spread of the T32 $P_{H+/OH-}$ values. It is, however, worth noting that we conducted all our experiments at room temperature. Komatsu and Chong found that the $H^+/OH^-$ permeability of doubly-tethered lipids isolated from *S. acidocaldarius* was relatively invariant with respect to temperature from 25-80 ºC, whereas $P_{H+/OH-}$ values from standard (untethered) eggPC lipids increased dramatically with increasing temperature. The $P_{H+/OH-}$ values from the two membrane compositions were comparable at room temperature but diverged greatly at higher temperatures.[65]

*Isoprenoid methyls decrease $H^+/OH^-$ permeability*

Based on a two-tailed Student's *t*-test comparing log-transformed $P_{H+/OH-}$ values, the mean permeability of liposomes from Di-O-PhyPC lipids was lower ($p = 0.059$) than from U16 lipids (Table 3.1). Given that U16 and Di-O-PhyPC only differ structurally by the presence or

absence of isoprenoid methyl groups on one lipid tail, this result agrees with previous findings that this motif lowers $H^+/OH^-$ permeability.[9] Most lipids characteristic of acidophilic archaea display the isoprenoid methyl motif on both acyl chains.[2]

*Possible reasons for variability in measured $P_{H+/OH-}$ values*

Despite strong efforts to optimize the permeability assay, we were unable to eliminate variability between measured $H^+/OH^-$ permeability values of membranes composed of the same lipid. This variability, seen both in this work and in prior literature,[9,17,22,26,39,43,66,67] represents a limitation of the usefulness of $P_{H+/OH-}$ data.[25,27] We have attempted to identify and minimize potential sources of variation inherent in the process of gathering $P_{H+/OH-}$ values and present a detailed discussion on this topic in the Appendix, section S3.1.

### 3.5 Conclusions

We have optimized a fluorescence-based $H^+/OH^-$ permeability assay by introducing a fitting formula that describes the entire kinetics of a step ΔpH-induced change of the interior pH of liposomes and by establishing an appropriate concentration of valinomycin (10 nM) in order to investigate permeability values in homogeneous lipid membranes containing synthetic archaea-inspired lipids. The lipid T32, which was tethered by a straight 32-carbon chain, produced membranes with similar $P_{H+/OH-}$ values to those of membranes composed of its untethered equivalent U16, revealing that tethering does not affect $P_{H+/OH-}$ at room temperature. However, $P_{H+/OH-}$ values among tethered lipid membranes increased with increasing tether length if the number of carbons in the untethered acyl tail was constant. Further, monopolar lipids with two tails containing isoprenoid methyl branches form membranes with lower $H^+/OH^-$

permeability than those with one branching tail and one unbranched tail. These results inform the design of synthetic bipolar lipid molecules for desired $H^+/OH^-$ permeability characteristics.

### 3.6 Contributions of Others

Geoffray Leriche and Takaoki Koyanagi from the Yang group at the University of California San Diego synthesized and characterized the lipids used in this work; synthesis procedures and spectra can be found in Sections 4 and 5 of the Supporting Material of Schroeder *et al*. 2016.[1] Mitchell Johnson, Kathryn Haengel, and Claire Wang assisted me in permeability experiments. Olivia Eggenberger performed measurements of the lateral diffusion coefficient using FRAP shown in Table 3.1. Young Hun Kim performed atomic force microscopy shown in Figure 3.5. Karthik Diraviyam and David Sept designed and performed the molecular dynamics experiments. The spectrofluorometer used here belonged to the laboratory of Mary-Ann Mycek. This project was conceived by Michael Mayer, Jerry Yang, David Sept, and myself.

## Chapter 3 Appendix

### S3.1. Possible reasons for variability in measured $P_{H+/OH-}$ values

Despite strong efforts to optimize the permeability assay, we were unable to eliminate variability between measured $H^+/OH^-$ permeability values of membranes composed of the same lipid. This variability, seen both in this work and in prior literature,[9,17,26,39,43,66–68] represents a limitation of the usefulness of $P_{H+/OH-}$ data.[25,27] We have attempted to identify and minimize potential sources of variation inherent in the process of gathering $P_{H+/OH-}$ values.

First, as noted in the Materials and Methods section, we made an effort to ensure that the vast majority of the liposomes in solution were unilamellar. Before extrusion, the liposome solutions contained visible lipid aggregates (likely remnants of the lipid film) that would make it difficult to obtain reliable particle size data from DLS. We therefore performed a preliminary extrusion of seven passes through a polycarbonate membrane with significantly larger pores (usually 200 nm) than the desired liposome size (usually 80 nm) and measured the size distribution using DLS. The smallest diameters seen in these distributions were usually larger than 100 nm, so in order to ensure that all liposomes in the solution had been forced through pores smaller than their diameter (and thereby to increase the likelihood of producing unilamellar liposomes), we extruded them through membranes with 80 nm pores for 21 passes. This measure was taken to reduce, as much as possible, the fraction of multilamellar vesicles (MLVs) formed during lipid film hydration remained in the final liposome solution[28,69] since such MLVs would lead to an erroneous apparent reduction of $P_{H+/OH-}$ values.

We suspect that variation inherent in the extrusion procedure might account for some of the variation in $P_{H+/OH-}$, as the mode of the diameter distributions of LUVs of identical composition that had undergone final extrusion through polycarbonate membranes with 80 nm

pores varied from 52 nm to 78 nm. Unlike lipid bilayers, monolayers of bipolar lipids must maintain a 1:1 ratio of lipid head groups between the interior and exterior of the membrane, assuming that all lipids orient themselves in a transmembrane configuration.[70,71] In curved membrane systems such as liposomes, there will, however, exist a disparity in the membrane area per head group between the interior and exterior faces of the membrane. We wondered whether tethered lipid membranes with different curvatures would have significantly different $H^+/OH^-$ permeability values due to corresponding differences in the magnitude of this disparity in inner and outer surface area. To investigate possible effects of the diameter of unilamellar liposomes on $H^+/OH^-$ permeability values, we collected $P_{H+/OH-}$ values for each of the synthetic lipids after final extrusion through membranes with 200 nm pores for comparison to the 80 nm values (Fig. S3.1). For these experiments, we performed a first extrusion through membranes with 400 nm pores. The distributions of measured $P_{H+/OH-}$ values from liposomes extruded through 200 nm filters overlapped the $P_{H+/OH-}$ value distributions of liposomes extruded through 80 nm. We thus concluded that variations in diameter could not account for the variation seen in this study and included the 200 nm values in Fig. 3.4. A related possibility is that the liposome sizing procedure using DLS yields unreliable diameter values; as $P_{H+/OH-}$ is directly proportional to $r$ in the fitting formula (Eq. (2)), any error in liposome size measurement will be translated directly to error in $P_{H+/OH-}$.

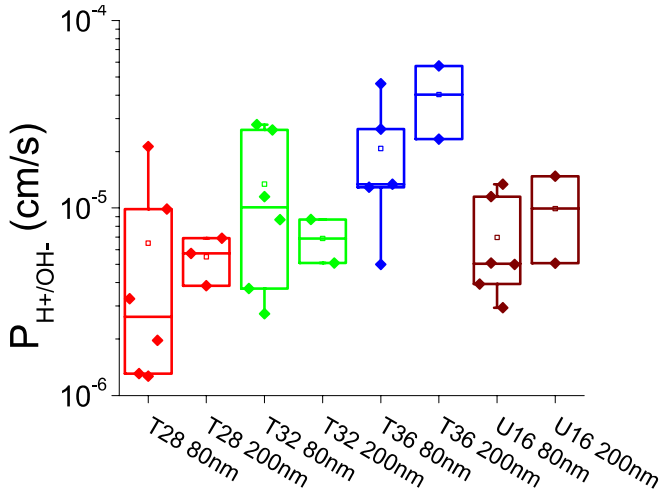


**Figure S3.1.** The $P_{H+/OH-}$ values from liposomes extruded through 200 nm filters generally overlap the $P_{H+/OH-}$ distributions from liposomes extruded through 80 nm filters. A Tukey HSD test and two-tailed Student's *t*-tests showed no statistical significance between liposome sizes for any lipid.

We then wondered whether incorporating the entire liposome size distribution as determined by DLS rather than the most probable liposome size would minimize the spread of our data. We designed a fitting equation that takes in the full size distribution of the liposomes as a histogram (provided by the DLS instrument). In other words, consideration of a size distribution with weights and sizes as shown in Figure S3.2 A is implemented by changing the equation

$$\frac{I_{ex450}}{I_{ex415}} = A_2\left(\frac{\left[H^+\right]_{f,o} - y_1}{A_1 - Ce\dfrac{3P_{H^+/OH^-}\left(y_1 - \left[H^+\right]_{f,o}\right)}{rx_1}}\right)^{-x_1/x_2} + y_2 \quad \text{to} \quad \frac{I_{ex450}}{I_{ex415}} = y_2 + A_2\sum_i^{bins} W_i\left(\frac{\left[H^+\right]_{f,o} - y_1}{A_1 - Ce\dfrac{3P_{H^+/OH^-}\left(y_1 - \left[H^+\right]_{f,o}\right)}{r_i x_1}}\right)^{-x_1/x_2}.$$

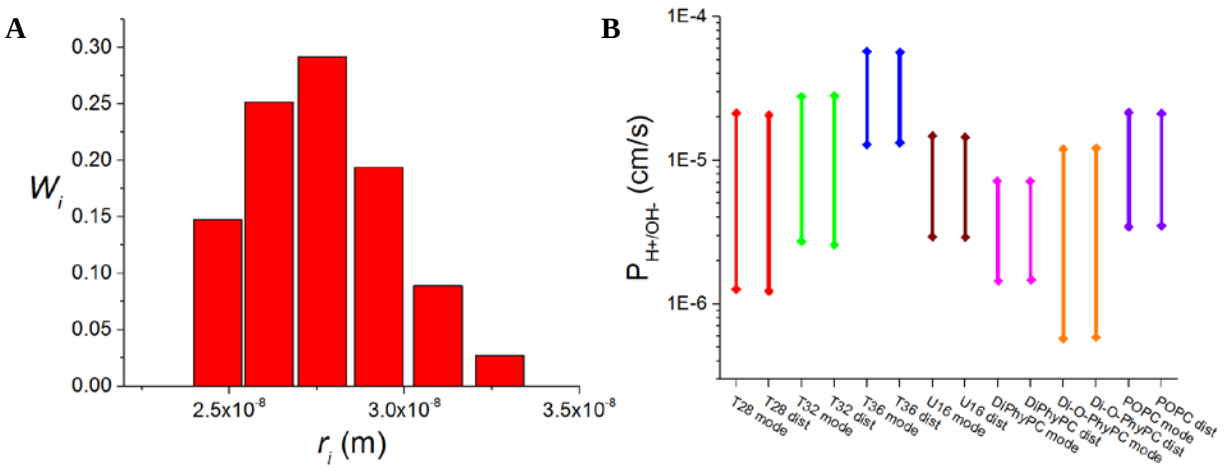


**Figure S3.2.** Including full vesicle radius distributions in the fitting formula does not substantially impact the $P_{H+/OH-}$ values. **A.** Typical distribution of vesicle radii as determined by DLS. **B.** Highest and lowest $P_{H+/OH-}$ values for each lipid calculated using the mode of each size distribution ("mode") and using the full distribution ("dist").

In order to determine whether accounting for variability in the liposomes' size distributions would result in narrower distributions of $P_{H+/OH-}$ values compared to calculations based on the most probable liposome size in the distribution, we fit, for each lipid, the fluorescence decay traces that gave the highest and lowest $P_{H+/OH-}$ with the new *r*-distribution-inclusive fitting formula using the DLS data from that experiment. The results are shown in Figure S3.2 B. The highest and lowest $P_{H+/OH-}$ values for each lipid as determined using the most probable vesicle radius are plotted next to the values as determined using the entire vesicle radius distribution. The two methods produce nearly indistinguishable $P_{H+/OH-}$ spreads. Compared to using the most probable vesicle radius, this new fitting procedure changed the $P_{H+/OH-}$ values by less than 2% on average with no systematic directionality. Therefore, we conclude that the large spread in $P_{H+/OH-}$ does not appear to be the result of vesicle size distributions.

Additionally, the liposome solution comes into contact with a number of different surfaces before and during each fluorescence decay experiment, including the glass round-bottom flask where the lipid film is hydrated, multiple plastic microvials, cuvettes for DLS and spectrofluorometry, plastic pipette tips, and a metal pH meter tip. Possible interactions between

these surfaces and the lipid membranes, as well as possible effects on the integrity of the liposomes, have not been accounted for in this work; differences in the time of exposure to each surface as well as in the time between liposome preparation and performance of the assay may also be partly responsible for the uncertainty in measured $P_{H^+/OH^-}$ values.

Another potential source of error relates to a slow upward trend of the fluorescence ratio observed on some occasions when the liposome solutions were observed over time scales of thousands of seconds before the addition of acid. Such an upward drift in fluorescence ratio has been reported previously by Grzesiek and Dencher.[38] One possible explanation may be intensity drift associated with the instrument's light source, although we always turned it on at least 30 min prior to use. We do *not* think that this upward trend was the result of slow leakage of pyranine dye from the vesicles. Pyranine is classified as a "membrane-impermeant" dye due to its three negative charges and slow leakage kinetics; even if it leaked over the time scale relevant to the experiment, it would likely produce a downward trend in fluorescence ratio: solutions of pyranine exhibit self-quenching at high concentrations – at the excitation and pH range used, the fluorescence emission intensity of pyranine solutions at 510 nm increases with pyranine concentration before it peaks and decreases between 100 μM and 250 μM. We therefore chose an intravesicular dye concentration of 50 μM to remain below this self-quenching range. Even at this relatively low concentration, however, the fluorescence intensity does not increase linearly with respect to concentration, so the leakage of pyranine out of LUVs in the absence of a pH gradient would result in a rising total fluorescence intensity at each wavelength as dye molecules would move from ~ 50 μM concentration to a volume of extremely low pyranine concentration where no detectable self-quenching occurs. Despite the expected increase in fluorescence intensity due to this dye leakage scenario, we found that this increase in fluorescence emission

was less pronounced when using the pH-sensitive excitation wavelength of 450 nm than the fluorescence emission when using the pH-invariant excitation wavelength of 415 nm. Therefore the $I_{450}/I_{415}$ fluorescence emission *ratio* would be expected to *decrease* if significant leakage of fluorescent pyranine would occur.

Another potential source for uncertainty in $P_{H+/OH-}$ data may be related to a tendency of the measured fluorescence ratio traces (such as Fig. 3.2 A) to display higher fluorescence ratio (driven by a higher raw emission intensity at the pH-dependent excitation wavelength) after the addition of the final KOH aliquot during calibration than before the initial acid was added – despite having added an equivalent amount of strong acid and strong base and despite obtaining equivalent pH measurements from the pH meter at each time point. Grzesiek and Dencher also report a similar asymmetric response when comparing titrations of acid and base into DiPhyPC vesicles[38]. We considered a number of possible reasons for this unexpected increase in fluorescence, such as lamp intensity drift and photochemical changes in pyranine's response to pH changes over the long (~2 h) durations of the permeation experiments performed in this study. We ruled out both of these hypotheses experimentally, however. After a period of fluorescence collection to establish a stable baseline, we added the same total amounts of $H_2SO_4$, nigericin, and KOH to POPC liposomes as in a typical $H^+/OH^-$ permeation experiment, but did so on a much shorter timescale than usual, namely ~24 minutes instead of the typical ~2 hours. The fluorescence ratio stayed stable before the addition of the acid, ruling out a photochemistry-induced change to the fluorescence ratio at pH 7.25. After acid, nigericin, and base additions, the fluorescence ratio recovered to approximately 120% of its initial value despite the initial and final pH being nearly identical as reported by a pH meter, an overshoot typical of the (significantly longer) experiments that we performed in this study. We concluded that any

photochemical change in pyranine's response to pH would have to have taken place within the first 24 minutes between the acid addition and the final base addition. In order to rule out photochemical changes on a shorter timescale, we filled two cuvettes with 1 mL intravesicular solution (containing pyranine at pH 7.25) used in our experiment, but in the absence of liposomes. We added 10 µL 250 mM $H_2SO_4$ as usual to one of these cuvettes and recorded the fluorescence ratio for 2 h, after which point we added 10 µL 500 mM KOH. Both the recorded pH and the fluorescence ratio were the same in the end as the control cuvette, leading us to conclude that our anomaly's cause is not photochemical in nature and must have to do with the presence of liposomes in the experimental system, as observed by Grzesiek and Dencher.[38]

Despite our best efforts, we could not find an explanation that could account for this effect. Nonetheless, the overshoot was observed in all measurements to a similar extent (the final fluorescence ratio exceeds the initial ratio by approximately 20% at the same measured pH) regardless of vesicle size or lipid composition. We therefore believe that while this artifact likely causes a slight systematic error in all measured $P_{H+/OH-}$ values, it does not affect the values' relative standing, as it was consistently observed. The main purpose of this work is the comparison of $P_{H+/OH-}$ within a family of structurally similar lipids.

Ultimately, despite the careful optimization of the $P_{H+/OH-}$ assay presented here, we observed significant uncertainty in the measured values, which is consistent with published results and may, to some extent, be inherent to the particular problem of measuring proton permeability through lipid membranes as discussed in previous work.[9,23,25,26,38] While reflecting on this, we consulted a number of literature sources of $P_{H+/OH-}$ data. In these works we found evidence that the distributions of $P_{H+/OH-}$ values we measured for each lipid are not wider than typically found in prior reports, rather the presentation of the data is different.

In the literature, $P_{H+/OH-}$ values are either presented graphically on a plot or numerically as values in a table or in the text of an article. In both instances, the norm has been to present the values as a mean plus or minus the standard error of the mean (SEM), written explicitly or represented with error bars in a graph. Two good examples of the ways in which $P_{H+/OH-}$ data is commonly presented are Gensure *et al.* 2006, Figs. 2 C and D[23] and Komatsu and Chong 1998, Figs. 6 and 7.[65]

For comparison, the data from the manuscript here is shown in Figure S3.3. In Figs. S3.3 A and B, we present our data similarly to the literature graphs – as a bar or point graph showing a mean and standard deviation on a linear scale. In our opinion, the figures from Gensure *et al.*[23] and Fig. S3.3 A look similar in terms of perceived spread, as do the figures from Komatsu and Chong[65] and Fig. S3.3 B. The presentation style used in the manuscript here (Fig. S3.3 C) shows each data point gathered, uses a logarithmic scale, and is less flattering than Figs. S3.3 A and B. However, we believe that by representing each point of $P_{H+/OH-}$ data, we offer a degree of transparency about our spread that will be useful to future researchers. Additionally, we suggest that permeability data is better presented on a logarithmic scale, as is sometimes done in the literature[20,72] – the quantity will be compared across multiple orders of magnitude, and as mentioned in the main text, distributions of $P_{H+/OH-}$ values fail homogeneity of variance tests while distributions of $P_{H+/OH-}$ pass them. It follows, then, that more permeable membranes will appear to have wider data spreads when viewed on a linear scale; this is particularly visible in the Gensure *et al* Fig. 2 D[23] and Komatsu and Chong Fig. 6.[65] The reverse is also true: the error bars on the small values in these plots are very narrow – a reflection of the magnitude of the mean rather than of the precision of the data.

Often, papers that report proton/hydroxide permeability values numerically do not provide an indication of the uncertainty in their values.[20,24,38] The ones that do usually provide the SEM, but often do not provide the number of experiments that were conducted to obtain the values presented.[9,26,39,43,66–68] We think that the SEM is an imperfect parameter for comparison of spread (standard deviation would be more appropriate if the measured distribution is Normal), but as it is generally the only quantity presented alongside the mean, we have compiled the lipid membrane $P_{H+/OH-}$ values (collected by a variety of assays) that we could find presented numerically with their standard errors in the literature, normalized the standard error values by the means they describe, and presented them in Figure S3.4.[9,17,26,39,43,66–68] The SEM/mean ratios fall between 0.2 and 0.3 on average; our SEM/mean values generally fall within this typical range.

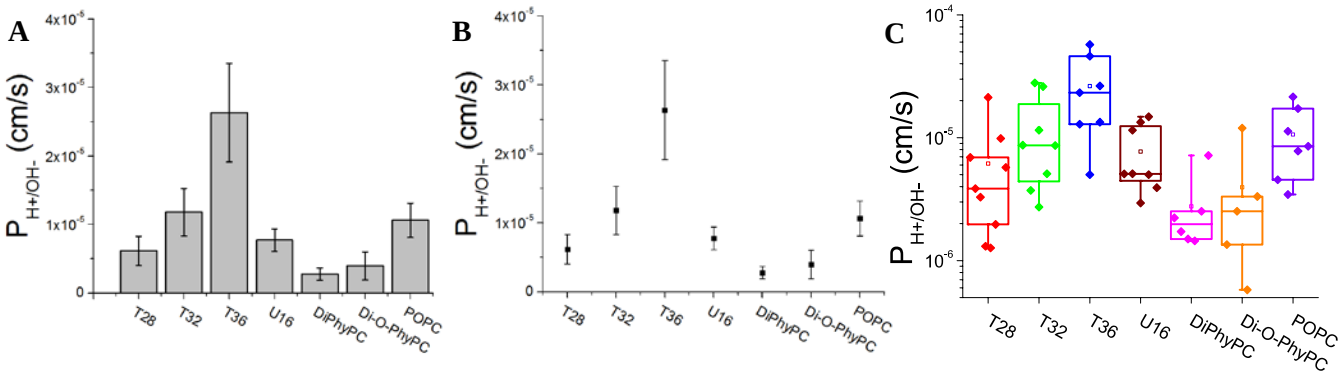


**Figure S3.3.** Plots of $P_{H+/OH-}$ data measured in this study. Represented as in: **A.** Gensure *et al.* 2006,[23] **B.** Komatsu and Chong 1998,[65] **C.** this work.

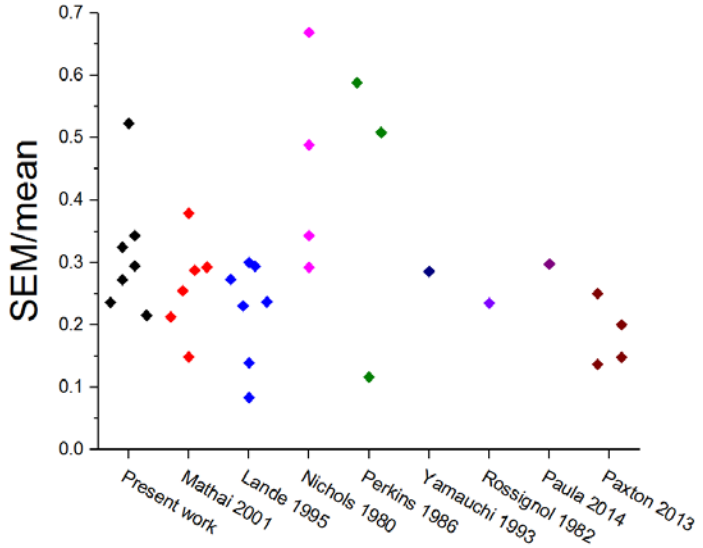


**Figure S3.4.** Standard error of the mean normalized by the mean for $P_{H+/OH-}$ values found in the literature. The leftmost column presents the SEM/mean for the data in this work.

## References


1. Schroeder, T. B. H. *et al.* Effects of Lipid Tethering in Extremophile-Inspired Membranes on H+/OH− Flux at Room Temperature. *Biophys. J.* **110,** 2430–2440 (2016).

2. Ulrih, N. P., Gmajner, D. & Raspor, P. Structural and physicochemical properties of polar lipids from thermophilic archaea. *Appl. Microbiol. Biotechnol.* **84,** 249–60 (2009).

3. Schleper, C. *et al.* Picrophilus gen. nov., fam. nov.: a novel aerobic, heterotrophic, thermoacidophilic genus and family comprising archaea capable of growth around pH 0. *J. Bacteriol.* **177,** 7050–7059 (1995).

4. Konings, W. N., Albers, S.-V., Koning, S. & Driessen, A. J. M. The cell membrane plays a crucial role in survival of bacteria and archaea in extreme environments. *Antonie Van Leeuwenhoek* **81,** 61–72 (2002).

5. Baker-Austin, C. & Dopson, M. Life in acid: pH homeostasis in acidophiles. *Trends Microbiol.* **15,** 165–171 (2007).

6. Michels, M. & Bakker, E. P. Generation of a large, protonophore-sensitive proton motive force and pH difference in the acidophilic bacteria Thermoplasma acidophilum and Bacillus acidocaldarius. *J. Bacteriol.* **161,** 231–237 (1985).

7. Tyson, G. W. *et al.* Community structure and metabolism through reconstruction of microbial genomes from the environment. *Nature* **428,** 37–43 (2004).

8. Elferink, M. G. L., de Wit, J. G., Driessen, A. J. M. & Konings, W. N. Stability and proton-permeability of liposomes composed of archaeal tetraether lipids. *Biochim. Biophys. Acta BBA - Biomembr.* **1193,** 247–254 (1994).

9. Mathai, J. C., Sprott, G. D. & Zeidel, M. L. Molecular Mechanisms of Water and Solute Transport across Archaebacterial Lipid Membranes. *J. Biol. Chem.* **276,** 27266–27271 (2001).

10. De Rosa, M., Gambacorta, A., Nicolaus, B., Chappe, B. & Albrecht, P. Isoprenoid ethers; backbone of complex lipids of the archaebacterium Sulfolobus solfataricus. *Biochim. Biophys. Acta BBA - Lipids Lipid Metab.* **753,** 249–256 (1983).

11. Sprott, G. D., Meloche, M. & Richards, J. C. Proportions of diether, macrocyclic diether, and tetraether lipids in Methanococcus jannaschii grown at different temperatures. *J. Bacteriol.* **173,** 3907–3910 (1991).

12. Lai, D., Springstead, J. R. & Monbouquette, H. G. Effect of growth temperature on ether lipid biochemistry in Archaeoglobus fulgidus. *Extremophiles* **12,** 271–278 (2007).

13. De Rosa, M., Esposito, E., Gambacorta, A., Nicolaus, B. & Bu'Lock, J. D. Effects of temperature on ether lipid composition of Caldariella acidophila. *Phytochemistry* **19,** 827–831 (1980).

14. Uda, I., Sugai, A., Itoh, Y. H. & Itoh, T. Variation in Molecular Species of Core Lipids from the Order *Thermoplasmales* Strains Depends on the Growth Temperature. *J. Oleo Sci.* **53,** 399–404 (2004).

15. de Grotthuss, C. J. T. Memoir on the decomposition of water and of the bodies that it holds in solution by means of galvanic electricity. *Biochim. Biophys. Acta BBA - Bioenerg.* **1757,** 871–875 (2006).

16. Cukierman, S. Et tu, Grotthuss! and other unfinished stories. *Biochim. Biophys. Acta BBA - Bioenerg.* **1757,** 876–885 (2006).

17. Nichols, J. W. & Deamer, D. W. Net Proton-Hydroxyl Permeability of Large Unilamellar Liposomes Measured by an Acid-Base Titration Technique. *Proc. Natl. Acad. Sci. U. S. A.* **77,** 2038–2042 (1980).

18. Nagle, J. F. Theory of passive proton conductance in lipid bilayers. *J. Bioenerg. Biomembr.* **19,** 413–426 (1987).

19. Deamer, D. W. & Nichols, J. W. Proton flux mechanisms in model and biological membranes. *J. Membr. Biol.* **107,** 91–103 (1989).

20. Paula, S., Volkov, A. G., Van Hoek, A. N., Haines, T. H. & Deamer, D. W. Permeation of protons, potassium ions, and small polar molecules through phospholipid bilayers as a function of membrane thickness. *Biophys. J.* **70,** 339–348 (1996).

21. Nichols, J. W. & Abercrombie, R. F. A View of Hydrogen/Hydroxide Flux Across Lipid Membranes - Springer. *J. Membr. Biol.* 21–30 (2010). doi:10.1007/s00232-010-9303-0

22. Lande, M. B., Donovan, J. M. & Zeidel, M. L. The relationship between membrane fluidity and permeabilities to water, solutes, ammonia, and protons. *J. Gen. Physiol.* **106,** 67–84 (1995).

23. Gensure, R. H., Zeidel, M. L. & Hill, W. G. Lipid raft components cholesterol and sphingomyelin increase H+/OH− permeability of phosphatidylcholine membranes. *Biochem. J.* **398,** 485–495 (2006).

24. Deamer, D. W. & Nichols, J. W. Proton-hydroxide permeability of liposomes. *Proc. Natl. Acad. Sci. U. S. A.* **80,** 165–168 (1983).

25. Kuyper, C. L., Kuo, J. S., Mutch, S. A. & Chiu, D. T. Proton Permeation into Single Vesicles Occurs via a Sequential Two-Step Mechanism and Is Heterogeneous. *J. Am. Chem. Soc.* **128,** 3233–3240 (2006).

26. Perkins, W. R. & Cafiso, D. S. An electrical and structural characterization of proton/hydroxide currents in phospholipid vesicles. *Biochemistry (Mosc.)* **25,** 2270–2276 (1986).

27. van de Vossenberg, J. L. C. M., Driessen, A. J. M., da Costa, M. S. & Konings, W. N. Homeostasis of the membrane proton permeability in Bacillus subtilis grown at different temperatures. *Biochim. Biophys. Acta BBA - Biomembr.* **1419,** 97–104 (1999).

28. Hope, M. J., Bally, M. B., Webb, G. & Cullis, P. R. Production of large unilamellar vesicles by a rapid extrusion procedure. Characterization of size distribution, trapped volume and ability to maintain a membrane potential. *Biochim. Biophys. Acta BBA - Biomembr.* **812,** 55–65 (1985).

29. Mingeot-Leclercq, M.-P., Deleu, M., Brasseur, R. & Dufrêne, Y. F. Atomic force microscopy of supported lipid bilayers. *Nat. Protoc.* **3,** 1654–1659 (2008).

30. Lee, J. *et al.* Role of the Fast Kinetics of Pyroglutamate-Modified Amyloid-β Oligomers in Membrane Binding and Membrane Permeability. *Biochemistry (Mosc.)* **53,** 4704–4714 (2014).

31. Richter, R. P. & Brisson, A. R. Following the Formation of Supported Lipid Bilayers on Mica: A Study Combining AFM, QCM-D, and Ellipsometry. *Biophys. J.* **88,** 3422–3433 (2005).

32. Humphrey, W., Dalke, A. & Schulten, K. VMD: visual molecular dynamics. *J. Mol. Graph.* **14,** 33–38, 27–28 (1996).

33. Phillips, J. C. *et al.* Scalable molecular dynamics with NAMD. *J. Comput. Chem.* **26,** 1781–1802 (2005).

34. Watson, M. C., Penev, E. S., Welch, P. M. & Brown, F. L. H. Thermal fluctuations in shape, thickness, and molecular orientation in lipid bilayers. *J. Chem. Phys.* **135,** 244701 (2011).

35. Schlitter, J. Estimation of absolute and relative entropies of macromolecules using the covariance matrix. *Chem. Phys. Lett.* **215,** 617–621 (1993).

36. Wohlert, J. & Edholm, O. Dynamics in atomistic simulations of phospholipid membranes: Nuclear magnetic resonance relaxation rates and lateral diffusion. *J. Chem. Phys.* **125,** 204703 (2006).

37. Benedek, G. B. & Villars, F. M. H. *Physics with Illustrative Examples from Medicine and Biology: Statistical Physics*. (Springer-Verlag, 2000).

38. Grzesiek, S. & Dencher, N. A. Dependency of delta pH-relaxation across vesicular membranes on the buffering power of bulk solutions and lipids. *Biophys. J.* **50,** 265–276 (1986).

39. Rossignol, M., Thomas, P. & Grignon, C. Proton permeability of liposomes from natural phospholipid mixtures. *Biochim. Biophys. Acta BBA - Biomembr.* **684,** 195–199 (1982).

40. Clement, N. R. & Gould, J. M. Pyranine (8-hydroxy-1,3,6-pyrenetrisulfonate) as a probe of internal aqueous hydrogen ion concentration in phospholipid vesicles. *Biochemistry (Mosc.)* **20,** 1534–1538 (1981).

41. Ira & Krishnamoorthy, G. Probing the Link between Proton Transport and Water Content in Lipid Membranes. *J. Phys. Chem. B* **105,** 1484–1488 (2001).

42. Gutknecht, J. Proton/hydroxide conductance and permeability through phospholipid bilayer membranes. *Proc. Natl. Acad. Sci. U. S. A.* **84,** 6443–6446 (1987).

43. Yamauchi, K., Doi, K., Yoshida, Y. & Kinoshita, M. Archaebacterial lipids: highly proton-impermeable membranes from 1,2-diphytanyl-sn-glycero-3-phosphocoline. *Biochim. Biophys. Acta BBA - Biomembr.* **1146,** 178–182 (1993).

44. Brookes, P. S., Rolfe, D. F. S. & Brand, M. D. The Proton Permeability of Liposomes Made from Mitochondrial Inner Membrane Phospholipids: Comparison with Isolated Mitochondria. *J. Membr. Biol.* **155,** 167–174 (1997).

45. Seigneuret, M. & Rigaud, J. L. Analysis of passive and light-driven ion movements in large bacteriorhodopsin liposomes reconstituted by reverse-phase evaporation. 1. Factors governing the passive proton permeability of the membrane. *Biochemistry (Mosc.)* **25,** 6716–6722 (1986).

46. Brand, M. D., Couture, P. & Hulbert, A. J. Liposomes from mammalian liver mitochondria are more polyunsaturated and leakier to protons than those from reptiles. *Comp. Biochem. Physiol. Part B Comp. Biochem.* **108,** 181–188 (1994).

47. Pennisi, C. P., Greenbaum, E. & Yoshida, K. Analysis of light-induced transmembrane ion gradients and membrane potential in Photosystem I proteoliposomes. *Biophys. Chem.* **146,** 13–24 (2010).

48. Kříž, J., Dybal, J. & Makrlík, E. Valinomycin–proton interaction in low-polarity media. *Biopolymers* **82,** 536–548 (2006).

49. Kříž, J., Makrlík, E. & Vaňura, P. NMR evidence of a valinomycin–proton complex. *Biopolymers* **81,** 104–109 (2006).

50. Garavaglia, M. *et al.* Membrane Thickness Changes Ion-Selectivity of Channel-Proteins. *Cell. Physiol. Biochem.* **14,** 231–240 (2004).

51. Kučerka, N., Nieh, M.-P. & Katsaras, J. Fluid phase lipid areas and bilayer thicknesses of commonly used phosphatidylcholines as a function of temperature. *Biochim. Biophys. Acta BBA - Biomembr.* **1808,** 2761–2771 (2011).

52. Åkesson, A. *et al.* Composition and structure of mixed phospholipid supported bilayers formed by POPC and DPPC. *Soft Matter* **8,** 5658–5665 (2012).

53. Miller, C. E., Majewski, J., Gog, T. & Kuhl, T. L. Characterization of biological thin films at the solid-liquid interface by x-ray reflectivity. *Phys. Rev. Lett.* **94,** 238104 (2005).

54. Bayerl, T. M. & Bloom, M. Physical properties of single phospholipid bilayers adsorbed to micro glass beads. A new vesicular model system studied by 2H-nuclear magnetic resonance. *Biophys. J.* **58,** 357–362 (1990).

55. Haines, T. H. Do sterols reduce proton and sodium leaks through lipid bilayers? *Prog. Lipid Res.* **40,** 299–324 (2001).

56. Shinoda, W., Mikami, M., Baba, T. & Hato, M. Molecular Dynamics Study on the Effects of Chain Branching on the Physical Properties of Lipid Bilayers: 2. Permeability. *J. Phys. Chem. B* **108,** 9346–9356 (2004).

57. Finkelstein, A. *Water movement through lipid bilayers, pores, and plasma membranes: theory and reality*. **4,** (Wiley, 1987).

58. Haines, T. H. Water transport across biological membranes. *FEBS Lett.* **346,** 115–122 (1994).

59. Ollila, S., Hyvönen, M. T. & Vattulainen, I. Polyunsaturation in Lipid Membranes: Dynamic Properties and Lateral Pressure Profiles. *J. Phys. Chem. B* **111,** 3139–3150 (2007).

60. Orsi, M., Haubertin, D. Y., Sanderson, W. E. & Essex, J. W. A Quantitative Coarse-Grain Model for Lipid Bilayers. *J. Phys. Chem. B* **112,** 802–815 (2008).

61. Orsi, M., Michel, J. & Essex, J. W. Coarse-grain modelling of DMPC and DOPC lipid bilayers. *J. Phys. Condens. Matter* **22,** 155106 (2010).

62. Krylov, N. A., Pentkovsky, V. M. & Efremov, R. G. Nontrivial Behavior of Water in the Vicinity and Inside Lipid Bilayers As Probed by Molecular Dynamics Simulations. *ACS Nano* **7,** 9428–9442 (2013).

63. Elamrani, K. & Blume, A. Effect of the lipid phase transition on the kinetics of H+/OH− diffusion across phosphatidic acid bilayers. *Biochim. Biophys. Acta BBA - Biomembr.* **727,** 22–30 (1983).

64. Disalvo, E. A., Bouchet, A. M. & Frias, M. A. Connected and isolated CH2 populations in acyl chains and its relation to pockets of confined water in lipid membranes as observed by FTIR spectrometry. *Biochim. Biophys. Acta BBA - Biomembr.* **1828,** 1683–1689 (2013).

65. Komatsu, H. & Chong, P. L. Low permeability of liposomal membranes composed of bipolar tetraether lipids from thermoacidophilic archaebacterium Sulfolobus acidocaldarius. *Biochemistry (Mosc.)* **37,** 107–115 (1998).

66. Paula, S. An Introduction to Passive Ion Transport across Model Lipid Membranes for Undergraduate Students: Proton Permeation Measurements in Liposomes. *J. Chem. Educ.* **91,** 145–148 (2014).

67. Paxton, W. F., Price, D. & Richardson, N. J. Hydroxide ion flux and pH-gradient driven ester hydrolysis in polymer vesicle reactors. *Soft Matter* **9,** 11295–11302 (2013).

68. Lande, M. B., Donovan, J. M. & Zeidel, M. L. The relationship between membrane fluidity and permeabilities to water, solutes, ammonia, and protons. *J. Gen. Physiol.* **106,** 67–84 (1995).

69. Hope, M. J., Bally, M. B., Mayer, L. D., Janoff, A. S. & Cullis, P. R. Generation of multilamellar and unilamellar phospholipid vesicles. *Chem. Phys. Lipids* **40,** 89–107 (1986).

70. De Rosa, M., Gambacorta, A. & Nicolaus, B. A New type of cell membrane, in thermophilic archaebacteria, based on bipolar ether lipids. *J. Membr. Sci.* **16,** 287–294 (1983).

71. Koyanagi, T. *et al.* Cyclohexane Rings Reduce Membrane Permeability to Small Ions in Archaea-Inspired Tetraether Lipids. *Angew. Chem.* **128,** 1922–1925 (2016).

72. Chandy, G., Grabe, M., Moore, H.-P. H. & Machen, T. E. Proton leak and CFTR in regulation of Golgi pH in respiratory epithelial cells. *Am. J. Physiol. - Cell Physiol.* **281,** C908–C921 (2001).

# CHAPTER 4

## An Artificial Electric Organ: 110 Volts from Water and Salt

Progress towards continued integration of technology into living organisms requires electrical power sources that are biocompatible, mechanically compliant, and able to harness the chemical energy available inside biological systems. Conventional batteries were not designed with these criteria in mind. The electric organ of the knifefish *Electrophorus electricus* (commonly known as the electric eel) is, however, an example of an electrical power source that operates within biological constraints while featuring power characteristics that include peak potential differences of 600 V and currents of 1 A.[1,2] Here, we introduce an eel-inspired power concept that employs gradients of ions across miniature hydrogel compartments bounded by a repeating sequence of cation- and anion-selective hydrogel membranes. The system employs a scalable stacking or folding geometry that generates 110 V or 27 $mW/m^2$ per gel cell upon simultaneous, self-registered mechanical contact activation of thousands of gel compartments in series; this design also circumvents power dissipation before contact. Unlike typical batteries, these systems are soft, flexible, transparent, and potentially biocompatible. These characteristics make artificial electric organs compelling for powering next generation implant materials in hybrids of living and nonliving systems.[3–6]

This work was accepted by *Nature* in 2017.

## 4.1 Background

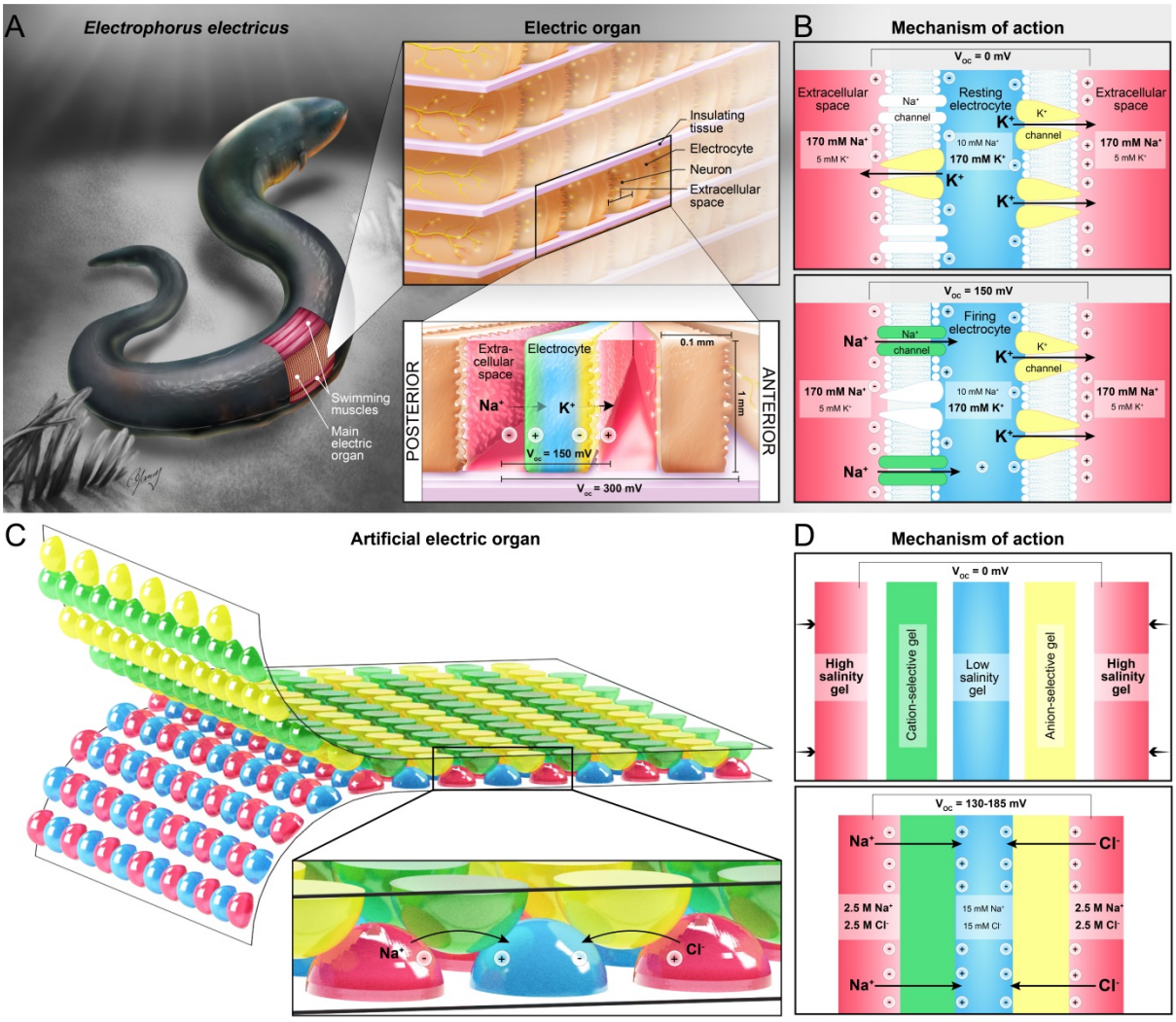


**Figure 4.1** Morphology and mechanism of action of the eel's electric organ and the artificial electric organ. **A**. Arrangement of electrocytes within the electric organs of *Electrophorus electricus*. Close-up shows ion fluxes in the firing state. **B.** Mechanism of voltage generation in electrocytes. Each cell's posterior membrane is innervated and densely packed with voltage-gated $Na^+$ channels; the anterior membrane is non-innervated and has papillar projections extending into the extracellular compartment that increase its surface area.[2] In the resting state, open $K^+$ channels in both membranes produce equal and opposite transmembrane potentials of -85 mV, so the total transcellular potential is zero. During an impulse, the $Na^+$ channels in the posterior membrane open and $K^+$ channels close in response to neural signals, generating an action potential of +65 mV from the resulting change in relative permeability to $Na^+$ and $K^+$ ions (see Section S4.1) and a total transcellular potential across both membranes of +150 mV.[2] **C.** Artificial electric organ in its printed implementation. In this and all subsequent figures, red hydrogel contains concentrated NaCl and was polymerized from neutral monomers, green gel was polymerized from negatively-charged monomers and is cation-selective, blue gel contains dilute NaCl and was polymerized from neutral monomers, and yellow gel was polymerized from positively-charged monomers and is anion-selective. **D.** Mechanism of voltage generation in artificial electric organ. Mechanical contact brings together a sequence of gels such that ionic gradients are formed across alternating charge-selective membranes, producing potentials across each membrane that add up as tetramers and can be stacked in series of thousands of gels (see Appendix S4.1).

The ability to generate electrical discharges by excitable cells has evolved independently at least six times in natural history.[1,7] The electric eel *Electrophorus electricus* in particular is a system optimized by natural selection for power generation from ionic gradients;[8,9] its specialized electric organs can generate discharges of 100 W[10] entirely from the flux of small ions. The eel employs the resulting transient current spikes to defend itself as well as to detect and incapacitate prey.[2,8] From the point of view of engineering an electrical power source for operation within a living organism[9], the electric organ of *Electrophorus* provides a fascinating example as it takes advantage of specialized anatomy and physiology (Fig. 4.1A,B) that employs thousands of membranes with densely-packed, exquisitely selective, and actuatable ion channels for generating large voltages and currents.[1,2]

Inspired by *Electrophorus*, we engineered a potentially biocompatible artificial electric organ by employing durable and accessible components as well as automated and scalable fabrication processes. This artificial electric organ is capable of generating potential differences in excess of 100 V by implementing three unique features of *Electrophorus*' electric organs.

**4.2 Biomimicry**

The first relevant feature in the eel's electric organ is the arrangement of thousands of ion gradients in series by growing long and thin electrically active cells known as electrocytes in parallel stacks that span the rear 80% of the eel's body[11] (Fig. 4.1A,B). The anterior and posterior membranes of electrocytes are bound, top and bottom, by insulating connective tissue and function as separate membranes with selectivity for two different ions such that the transcellular potentials across both membranes add up in series.[1,2,12] Figure 4.1B illustrates the mechanism of action for generating potential differences and electrical discharges by a resting

and firing electrocyte: In the resting state, the anterior and posterior membrane potentials cancel each other out. In contrast, during an impulse, the posterior membrane depolarizes to produce a total transcellular potential of approximately 150 mV (Fig. 4.1B). Large electric eels stack thousands of electrocytes in series and can generate potential differences over 600 V;[2] parallel arrangement of multiple stacks enables peak currents that approach 1 A at short circuit.[8,13]

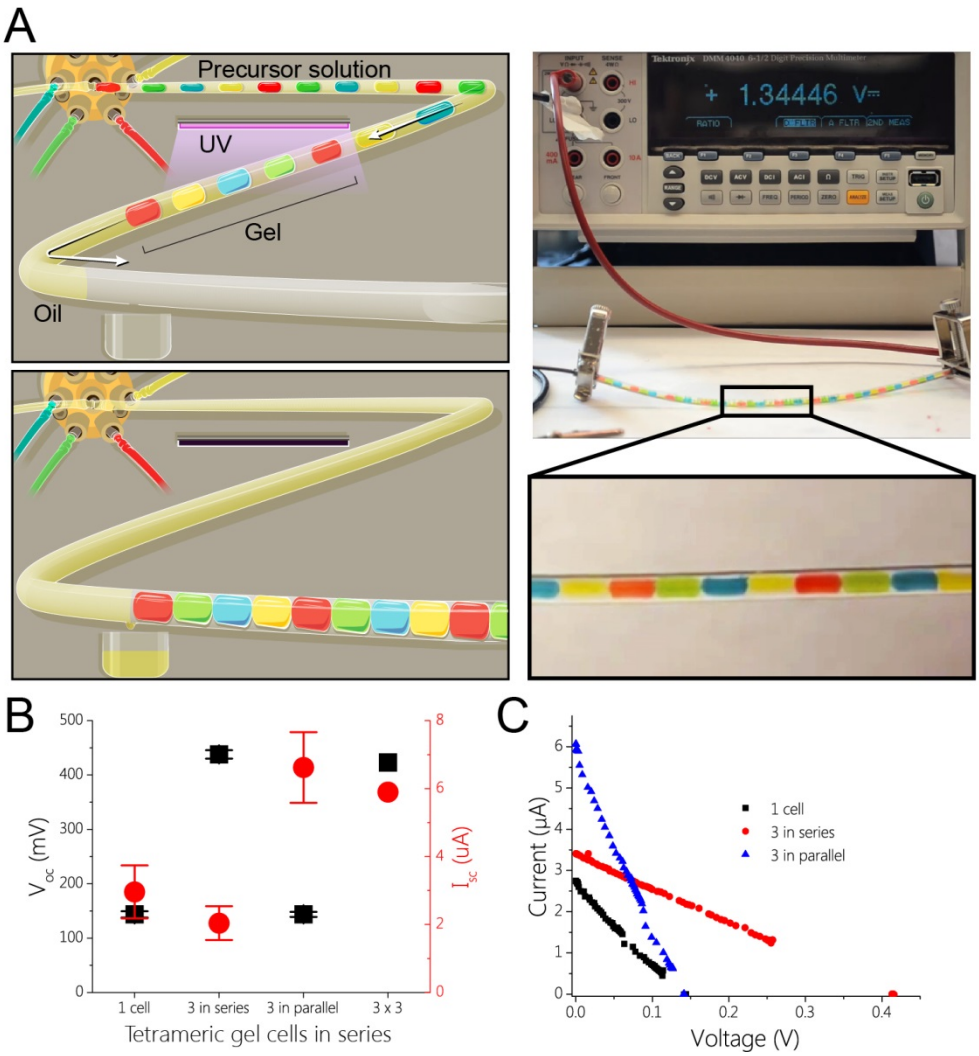


**Figure 4.2** Fluidic artificial electric organ. **A.** Left: Cartoon of a fluidic artificial electric organ before and after contact activation. Aqueous plugs of hydrogel precursor solution were generated in mineral oil, cured with a UV lamp, and sequentially brought into mechanical contact after passing a small aperture in the tubing that allowed the interstitial oil to escape. Right: Photograph of a fluidic artificial electric organ with 10 tetrameric gel cells generating 1.34 V. Scale bar = 1 cm. **B**. Open-circuit voltage and short-circuit current characteristics of fluidic artificial electric organ. Open-circuit voltages (red bars) scale linearly when tetrameric gel cells are added in series; short-circuit currents (blue bars) scale linearly when tetrameric gel cells are added in parallel. Error bars show standard deviation ($N$ = 3 except for 3×3, where $N$ = 1). **C.** Plot of current and voltage in response to various external loads for one tetrameric gel cell (black squares), three cells in series (red circles), and three cells in parallel (blue triangles).

To generate an artificial electric organ, we mimicked the anatomy of the eel by using four compositions of hydrogel as analogs of the four major components of an electrocyte, namely its two membranes with different ion selectivity on the anterior and posterior side, as well as its intracellular and extracellular salt compartments (Fig. 4.1B, Appendix S4.1, Fig. S4.1). Figure 4.1C,D illustrates that upon initiation of registered contact, tetrameric repeating units of a high salinity hydrogel, a cation-selective gel, a low salinity gel, and an anion-selective gel in sequence formed ionically conductive pathways, establishing electrolyte gradients across tens to thousands of permselective hydrogel compartments. Employing the principle of reverse electrodialysis[14], each of these "tetrameric gel cells" generated 130-185 mV at open circuit (Fig. 4.1D), a value comparable to the potential generated by a single electrocyte.[2] Figure 4.3C illustrates that the potential differences arising from 2,449 gels stacked in series added linearly to reach 110 V.

The second feature that evolved in the electric organs of *Electrophorus* ensures simultaneous excitation of electrocytes along the entire ~1 m-long organ. Since nerve signals do not travel fast enough to simultaneously activate all electrocytes within the ~2 ms duration of a discharge, *Electrophorus* ensures synchronous signal delivery by slowing down the arrival of neural impulses to the parts of the organ closest to the command nucleus.[1]

The artificial electric organ also requires simultaneous activation across many gels to circumvent energy dissipation (Appendix S4.2, Fig. S4.2). Figures 4.2 and 4.3 show two assembly strategies of an artificial electric organ, one based on fluidics and the other based on surface printing. The fluidic implementation automatically generated and positioned a series of gels sequentially using a programmable fluid dispenser (see Video S4.1, URL at end of Chapter 4 appendix). In this configuration, we prepared artificial electric organs with a maximum of 41 gels (Fig. 4.2A) and demonstrated that three gel columns in parallel delivered the expected triple

current and power (Fig. 4.2B,C, Table S4.3). Automated fluidic assembly thus makes it possible to fill devices in parallel and enables formation of a bundled artificial organ whose current and power scale with the number of gel columns analogous to the parallel electrocyte columns in the eel (Fig. 4.2B,C).[1,2] While this first implementation of the fluidically-assembled artificial electric organ required three seconds per gel plug, state-of-the-art microfluidics systems can generate water-in-oil droplets of four different compositions[15] at rates approaching $10^2$ to $10^5$ droplets per second[16] and UV-induced polymerization of hydrogel particles in a flow-through reactor has been demonstrated at a rate of 25 gelled particles per second.[17] At these rates an artificial electric organ with 2,500 gels to generate 100 V may be assembled in less than 2 min. We demonstrated that by decoupling the fabrication from the assembly, for instance in the form of a tube pre-loaded with oil-separated hydrogel beads, assembly by pressure or external fields can be achieved within seconds (Video S4.1).

As an alternative to this fluidic assembly strategy, Figure 4.3A shows truly synchronous activation of an artificial electric organ by initiating mechanical contact between two complementary gel patterns over large arrays in a registered, parallel fashion. This design prints precursor solutions of ion-selective membranes in an array of lenses on one polyester substrate and precursor solutions of salt compartments on a second substrate in complementary patterns (Fig. 4.3A and Video S4.2, URL at end of Chapter 4 appendix). When overlaid after curing, the resulting hydrogel lenses instantly form a serpentine ionically conductive pathway (Fig. 4.3A) with a repeating motif of potentials that add to 110 V (Fig. 4.3B,C).

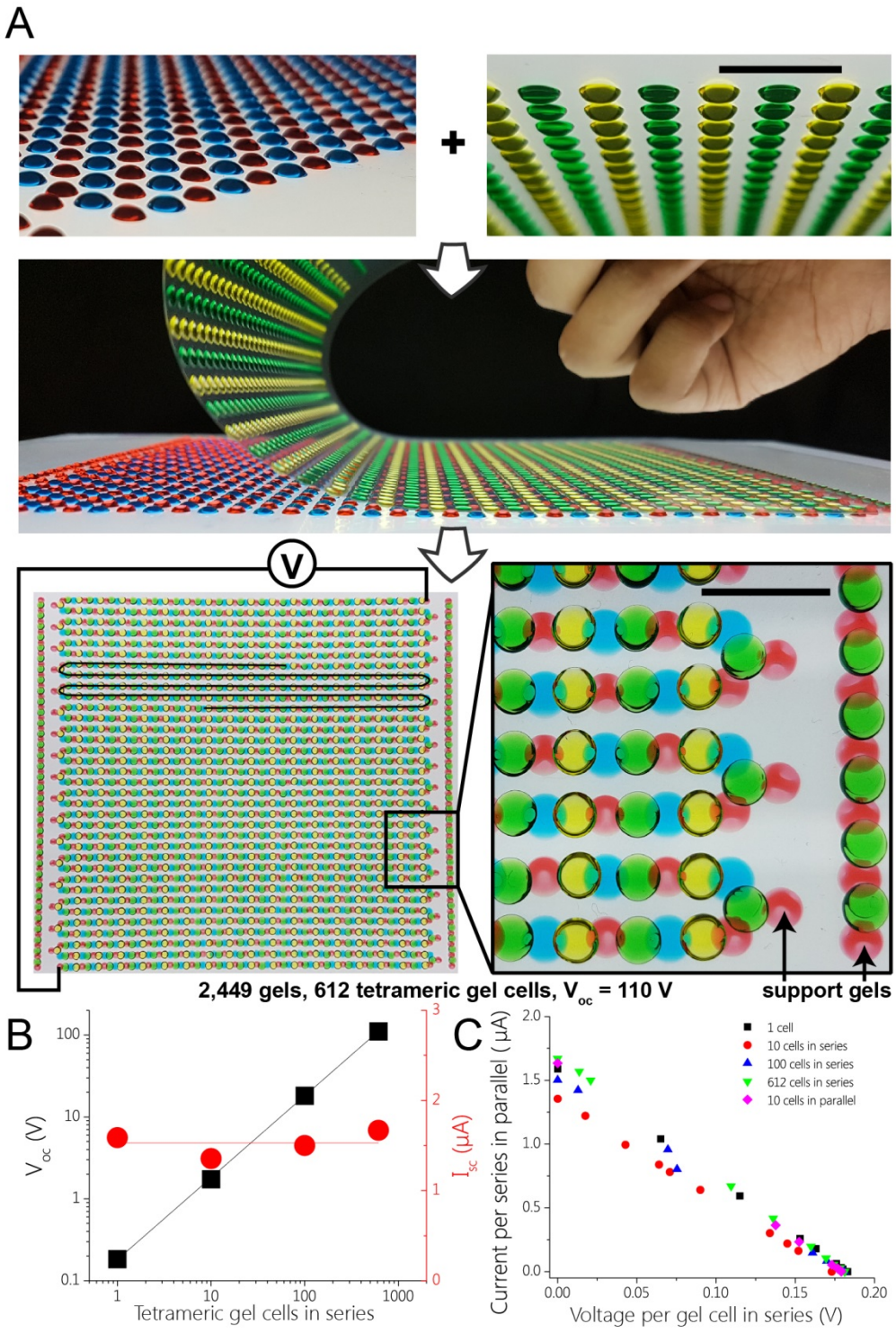


**Figure 4.3** Printed artificial electric organ. **A**. Photographs of large complementary arrays of printed hydrogel lenses combining to form continuous series of 2,449 gels with serpentine geometry. Support gels are used for mechanical stability and do not contribute to the system electrically. Scale bar = 1 cm. **B.** Open circuit voltage and short circuit current characteristics of printed artificial electric organs as a function of the number of tetrameric gel cells in a series. **C**. Normalized current-voltage relations of various numbers of tetrameric cells added in series and in parallel. The voltage axis is normalized by the number of cells in a series; the current axis is normalized by the number of series that are arranged in parallel. All points fall on one curve, as expected for a scalable system.

The third relevant feature that evolved in the electric organs of *Electrophorus* enables maintenance and regeneration of large gradients of $Na^+$ and $K^+$ ions between the electrocyte cells and the extracellular space. ATP-dependent active transport by the $Na^+/K^+$-ATPase protein accomplishes this task by counteracting passive diffusion and rebuilding gradients after a discharge.[2,18]

In the artificial electric organ, we achieved maintenance of ionic gradients by physical separation between each of the hydrogels before actuation with the benefit that this design did not require energy expenditure. We regenerated the artificial organ after discharge by applying a current to the terminal electrodes in a manner similar to Gumuscu *et al*[19] and recovered over 90% the original capacity over at least ten discharges (Appendix S4.3, Fig. S4.3).

**Table 4.1.** Comparison of parameters from the natural and artificial electric organ.

| Source | Thickness of repeating unit* (m) | Cross-sectional area of electric organ ($m^2$) | Open-circuit voltage per repeating unit (V) | Internal resistance of repeating unit ($\Omega$ $m^2$) | Maximum power density generated by repeating unit (W $m^{-2}$) |
|---|---|---|---|---|---|
| **Live eels, anterior 6-10 cm of main organ, Nachmansohn *et al*. 1942 [11†]** | $(1.1 \pm 0.2) \times 10^{-4}$ | $(2.3 \pm 0.6) \times 10^{-3}$ | 0.11 ± 0.01 | $(6.8 \pm 0.7) \times 10^{-4}$ | 5.5 ± 1.4 |
| **Live eels, sections of main organ, Cox *et al*. 1946 [13‡]** | $10^{-4}$ | $(3.4 \pm 0.5) \times 10^{-3}$ | 0.12 ± 0.01 | $(5.1 \pm 0.4) \times 10^{-4}$ | 10.6± 2.0 |
| **Live eels, leaping, Catania 2016 [8§]** | $10^{-4}$ | $2.8 \times 10^{-3}$ | 0.16 | $4.8 \times 10^{-4}$ | 13.6 |
| **Gel cells, this work, 80˚ fold** | $2.8 \times 10^{-3}$ | $8.5 \times 10^{-5}$ | 0.17 ± 0.01 | 0.27 ± 0.02 | 0.027 ± 0.002 |

* Repeating unit refers to an electrocyte in the eel's electric organ and to a tetrameric gel cell in this work.
† Parameters are averages of the farthest anterior measurements for each of the 4 eels from that paper's Table 2. Cross-sectional area estimated from eels of corresponding length in Table 1 of Cox *et al*. 1946 [13].
‡ Parameters are averages of all measurements from that paper's Table 1. Repeating unit thickness is an estimate reported in that paper. Open-circuit voltage values were calculated by multiplying reported electromotive force values by a factor of 0.77 (an average factor reported in the paper). Unit resistance and power density were estimated for each eel based on the approximation made in the paper that the external resistance was approximately equal to the internal resistance of the system.
§ Average of two experiments. Open-circuit voltage and short-circuit current extracted from highest position attained by each ascending eel where both parameters are shown in that paper's Figure 4C. Cross-sectional area estimated from eels of corresponding length in Table 1 of Cox *et al*. 1946[13], repeating unit thickness estimated from anterior voltage distributions reported in Cox *et al*. 1940 [20]. Assumptions: eel tilt angle = 70˚; electric organ begins 20% of reported eel length from its front tip[11], resistance in the water tank from that paper's Figure 3 is negligible.

## 4.3 Optimization

In terms of performance as a power source, the electric organs of *Electrophorus* can generate 600 V by stacking parallel columns of 100 μm-thin electrocytes with membrane contact areas as large as 7,000 $mm^2$,[13] minimizing the resistance of a layer of electrocytes to ~ 0.1 Ω (Table 4.1) and enabling discharges of 100 W.[10] By comparison, the 110 V implementation of the artificial electric organ involved a conductive pathway along thousands of relatively thick hydrogel lenses with a small cross-sectional contact area (Fig. 4.3A), increasing the resistance to 115 kΩ per tetrameric gel cell and limiting the power output to 50 μW across 2,449 gels (Fig. 4.3B,C, Appendix S4.4).

To improve the performance, we devised flat hydrogel films on a patterned substrate and took advantage of a folding strategy developed for use in space to unfold solar panels (Fig. 4.4A, Appendix S4.5, Fig. S4.5). This *Miura-ori* fold makes it possible to stack a repeating series of thin films with large contact area in a single synchronized and self-registered motion[21] (Video S4.3, URL at end of Chapter 4 appendix). Table 4.1 shows that stacking 0.7-mm thin films using an 80˚ *Miura-ori* fold yielded an artificial electric organ with a maximum power density of 27 ± 2 mW $m^{-2}$ per tetrameric gel cell due to an approximately 40-fold reduction in resistance compared to lateral conduction through films of similar dimensions in the serpentine arrangement (Fig. 4.4B). As summarized in Table 4.1, the power density generated by this most efficient gel cell geometry is, however, still 2-3 orders of magnitude smaller than electrocyte layers in *Electrophorus.*[12,13]

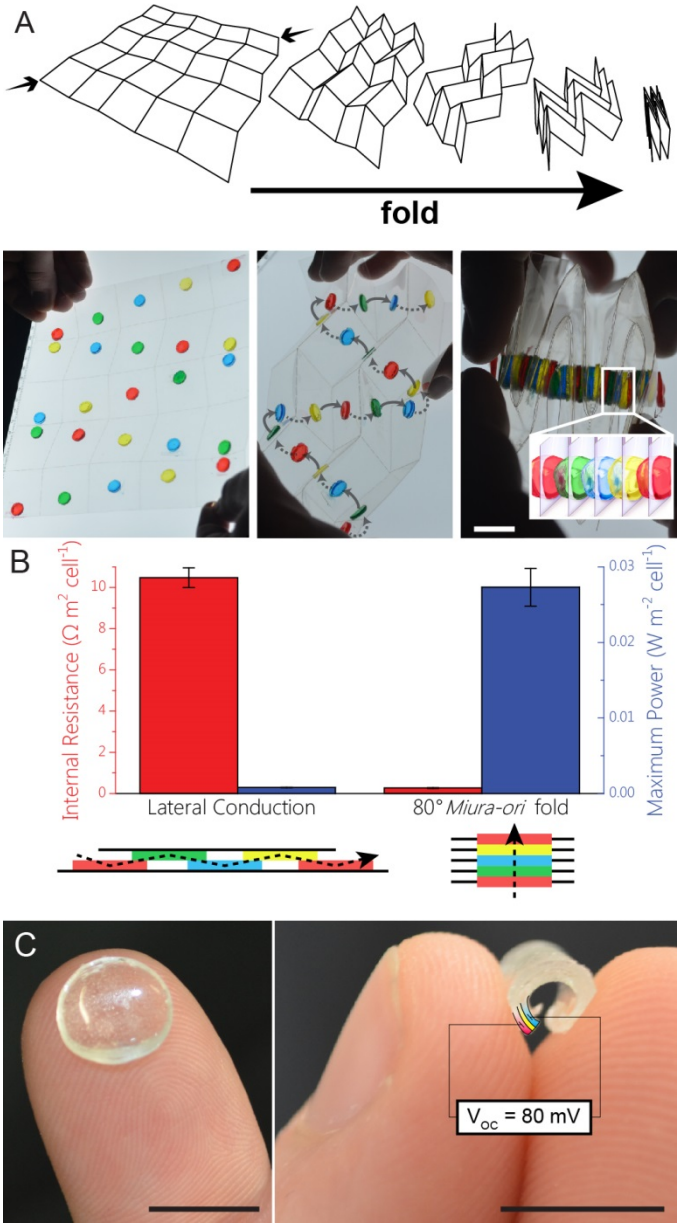


**Figure 4.4** Artificial electric organ morphologies based on thin hydrogel films. **A.** Schematic and photographs of *Miura-ori* folding. A single motion compresses a two-dimensional array of panels into a self-registered folded state where all panels overlap, generating a one-dimensional sequence[21]. This morphology was used to generate flat and large contact areas between a series of thin gel films, which conducted ions from gel to gel through holes in the supporting polyester substrate. Scale bar = 1 cm. **B.** Area-normalized internal resistance (red) and maximum power (blue) per tetrameric gel cell with 0.7 mm thick gel films arranged either laterally in a manner that approximates the relative geometry of the serpentine implementation or in a *Miura-ori*-assembled stack (Appendix S4.4). The stack geometry imparts a 40-fold reduction in resistance and a corresponding 40-fold improvement in maximum power output. **C.** Flexible and transparent artificial electric organ prototype with the shape of a contact lens composed of a gel trilayer of high salinity gel (indicated by a false-colored section in red), anion-selective gel (yellow), and low salinity gel (blue) with a total thickness of 1.2 mm that produced an open-circuit voltage of 80 mV. Scale bars = 1 cm.

Bringing the design parameters of the artificial electric organ closer to the eel provides opportunities for further improving its performance. Electrocytes are thinner than the gel films shown in Fig. 4.4A by a factor of at least 7, and the absolute permeabilities of the ion-selective gel membranes used here were 10 times smaller than the ion permeabilities of electrocyte membranes (Table S4.2).[22] We showed that reducing the thickness of the hydrogel films by an order of magnitude increases the power density fivefold (Fig. S4.6) and films of hydrogels as thin as a few hundred nanometers have been demonstrated in a different context.[23] Additionally, both the intracellular and extracellular compartments in the electric organs of *Electrophorus* are at physiological ionic strength of ~180 mM[12] imparting low resistivity, while the artificial electric organ's low-salinity compartment contains only 15 mM sodium chloride and contributes most of the system's electrical resistance (Fig. S4.6). In this regard, the work here highlights a non-obvious strategy the eel evolved to maximize power output. By developing electrocyte cells with two functionally different membranes such that, in the firing state, the posterior membrane is permeable specifically to sodium ions and the anterior membrane is permeable specifically to potassium ions (Fig. 4.1B), electrocytes convert the energy stored in opposing ion gradients of two different cations between physiological intracellular and extracellular solutions with low resistivity. In contrast, the broadly cation- or anion-selective hydrogel membranes in the artificial electric organ cannot distinguish between two different cations or anions, necessitating a gradient in overall ionic strength to establish a potential difference and hence inherently requiring one compartment with lower ionic strength and significantly higher resistivity than the other (see Appendix S4.6). Therefore, development of ultrathin synthetic membranes with improved ion selectivity[24] provides an opportunity to increase the power density of artificial electric organs.

## 4.4 Outlook

Even before implementing these possible improvements, the unique material properties of artificial electric organs may inspire opportunities that cannot be imagined with conventional batteries. One example is the development of an electrically active contact lens made from hydrogel films. Contact lenses are commonly fabricated from hydrogels[25] and prototypes with integrated displays and sensors have been reported.[26,27] To realize such functional lenses, an integrated and optically transparent power harvesting scheme would be enabling. Figure 4.4C illustrates a first step towards this vision. A single tri-layered lens generated a potential difference of 80 mV, hinting at the possibility of developing moldable, flexible, and optically transparent power sources for wearable and implantable devices.[5]

The work presented here introduces the first implementation of an artificial electric organ from potentially biocompatible materials. By employing thousands of compartmentalized ion gradients as well as scalable fabrication combined with synchronized assembly of ion-selective membranes, these materials are able to generate total open-circuit potential differences in excess of 100 V and power densities of 27 mW $m^{-2}$ per tetrameric gel cell. While these characteristics are only just approaching a useful power level for the lowest-power implant devices,[28] advanced designs – possibly with thinner and more selective membranes – combined with strategies to recharge and activate[29] these artificial organs inside a living body[30] are likely to increase their utility. Clearly, the eel's electric organ demonstrates that organic electrical power sources inside living organisms can operate with exquisite power characteristics by utilizing metabolically available energy. If next generation designs can shorten the performance gap between the artificial and natural electric organ by one or two orders of magnitude then these artificial

electric organs may open the door to metabolically sustained electrical energy for powering implants, wearables, and mobile devices during their complete life cycle.

## 4.5 Methods

*Materials and Equipment*

We purchased all chemicals from Sigma-Aldrich (Merck KGaA, Darmstadt, Germany) except for 40% acrylamide/N,N'-methylenebisacrylamide (henceforth "bis") solution, which we purchased from Bio-Rad (Hercules, CA, USA) and P100 hydrophilic solution, which we purchased from Jonsman Innovation (Gørløse, Denmark). We purified all water to 18.2 MΩ cm with a PURELAB Flex II purifier (ELGA LabWater, Veolia, Paris, France). We performed all fluidic gel handling with a FIAlab-3500 multi-analysis instrument (FIAlab Instruments Inc., Seattle, WA, USA) and an Infuse/Withdraw Pump 11 Elite programmable syringe pump (Harvard Apparatus, Holliston, MA, USA) in Tygon tubing (1/16" ID, 1/8" OD, McMaster-Carr, Elmhurst, IL, USA). We printed all patterns using a BioFactory 3D bioprinter (regenHU, Villaz-St-Pierre, Switzerland) with a custom print plate machined at the University of Fribourg. The transparent substrates were A4-sized uncoated polyester overhead transparencies with a thickness of 0.1 mm (Avery Zweckform #3555, Oberlaindern, Germany); we cut them using a Speedy 300 laser cutter (Trotec, Marchtrenk, Austria). We cured all gels using a Mineralight UV Display lamp (UVP, Analytik Jena, Jena, Germany) containing two 25-watt 302-nm or 365-nm UV tubes (Ushio Inc., Tokyo, Japan).

*Characterization of artificial electric organs*

The first and final gel compartment of each series of gels was a high-salinity reservoir gel. We inserted Ag/AgCl wire electrodes into the first and final gel of each series, or in identical high-salinity reservoir gels that we brought in contact with the terminal gels. We recorded voltages using a Tektronix DMM4040 digital multimeter set to high input impedance mode and short-circuit currents using a Keithley 2400 SourceMeter using a source voltage of zero (except where noted). We constructed I-V curves (Figs. 4.2C, 4.3C) by connecting a series of known load resistances to the batteries while monitoring the voltage across the load.

*Fluidic artificial electric organ*

The gel precursor solutions were all aqueous and had the following compositions: Low-salinity gel: 0.015 M sodium chloride, 0.045 M 2-hydroxy-4'-(2-hydroxyethoxy)-2-methylpropiophenone (henceforth "photoinitiator"), 5.5 M acrylamide, 0.067 M bis. High-salinity gel: 0.5 M sodium chloride, 0.045 M photoinitiator, 5.4 M acrylamide, 0.066 M bis. Cation-selective gel: 2.0 M 2-acrylamido-2-methylpropane sulfonic acid, 0.014 M photoinitiator, 3.7 M acrylamide, 0.045 M bis. Anion-selective gel: 2.0 M (3-acrylamidopropyl)trimethylammonium chloride, 2.75 M acrylamide, 0.034 M bis. We used McCormick food dye to differentiate the gels during experiments.

We connected the inlets of the FIAlab multi-position valve to sources containing the four different gel precursor solutions, and another containing mineral oil. A holding coil connected the main outlet of the valve to a syringe, which we used to withdraw liquids from the selected source into the holding coil. The main outlet was also connected to another source of mineral oil, which we pumped back through the outlet into a separate waste line to remove excess gel

precursor. We programmed the FIAlab to withdraw a sequence of plugs of gel precursor solution ([high-salinity, cation-selective, low-salinity, anion-selective] x the number of repeats in the series), separating them with spacer plugs of mineral oil to prevent mixing of gels. After producing the desired number of plugs, we removed the collection tube and cured the gels under the UV lamp (365 nm) at a distance of 25 mm for 90 seconds. We connected the collection tube to a syringe filled with oil, then cut a notch-shaped opening on the opposite end of the tube, smaller than the thickness of the gel plugs. When we pushed the plugs past this notch, the interstitial oil escaped through the small opening and brought the entire sequence of gels into contact. We fabricated the first and final high-salinity gels separately and embedded the electrodes before curing. We connected these gels to the ends of the stacked gel sequence while applying light pressure and clamped them into place before electrical characterization. Video S4.1 illustrates the entire process.

*Printed serpentine artificial electric organ for high voltages*

The gel precursor solutions were aqueous and had the following compositions: Low-salinity gel: 0.015 M sodium chloride, 0.045 M photoinitiator 4.1 M acrylamide, 0.051 M bis, and 3.4 M glycerol. High-salinity gel: 2.5 M sodium chloride, 0.045 M photoinitiator, 5.1 M acrylamide, 0.062 M bis. Cation-selective gel: 2.0 M 3-sulfopropyl acrylate (potassium salt), 0.045 M photoinitiator, 1.9 M acrylamide, 0.055 M bis. Anion-selective gel: 2.0 M (3-acrylamidopropyl)trimethylammonium chloride, 2.75 M acrylamide, 0.034 M bis. Food dye from Städter was only used for photography and was absent during electrical recording experiments.

We printed two complementary arrays of 8 μL droplets of gel precursor solution on separate substrates in geometries that formed a single serpentine ionic pathway when overlaid (Fig. 4.3A). All the selective gel precursor droplets were printed onto the same substrate; the reservoir gel precursor droplets were printed onto the other one. After we finished printing onto a substrate, we immediately removed that substrate from the print plate and cured the gels under the UV lamp (302 nm) at a distance of 12 mm for 30 seconds. Once both substrates had been prepared, we overlaid them and applied a pressure of 16 kPa to the assembly to ensure contact between each of the gels in the series. In these experiments, voltages were collected with the SourceMeter using a source current of zero and currents were collected with a Keithley 6487 picoammeter.

*80˚ Miura-ori folded artificial electric organ*

The gel precursor solutions were the same as in the printed artificial electric organ. We laser-cut a 0.1 mm-thick polyester substrate with perforations in the Miura-ori pattern (80˚, short edge of the parallelogram = 4 cm, long edge = 4.06 cm) and one 7 mm-diameter circular hole in each parallelogram positioned such that all the holes would overlap upon folding. We then attached PDMS pads with circular openings (depth = 0.3 mm, inner diameter = 10.5 mm) around each hole on both sides of the substrate, followed by manually pipetting the gel precursor solutions into each of the holes such that the PDMS reservoirs on both sides of the substrate were filled. We cured the solutions under a UV lamp (302 nm) at a distance of 12 mm for 30 seconds, then flipped the substrate over and cured the system for another 30 s. We peeled the PDMS reservoirs off the substrate before folding the substrates to bring the gels into contact (Fig. 4.4A).

Painting a thin layer of deionized water onto both sides of each gel before folding prevented the gels from detaching from the substrate upon unfolding.

The power characteristics of the 80˚ *Miura-ori* folded geometry are compared with a lateral geometry of gels of the same dimensions as the ones shown in Figure 4.4A. To make the lateral analogues, we attached PDMS pads with circular openings to two planar substrates (depth = 0.7 mm, inner diameter = 10.5 mm) with the rings on each substrate spaced 5 mm apart from one another to approximate the relative geometry of the serpentine implementation. We filled the openings on one substrate with alternating membrane precursor solutions and the openings on the other with alternating reservoir precursor solutions, then cured them with the same parameters as the 80˚ *Miura-ori* gels and registered them as with the serpentine geometry.

*Gel trilayer in the shape of a contact lens*

The gel precursor solutions were the same as in the printed artificial electric organ. We made thin reservoirs by mounting substrates above a block of Teflon with double-sided tape, pipetted the precursor solutions into the reservoirs, and cured them under a UV lamp (302 nm) at a distance of 12 mm for 30 seconds to form thin (0.4 mm) sheets of the low-salinity, high-salinity, and anion-selective gels. We assembled the gel films into a trilayer and used a biopsy punch to obtain a circular cutout (diameter = 10.5 mm).

## 4.6 Contributions of others

I collected all the data shown here alongside Anirvan Guha, who was a key work and discussion partner throughout this project. Along with Gloria VanRenterghem, Anirvan defined the parameters of the fluidic implementation of the organ. Aaron Lamoureux and Max Shtein

provided the idea of *Miura-ori* folding and laser-cutting substrates. David Sept validated my analysis of published electrical data sets taken from *Electrophorus*. The project was conceived by Michael Mayer, Jerry Yang, Anirvan Guha, and myself.

## Chapter 4 Appendix

### S4.1. Theoretical Background

An ionic gradient across a selectively permeable membrane gives rise to an electromotive force across that membrane. This phenomenon can be described and modeled as follows:

The Nernst-Planck equation (Equation S4.1) defines the flux of ion *s* in an electric field.

$$J_s = -D_s \left[ \nabla c_s + \frac{F z_s}{RT} c_s \nabla \varphi \right] \quad \text{(S4.1)}$$

$J_s$ (mol m$^{-2}$ s$^{-1}$) is the molar flux of ion *s*, $D_s$ (m$^2$ s$^{-1}$) is the diffusion coefficient of *s* in its medium, $c_s$ (mol m$^{-3}$) is the molar concentration of *s*, $F$ (C mol$^{-1}$) is Faraday's constant, $z_s$ is the charge of *s*, $R$ (J mol$^{-1}$ K$^{-1}$) is the gas constant, $T$ (K) is the temperature, and $\varphi$ (V) is the electrical potential. In the 1940s, Goldman, Hodgkin, and Katz formulated a version of this equation for considering electric currents in biological membrane systems by making the assumptions that the membrane behaves as a homogeneous medium, that the electric field is constant throughout the membrane, and that fluxes of ions are independent of one another.[31–34] Equation S4.2 shows the resulting Goldman-Hodgkin-Katz (GHK) current equation.

$$I_s = P_s V F^2 z_s^2 \frac{[\mathrm{S}]_i - [\mathrm{S}]_o e^{-VFz_s/RT}}{RT\,(1 - e^{-VFz_s/RT})} \quad \text{(S4.2)}$$

$I_s$ (A m$^{-2}$) is the current density carried by *s* across the membrane, $P_s$ (m s$^{-1}$) is the permeability of *s* through the membrane, $V$ (V) is the voltage across the membrane, and $[\mathrm{S}]_i$ and $[\mathrm{S}]_o$ (mol m$^{-3}$) are the concentrations of *s* inside and outside the cell. Sodium, potassium, and chloride are the

three ions most relevant to the study of excitable membranes. When formulated to consider the total ionic current density $I$ (A m$^{-2}$) from the combined flux of these three ions, the GHK current equation appears as Equation S4.3.[32]

$$I = \frac{VF^2\left[(P_{Na}[\mathrm{Na^+}]_i + P_K[\mathrm{K^+}]_i + P_{Cl}[\mathrm{Cl^-}]_o) - (P_{Na}[\mathrm{Na^+}]_o + P_K[\mathrm{K^+}]_o + P_{Cl}[\mathrm{Cl^-}]_i)e^{-VF/RT}\right]}{RT(1-e^{-VF/RT})} \quad \text{(S4.3)}$$

At open circuit ($I$ = 0), Equation S4.3 reduces to the GHK voltage equation (Equation S4.4).[32]

$$V_{OC} = \frac{RT}{F}\ln\left(\frac{P_{Na}[\mathrm{Na^+}]_o + P_K[\mathrm{K^+}]_o + P_{Cl}[\mathrm{Cl^-}]_i}{P_{Na}[\mathrm{Na^+}]_i + P_K[\mathrm{K^+}]_i + P_{Cl}[\mathrm{Cl^-}]_o}\right) \quad \text{(S4.4)}$$

$V_{OC}$ (V) is the open-circuit or zero-current voltage across the membrane. (By the convention used here, positive membrane potentials indicate that the interior of the cell is positive with respect to the exterior; note that this is the opposite of the convention used by Hodgkin and Katz.[32]) If the membrane is completely nonselective (i.e. $P_{Na} = P_K = P_{Cl}$) or no concentration gradient exists ($[\mathrm{S}]_i = [\mathrm{S}]_o$ for all species $s$), no voltage will arise.

Increasing the ratio of the ion permeabilities or the concentration gradient between compartments increases the voltage across the membrane. On the other hand, increasing the magnitude of the membrane's *absolute* permeability to the ions will increase the ionic current through the membrane. Permselectivity and absolute permeability are therefore critical parameters that define the power characteristics of this type of membrane system. A discussion of how to determine these parameters follows.

In a membrane system containing only two ions with sufficiently high concentrations and membrane permeances to impact the electrochemical environment, the third ion can be disregarded and removed from this equation on the basis of having negligible concentration or permeability. Subsequently, the ratio of the membrane's permeability to each of the two relevant ions can easily be determined from the open-circuit voltage and species concentrations. Equation S4.5 considers sodium and potassium, the two most permeant ions in the electrocytes of *Electrophorus electricus* (multiple reports indicate that chloride conductance is minimal by comparison[35–37]).

$$\frac{P_{Na}}{P_K} = \frac{[\mathrm{K^+}]_i \, e^{V_{OC}F/RT} - [\mathrm{K^+}]_o}{[\mathrm{Na^+}]_o - [\mathrm{Na^+}]_i \, e^{V_{OC}F/RT}} \tag{S4.5}$$

In the electric eel, electrocyte interiors contain high concentrations of potassium (150 mM) and low concentrations of sodium (5 mM); the extracellular compartments contain high concentrations of sodium (160 mM) and low concentrations of potassium (2.5 mM). The resting potential of the membranes is -85 mV, reflecting the membrane's open $K^+$-selective channels in the resting state.[2,38] As described in the main text, in the posterior electrocyte membrane these $K^+$ channels close and voltage-gated $Na^+$ channels open in response to a neural impulse; these changes comprise a sudden modulation of $P_{Na}$ and $P_K$ that triggers the reversal of the membrane voltage to +65 mV at its peak.[2,22,38] Table S4.1 shows the permeability ratios of the posterior electrocyte membrane in the resting state and at the peak of an impulse. The anterior membrane displays no electrical excitability and constantly maintains the resting permeability ratio.

Equation S4.6 considers sodium and chloride, the two mobile ions present in the tetrameric hydrogel cells presented here.

**Table S4.1.** Selectivity of membranes considered in this work.

| Reference | $[Na^+]_{in}$ (M) | $[Na^+]_{out}$ (M) | $[K^+]_{in}$ (M) | $[K^+]_{out}$ (M) | Membrane | $V_{oc}$ (mV)* | $P_{Na}/P_K$† | $P_K/P_{Na}$† |
|---|---|---|---|---|---|---|---|---|
| Keynes and Martins-Ferreira, 1953[12] ‡ | 0.01 [39] | 0.172 | 0.17 [39] | 0.005 | Main organ, resting | -70.2 ± 2.9 | .0354 | 28.3 |
| | | | | | Main organ, peak | +55.1± 4.4 | 16.8 | 0.0597 |
| | | | | | Sachs organ, resting | -78.1± 4.2 | .0182 | 55.1 |
| | | | | | Sachs organ, peak | +61.9 ± 2.1 | 31.3 | 0.0319 |
| Altamirano and Coates, 1957[40] ‡ | 0.01 [39] | 0.19 | 0.17 [39] | 0.005 | Sachs organ, resting | -84.0 ± 5.2 | .00789 | 127 |
| | | | | | Sachs organ, peak | +52.5 ± 2.6 | 11.7 | 0.0858 |
| Nakamura *et al.*, 1965[38] ‡ | 0.01 [39] | 0.172 | 0.17 [39] | 0.005 | Sachs organ, resting | -84.9 ± 2.7 | .00366 | 140 |
| | | | | | Sachs organ, peak | +52.3 ± 4.1 | 13.6 | 0.0734 |
| Shenkel and Sigworth 1991[22] | 0 | 0.2 | 0.2 | 0 | Main organ, cell-attached patch, peak | +78.6 ± 6.7 | 21.3 | 0.0468 |
| | | | | | Main organ, inside-out patch, peak | +72.7 ± 11 | 16.9 | 0.0590 |
| | | | | | Sachs organ, cell-attached, peak | +78.6 ± 6.6 | 21.3 | 0.0468 |
| | | | | | Sachs organ, inside-out patch, peak | +73.6 ± 4.1 | 17.6 | 0.0568 |
| | $[Na^+]_{in}$ (M) | $[Na^+]_{out}$ (M) | $[Cl^-]_{in}$ (M) | $[Cl^-]_{out}$ (M) | Membrane | $V_{oc}$ (mV) | $P_{Na}/P_{Cl}$ | $P_{Cl}/P_{Na}$ |
| This work | 0.015 | 2.5 | 0.015 | 2.5 | Anion-selective gel | -89.3 ± 0.6 | 0.0249 ± 0.0008 | 40.3 ±1.2 |
| | | | | | Cation-selective gel | +82.3 ± 1.5 | 29.5 ± 1.9 | 0.0343 ± 0.0024 |

Electrocyte membranes listed here are all the posterior, innervated membranes; anterior membranes maintain resting potential over the duration of a discharge[12]. Permeability ratios calculated using Equations S4.5 and S4.6.
* When applicable, values here and throughout this work are presented as mean ± S.E.M.
† Calculated from mean zero-current voltage.
‡ Interior concentration values not provided; taken from Schoffeniels 1959[39].

$$\frac{P_{Na}}{P_{Cl}} = \frac{[\mathrm{Cl}^-]_o \, e^{V_{OC}F/RT} - [\mathrm{Cl}^-]_i}{[\mathrm{Na}^+]_o - [\mathrm{Na}^+]_i \, e^{V_{OC}F/RT}} \tag{S4.6}$$

Fixed charges in ion exchange membranes cause those membranes to be quite permeable to oppositely-charged counter-ions while rejecting co-ions of the same charge sign, a principle known as Donnan exclusion.[41] Likewise, including charged monomers (Fig. S4.1) imparted charge-based ionic selectivity to the hydrogels considered in this work. Measuring the open-circuit voltage across the cation- and anion-selective hydrogels used here in the presence of a

salinity gradient yielded each gel's permeability ratio according to Equation S4.6 (Table S4.1). The strategy of creating additive potentials by separating alternating fresh-water and saline reservoirs with alternating cation- and anion-selective membranes is known as reverse electrodialysis; flow systems using this arrangement are an emerging alternative energy technology for extracting electrical power from naturally-occurring salinity gradients.[42–46]

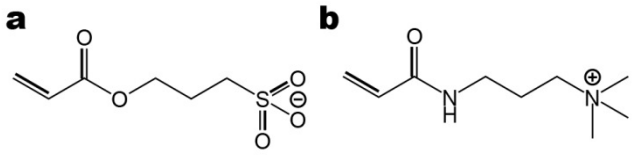


**Figure S4.1**. Charged monomers used in charge-selective "membrane" gels. **A.** 3-sulfopropyl acrylate, a component of the cation-selective gel. **B**. (3-acrylamidopropyl)trimethylammonium, a component of the anion-selective gel.

Calculating the *absolute* permeability of a membrane to an ionic species from an electrical recording requires the use of the GHK current equation. If a full current-voltage relation for a membrane is known (as with the artificial organ presented here), it can be fit directly to Equation S4.3;[22,32] absolute permeabilities of selective gels calculated in this way are shown in Table S4.2. Alternatively, a first approximation can be obtained from membrane resistance or conductance values reported in, or approximated from, electrophysiology literature using Equation S4.7, first reported by Hodgkin and Katz in 1949:

$$G = \frac{V_{OC}F^3}{R^2T^2}\left[\frac{(P_{Na}[\mathrm{Na^+}]_o+P_K[\mathrm{K^+}]_o+P_{Cl}[\mathrm{Cl^-}]_i)(P_{Na}[\mathrm{Na^+}]_i+P_K[\mathrm{K^+}]_i+P_{Cl}[\mathrm{Cl^-}]_o)}{(P_{Na}[\mathrm{Na^+}]_o+P_K[\mathrm{K^+}]_o+P_{Cl}[\mathrm{Cl^-}]_i)-(P_{Na}[\mathrm{Na^+}]_i+P_K[\mathrm{K^+}]_i+P_{Cl}[\mathrm{Cl^-}]_o)}\right] \quad \text{(S4.7)}$$

where G ($\Omega^{-1}$ $m^{-2}$) is the membrane's area-normalized conductance, defined as $(dI/dV)_{I\to 0}$. In the context of electrocytes with negligible chloride flux, this relationship can be reformulated as

Equation S4.8. If the open-circuit voltage and ion concentrations are known, the permeability ratio can be calculated as in Equation S4.5, making the absolute permeability of both ions accessible.

**Table S4.2.** Absolute permeability values of membranes considered in this work.

| Reference | $[Na^+]_{in}$ (M) | $[Na^+]_{out}$ (M) | $[K^+]_{in}$ (M) | $[K^+]_{out}$ (M) | Membrane | $V_{oc}$ (mV) | $P_{Na}$ (m $s^{-1}$) | $P_K$ (m $s^{-1}$) |
|---|---|---|---|---|---|---|---|---|
| Shenkel and Sigworth 1991[22] * | 0 | 0.2 | 0.2 | 0 | Sachs organ inside-out patch, peak | +75.3 ± 2.4 | (1.91 ± 0.28) x $10^{-7}$ | (8.74 ± 1.10) x $10^{-9}$ |
| | $[Na^+]_{in}$ (M) | $[Na^+]_{out}$ (M) | $[Cl^-]_{in}$ (M) | $[Cl^-]_{out}$ (M) | Membrane | $V_{oc}$ (mV) | $P_{Na}$ (m $s^{-1}$) | $P_{Cl}$ (m $s^{-1}$) |
| This work | 0.015 | 2.5 | 0.015 | 2.5 | Anion-selective gel | -89.3 ± 0.6 | (6.71 ± 4.10) x $10^{-10}$ | (2.61 ± 1.51) x$10^{-8}$ |
| | | | | | Cation-selective gel | 82.3 ± 1.5 | (2.03 ± 0.33) x $10^{-8}$ | (7.44 ± 1.71) x$10^{-10}$ |

Permeabilities calculated using Equations S4.3 and S4.8.
* Values calculated from reported values of reversal potential ($E_r$) and maximum current ($I_{max}$) from that paper's Table 1. Assumptions: (1) $I_{max}$ occurs at +10 mV (reported average value) for all traces. (2) Ohmic behavior between $E_r$ and $I_{max}$ (appears approximately true based on the shape of the curve in that paper's Figure 1B). (3) Patch area was 10 μm$^2$ (assumed in discussion).
Comparisons of absolute permeabilities in main text were made based on these values from firing electrocytes.

$$P_{Na} = \frac{R^2T^2G}{F^3V_{OC}}\left[\frac{\left([\mathrm{Na}^+]_o+\frac{P_K}{P_{Na}}[\mathrm{K}^+]_o\right)-\left([\mathrm{Na}^+]_i+\frac{P_K}{P_{Na}}[\mathrm{K}^+]_i\right)}{\left([\mathrm{Na}^+]_o+\frac{P_K}{P_{Na}}[\mathrm{K}^+]_o\right)\left([\mathrm{Na}^+]_i+\frac{P_K}{P_{Na}}[\mathrm{K}^+]_i\right)}\right] \quad \text{(S4.8)}$$

Approximate values for the absolute ion permeabilities of the posterior, innervated membrane in its firing state that we calculated in this way from data reported by Shenkel and Sigworth[22] appear in Table S4.2. Unfortunately, many of the other published data sets from *Electrophorus* were collected across whole cells rather than individual membranes,[13] did not report normalization factors such as area required to approximate current-voltage relations or conductances,[12,40] or focused on conductances at timepoints after the peak to study phenomena such as $K^+$ channel inactivation,[40,47] limiting the number of data sets that we could use in this comparison. Further, early voltage-clamp setups were likely plagued by leak current

pathways[38,48] (as detailed in [22]), as measured membrane resistances increased significantly with the advent of modern patch-clamp technique.[22] The assumptions required for the calculations appear in the footnotes of the table; accordingly, these values should be taken as a first approximation. A rare reported absolute $P_{Na}$ value ($3.4 \times 10^{-7}$ m $s^{-1}$ for experiment 8179b.1a in Shenkel and Sigworth's Table 1, reported on that paper's p. 1018[22]) confirms the validity of our assumptions, as the corresponding $P_{Na}$ for that experiment calculated from the parameters reported in that paper's Table 1 is $3.6 \times 10^{-7}$ m $s^{-1}$.

Ionic permeabilities and their ratios are important parameters of membranes in energetic contexts because they determine a membrane's power characteristics. Practically speaking, however, the power characteristics are more easily determined directly. We present a discussion of the internal resistance $R_{int}$ and the maximum power density $D_{max}$, the two parameters most relevant to a membrane system's ability to generate electrical power, in Appendix S4.4.

**S4.2. Dissipation experiments at open circuit**

When an ionic gradient exists across a permselective membrane at open circuit, the gradient dissipates at a rate limited by the flux of that membrane's non-favored ion (e.g. the flux of $Na^+$ across an anion-selective membrane) and osmotic effects even in the absence of a connected load.[43,49] In the artificial electric organ, this gradient dissipation is avoided when the gels are kept out of contact with one another. In the electric eel, the gradients are maintained via active transport by the $Na^+/K^+$-ATPase.[2,18]

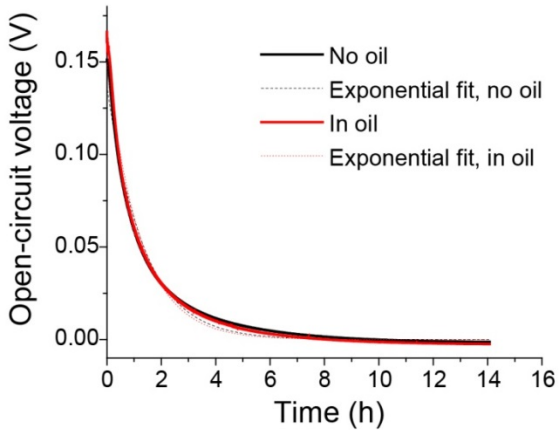


**Figure S4.2** Self-discharge of artificial electric organ over time after contact between all gels with and without exposure to ambient air. Curves were fit with a single exponential decay function (dotted curves); the half-time for each was 40 min. Video S4.1 shows a fluidic implementation of the artificial electric organ which puts gels into contact sequentially rather than simultaneously. Large-scale implementations of similar sequential positioning schemes would be prone to power loss from gradient depletion.

In order to quantify the dissipation rate of the gradients in the tetrameric hydrogel cells, we pipetted 500 µL of each gel cell component onto a single substrate and cured the solutions for 90 seconds at a distance of 12 mm, forming gel disks (diameter = 1.9 cm, height = 0.2 cm). We peeled off the gels from the substrate and placed them in a custom-built Teflon chamber which allowed us to maintain a constant force of approximately 2.2 N on our cell perpendicular to the gel-gel interfaces. We recorded the voltage across the cell in the absence of any connected load for over 12 hours. We performed one experiment open to air and one experiment in which the gel cell was completely submerged in mineral oil. Traces of voltage over time are shown in Fig. S4.2.

### S4.3. Discharging and recharging the artificial electric organ

We pipetted 500 µL of each gel cell component onto a single substrate and inserted spiral Ag/AgCl wire electrodes into both of the high-salinity reservoir solutions. We then cured the solutions for 2 min at a distance of 12 mm, forming gel disks (diameter = 1.9 cm, height = 0.2

cm). We peeled the gels off of the substrate and placed them in the Teflon chamber (section S2), and maintained a constant force through the cell of approximately 2.2 N during the discharge-recharge cycles. At the beginning of each cycle, the cell was discharged in short circuit conditions for 15 min while recording the current through the cell. We then recharged the cell with a 1 mA current for 2 min. We repeated this procedure for 10 cycles and integrated the current traces over time to calculate the capacity of the cell during each discharge. The discharge capacity (the current integrated over time during a discharge) remained above 90% of the initial discharge after ten such cycles (Fig. S4.3).

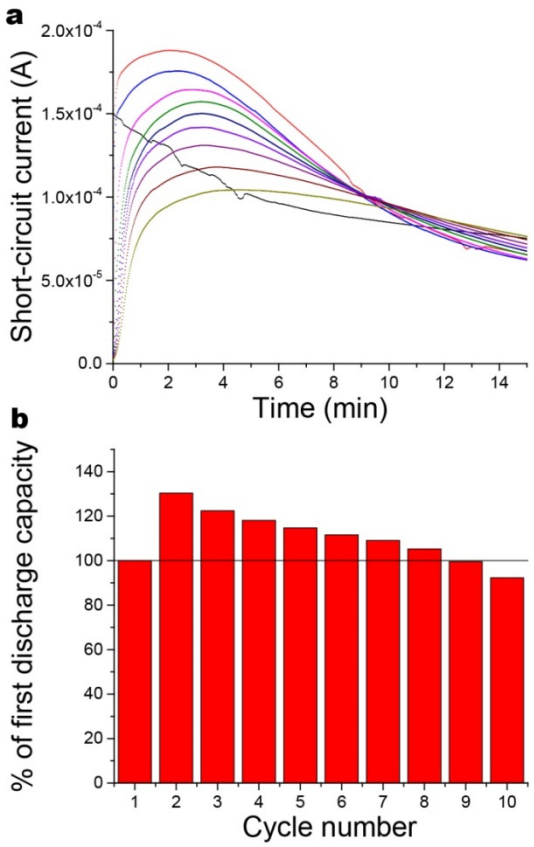


**Figure S4.3** The artificial electric organ can be recharged. **A.** Current versus time traces of ten discharges of a single tetrameric gel cell at short circuit following recharging. Initial discharge shown in black; subsequent discharges in the following order: red, blue, magenta, green, navy, purple, plum, wine, olive. **B.** Bar graph of normalized integrals of discharge curves.

**S4.4. Calculation of maximum power density of a stack of selective membranes**

*Electrophorus*' electrocytes at the peak of a discharge and the hydrogel cells of the artificial electric organ are each systems that behave approximately ohmically, which is to say that the internal resistance ($R_{int}$) of each system is practically independent of the load resistance ($R_{load}$) (see Fig. S4.4). This behavior is characterized by linear current-voltage relations as seen in Fig. 4.2C and Fig. 4.3C in the main text for gel cell systems and throughout the electrophysiology literature for *Electrophorus*[38,22,13,11] (in papers using the voltage-clamp strategy, the quadrant of interest is often reported as having positive voltage and negative current[22,38]). This line's intercept on the voltage axis is the open-circuit voltage $V_{OC}$ (V), the intercept on the current axis is the short-circuit current $I_{sc}$ (A), and the slope is the internal resistance $R_{int}$ (Ω); the three parameters are related by Ohm's law referring to a circuit where $R_{load}$ is zero (Equation S4.9).

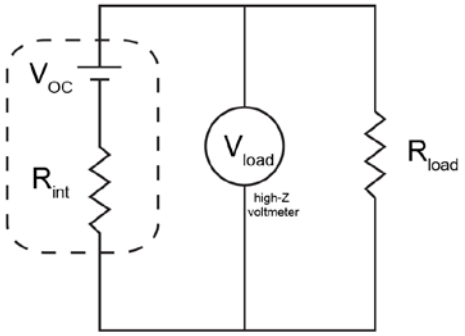


**Figure S4.4** Equivalent circuit of an artificial electric organ connected to a load resistance. The elements within the dotted line represent the contribution of a single gel cell; these can be added in series or in parallel. The impedance of the voltmeter used exceeded 10 GΩ; current through this pathway was assumed to be negligible.

$$R_{int} = -\frac{V_{OC}}{I_{sc}} \qquad \text{(S4.9)}$$

It should be noted that when current conduction occurs through an ionic pathway, $R_{int} = \rho \frac{l}{A}$ where $\rho$ is the resistivity (Ω m, a material property), $l$ is the length, and $A$ is the

cross-sectional area. The maximum power of an ionic pathway is therefore directly proportional to the cross-sectional area of that pathway and inversely proportional to its length. Maximizing the area while minimizing the length is therefore advantageous to a system's power characteristics; the ideal geometry resembles a stack of thin films. It should also be noted that the resistance of the hydrogel cell system is dominated by the reservoir gel containing the lower electrolyte concentration (0.015 M), whose resistivity is approximately 125 Ω m.

When the artificial electric organ is connected over a load,

$$P = V_{load} I = \frac{{V_{load}}^2}{R_{load}} \quad \text{(S4.10)}$$

where $P$ is the power output (W, not counting power lost to the internal resistance), $I$ is the current through the circuit, $R_{load}$ is the load resistance (Ω), and $V_{load}$ is the voltage across $R_{load}$ (V).

According to the maximum power transfer theorem, maximum power output $P_{max}$ (W) is obtained when $R_{load} = R_{int}$, the tetrameric gel cell's internal resistance (Ω). With a linear current-voltage relation, $V_{load} = V_{OC}/2$ under this condition, so

$$P_{max} = \frac{{V_{OC}}^2}{4R_{int}}. \quad \text{(S4.11)}$$

In the systems considered here, $V_{OC} = n * V_{OC,cell}$ where $n$ is the number of tetrameric gel cells in the system and $V_{OC,cell}$ is the open-circuit voltage of a single tetrameric gel cell. Likewise, $R_{int} = n * R_{int,cell}$. As a result,

$$P_{max} = \frac{{V_{OC,cell}}^2 * n}{4R_{int,cell}} \quad \text{(S4.12)}$$

To obtain the maximum power density $D_{max}$ (W m$^{-2}$ cell$^{-1}$), $P$ must be divided by the total gel area and the number of tetrameric gel cells stacked in series. If $A$ is the cross-sectional area of the stack (m$^2$) and there are four gels per cell, then:

$$D_{max} = \frac{P_{max}}{n*A} = \frac{{V_{OC,cell}}^2}{4*A*R_{int,cell}}. \quad \text{(S4.13)}$$

In the case of our 80˚ *Miura-ori* example, $V_{OC,cell}$ = 0.170 ± 0.004 V, $A$ = 0.866 cm$^2$, and $R_{int,cell}$ = 6.9 kΩ, so $D_{max}$ = 0.027 ± 0.002 W m$^{-2}$ cell$^{-1}$. This figure is presented alongside power densities calculated for *Electrophorus*' electrocytes in live eels in Table 4.1 in the main text.

**S4.5. The 45˚ *Miura-ori* fold as a printable non-planar gel setup**

In addition to the 80˚ *Miura-ori* fold presented in the main text, which required ionic conduction through holes in the substrate, we developed a printable gel cell geometry using another characteristic angle of the *Miura-ori* fold. Tesselating parallelograms with an acute angle of 45˚ form a sheet that can be folded into "mountains" and "valleys;" when compressed, the panels in the parallel valleys come into contact in a sequential series, each panel touching only the panel in front of it and the panel behind it in the series (Fig. S4.5). This geometry is amenable to patterning, as gels need only be patterned on one face of the substrate to come into contact in series (and parallel) upon folding. We printed diamond-shaped gel patterns onto the panels of laser-cut sheets before folding them (see Materials and Methods). The 45˚ fold represents a

robust, printable geometry in which an arbitrary number of parallel series of arbitrary numbers of gel cells can be patterned and automatically brought into aligned contact by manipulating one degree of mechanical freedom. However, its utility in terms of improving the maximum power output of the artificial electric organ is limited, as there is invariably a degree of lateral conduction that scales with the length of a series. When comparing a 45˚-folded artificial electric organ with a lateral analogue with panels of identical dimensions, we found that the power output was nearly identical. We attribute this to a similar lateral conduction distance through the low-salinity gel, which provides the highest resistance in the system (Fig. S4.6).

The gel precursor solutions were the same as in the printed artificial electric organ. We printed each of the gel precursors onto a single substrate that had been laser-cut with perforations in the Miura-ori pattern (45°; short edge of parallelogram = 3 cm, long edge = 4.24 cm) and corner holes corresponding to the size and position of pillars on the print plate for repeatable alignment. Before gel printing, we first printed P100 hydrophilic solution inside the parallelograms such that the hydrophilic coat ended approximately 1 mm from each perforation. We subsequently filled these parallelograms with the four gel precursor solutions using the printer (Video S4.2). The solutions were cured under the UV lamp (302 nm) at a distance of 12 mm and the substrate was folded into contact (Fig. S4.5).

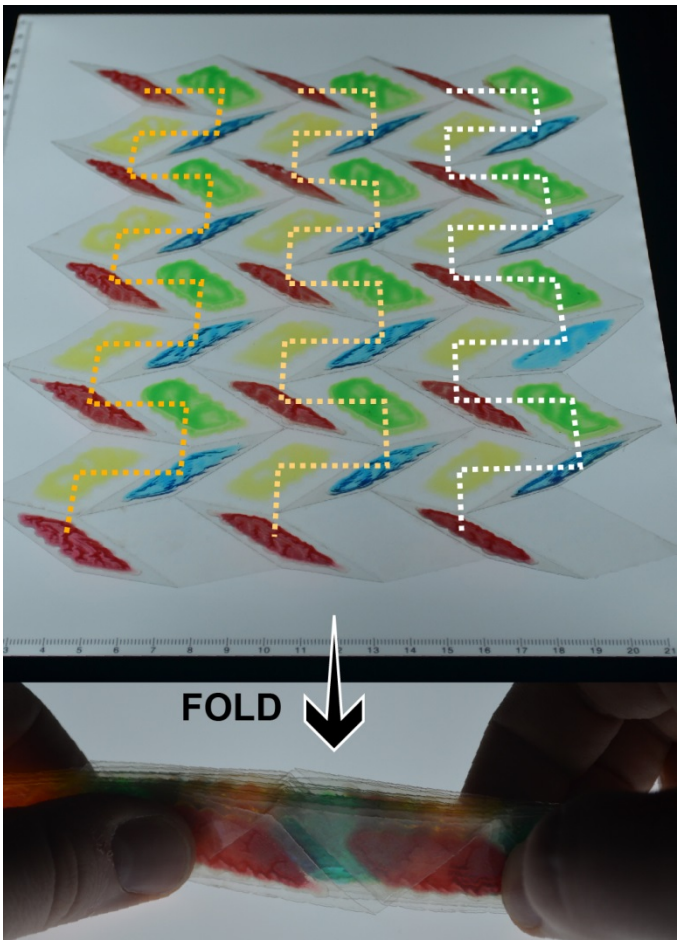


**Figure S4.5** The printed 45˚ *Miura-ori* gel cell geometry. Dotted lines of a single color indicate gels forming a series. Different colors indicate parallel sequences. This fold geometry is scalable both in series for higher voltage output and in parallel for higher current.

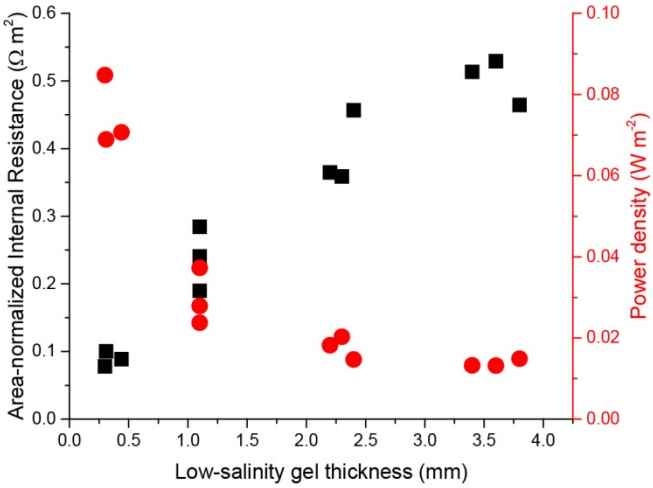


**Figure S4.6** Internal resistance (black squares) and power density (red circles) of gel cells as a function of thickness of low-salinity gel. The thicknesses of all other gels were held constant at 1 mm.

**S4.6. Ion-selective membranes enable lower resistances than charge-selective membranes**

Part of the reason that the internal resistance of tetrameric hydrogel cells is significantly higher than the internal resistance of *Electrophorus*' electrocytes (Table 4.1) can be attributed indirectly to the fact that the selective gels used in this work are broadly selective for cations or anions rather than having ion-specific selectivity. This choice was made for practical reasons: it is straightforward to imbue a hydrogel with a high cation/anion permeability ratio by including high concentrations of charged monomers in a gel framework, causing Donnan exclusion of co-ions but not counterions (see Appendix S4.1). A gel with a high selectivity between ions of the same polarity (for $Na^+$ over $K^+$, for example) is far more difficult to realize; on the other hand, this selectivity is possible in electrocyte membranes due to the presence of highly specialized monodisperse nanoscale channels. However, the ion-selectivity inherent to electrocyte membranes allows both the extracellular and intracellular compartments to contain solutions at the usual physiological ionic strength between 150 and 200 mM[12,39] while maintaining large opposing gradients of the two permeant species. The intracellular and extracellular compartments do not contribute meaningfully to the total resistance of the system, which is mostly provided by the membranes[47]. By contrast, imposing large alternating gradients of ions across broadly charge-selective membranes necessitates that one of the two reservoirs in each cell must have a low ionic strength (to illustrate this, Fig. 4.1B,D compares the ionic strengths of the compartments in electrocytes to those in gel cells). The low-salinity reservoir gel in the artificial electric organ had an ionic strength of 15 mM and provided most of the electrical resistance of each tetrameric gel cell (Fig. S4.6).

**Table S4.3**. Electrical characteristics from fluidic assembly of gel cells in series and parallel

| Cell arrangement | $V_{oc}$ (mV) | $R_{int}/L$ (kΩ/mm) |
|---|---|---|
| One cell | 143 ± 3 | 4.8 ± 0.8 |
| Three cells in series | 438 ± 5 | 14.6 ± 0.9 |
| Three cells in parallel | 143 ± 3 | 2.0 ± 0.1 |
| Three series of three cells in parallel | 423 | 4.6 |

*Internal resistance normalized by effective cell length, which accounts for differences in extent of compression. $N = 3$ for all values except final row.

## S4.7 Videos

## Video S4.1. Fluidic artificial electric organ implementation.

**Video S4.2. Printer depositing gels for serpentine implementation.**

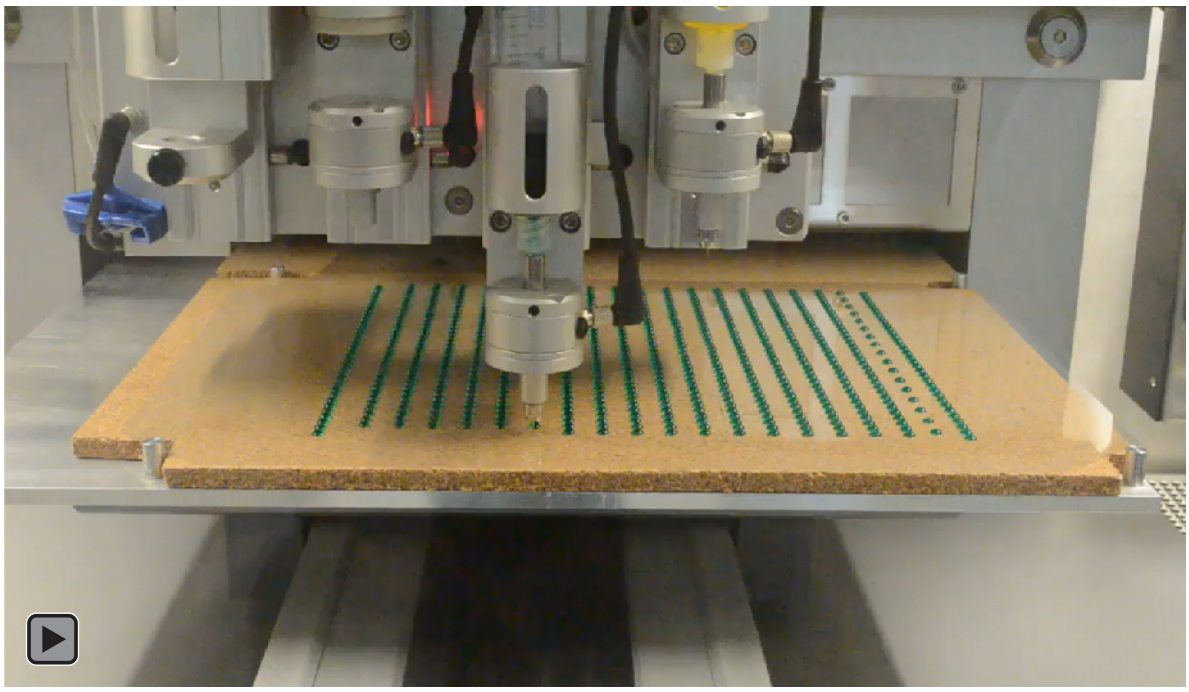

**Video S4.3. *Miura-ori* folding of a gel-bearing substrate.**

**References:**


1. Bennett, M. V. L. Electric Organs. in *Fish Physiology* (ed. Randall, W. S. H. and D. J.) **5,** 347–491 (Academic Press, 1971).

2. Gotter, A. L., Kaetzel, M. A. & Dedman, J. R. Electrophorus electricus as a model system for the study of membrane excitability. *Comp. Biochem. Physiol. A. Mol. Integr. Physiol.* **119,** 225–241 (1998).

3. Xu, J., Sigworth, F. J. & LaVan, D. A. Synthetic Protocells to Mimic and Test Cell Function. *Adv. Mater.* **22,** 120–127 (2010).

4. Sun, H., Fu, X., Xie, S., Jiang, Y. & Peng, H. Electrochemical Capacitors with High Output Voltages that Mimic Electric Eels. *Adv. Mater.* **28,** 2070–2076 (2016).

5. Kim, D.-H. *et al.* Epidermal Electronics. *Science* **333,** 838–843 (2011).

6. Whitesides, G. M. Assumptions: Taking Chemistry in New Directions. *Angew. Chem. Int. Ed.* **43,** 3632–3641 (2004).

7. Gallant, J. R. *et al.* Genomic basis for the convergent evolution of electric organs. *Science* **344,** 1522–1525 (2014).

8. Catania, K. C. Leaping eels electrify threats, supporting Humboldt's account of a battle with horses. *Proc. Natl. Acad. Sci.* **113,** 6979–6984 (2016).

9. Xu, J. & Lavan, D. A. Designing artificial cells to harness the biological ion concentration gradient. *Nat. Nanotechnol.* **3,** 666–670 (2008).

10. Brown, M. V. The electric discharge of the electric eel. *Electr. Eng.* **69,** 145–147 (1950).

11. Nachmansohn, D., Cox, R. T., Coates, C. W. & Machado, A. L. Action Potential and Enzyme Activity in the Electric Organ of Electrophorus Electricus (linnaeus): I. Choline Esterase and Respiration. *J. Neurophysiol.* **5,** 499–515 (1942).

12. Keynes, R. D. & Martins-Ferreira, H. Membrane potentials in the electroplates of the electric eel. *J. Physiol.* **119,** 315–351 (1953).

13. Cox, R. T., Coates, C. W. & Brown, M. V. Electrical Characteristics of Electric Tissue. *Ann. N. Y. Acad. Sci.* **47,** 487–500 (1946).

14. Pattle, R. E. Production of Electric Power by mixing Fresh and Salt Water in the Hydroelectric Pile. *Nature* **174,** 660–660 (1954).

15. Zeng, S., Li, B., Su, X., Qin, J. & Lin, B. Microvalve-actuated precise control of individual droplets in microfluidic devices. *Lab. Chip* **9,** 1340–1343 (2009).

16. Bardin, D. *et al.* High-speed, clinical-scale microfluidic generation of stable phase-change droplets for gas embolotherapy. *Lab. Chip* **11,** 3990–3998 (2011).

17. Young, C., Rozario, K., Serra, C., Poole-Warren, L. & Martens, P. Poly(vinyl alcohol)-heparin biosynthetic microspheres produced by microfluidics and ultraviolet photopolymerisation. *Biomicrofluidics* **7,** 044109 (2013).

18. Somló, C., Souza, W. de, Machado, R. D. & Hassón-Voloch, A. Biochemical and cytochemical localization of ATPases on the membranes of the electrocyte of Electrophorus electricus. *Cell Tissue Res.* **185,** 115–128 (1977).

19. Gumuscu, B. *et al.* Desalination by Electrodialysis Using a Stack of Patterned Ion-Selective Hydrogels on a Microfluidic Device. *Adv. Funct. Mater.* **26,** 8685–8693 (2016).

20. Cox, R. T., Rosenblith, W. A., Cutler, J. A., Mathews, R. S. & Coates, C. W. A comparison of some electrical and anatomical characteristics of the electric eel, Electrophorus electricus. *Zoologica* **25,** 553–562 (1940).

21. Miura, K. Method of Packaging and Deployment of Large Membranes in Space. *Inst. Space Astronaut. Sci.* 1–9 (1985).

22. Shenkel, S. & Sigworth, F. J. Patch recordings from the electrocytes of Electrophorus electricus. Na currents and PNa/PK variability. *J. Gen. Physiol.* **97,** 1013–1041 (1991).

23. Ide, T., Takeuchi, Y. & Yanagida, T. Development of an Experimental Apparatus for Simultaneous Observation of Optical and Electrical Signals from Single Ion Channels. *Single Mol.* **3,** 33–42 (2002).

24. Feng, J. *et al.* Single-layer MoS2 nanopores as nanopower generators. *Nature* **536,** 197–200 (2016).

25. Kopecek, J. Hydrogels: From soft contact lenses and implants to self-assembled nanomaterials. *J. Polym. Sci. Part Polym. Chem.* **47,** 5929–5946 (2009).

26. Lingley, A. R. *et al.* A single-pixel wireless contact lens display. *J. Micromechanics Microengineering* **21,** 125014 (2011).

27. Mansouri, K., Medeiros, F. A., Tafreshi, A. & Weinreb, R. N. Continuous 24-Hour Monitoring of Intraocular Pressure Patterns With a Contact Lens Sensor: Safety, Tolerability, and Reproducibility in Patients With Glaucoma. *Arch. Ophthalmol.* **130,** 1534–1539 (2012).

28. Chandrakasan, A. P., Verma, N. & Daly, D. C. Ultralow-Power Electronics for Biomedical Applications. *Annu. Rev. Biomed. Eng.* **10,** 247–274 (2008).

29. Enger, C. C. & Simeone, F. A. Biologically Energized Cardiac Pacemaker: in vivo Experience with Dogs. *Nature* **218,** 180–181 (1968).

30. Chin, S. Y. *et al.* Additive manufacturing of hydrogel-based materials for next-generation implantable medical devices. *Sci. Robot.* **2,** eaah6451 (2017).

31. Goldman, D. E. Potential, Impedance, and Rectification in Membranes. *J. Gen. Physiol.* **27,** 37–60 (1943).

32. Hodgkin, A. L. & Katz, B. The effect of sodium ions on the electrical activity of the giant axon of the squid. *J. Physiol.* **108,** 37 (1949).

33. Hille, B. *Ion Channels of Excitable Membranes*. (Sinauer Associates, Inc., 2001).

34. Grundfest, H. Comparative electrobiology of excitable membranes. *Adv Comp Physiol Biochem* **2,** 1–116 (1966).

35. Lester, H. A. Analysis of sodium and potassium redistribution during sustained permeability increases at the innervated face of Electrophorus electroplaques. *J. Gen. Physiol.* **72,** 847–862 (1978).

36. Higman, H. B., Podleski, T. R. & Bartels, E. Correlation of membrane potential and potassium flux in the electroplax of electrophorus. *Biochim. Biophys. Acta BBA - Spec. Sect. Biophys. Subj.* **79,** 138–150 (1964).

37. Karlin, A. Permeability and internal concentration of ions during depolarization of the electroplax. *Proc. Natl. Acad. Sci. U. S. A.* **58,** 1162–1167 (1967).

38. Nakamura, Y., Nakajima, S. & Grundfest, H. Analysis of spike electrogenesis and depolarizing K inactivation in electroplaques of Electrophorus electricus, L. *J. Gen. Physiol.* **49,** 321–349 (1965).

39. Schoffeniels, E. Ion Movements Studied with Single Isolated Electroplax. *Ann. N. Y. Acad. Sci.* **81,** 285–306 (1959).

40. Altamirano, M. & Coates, C. W. Effect of potassium on electroplax of electrophorus electricus. *J. Cell. Comp. Physiol.* **49,** 69–101 (1957).

41. Helfferich, F. *Ion exchange*. (McGraw-Hill, 1962).

42. Weinstein, J. N. & Leitz, F. B. Electric Power from Differences in Salinity: The Dialytic Battery. *Science* **191,** 557–559 (1976).

43. Kingsbury, R. S., Chu, K. & Coronell, O. Energy storage by reversible electrodialysis: The concentration battery. *J. Membr. Sci.* **495,** 502–516 (2015).

44. Tedesco, M. *et al.* Performance of the first reverse electrodialysis pilot plant for power production from saline waters and concentrated brines. *J. Membr. Sci.* **500,** 33–45 (2016).

45. Post, J. W. *et al.* Towards implementation of reverse electrodialysis for power generation from salinity gradients. *Desalination Water Treat.* **16,** 182–193 (2010).

46. Veerman, J., Saakes, M., Metz, S. J. & Harmsen, G. J. Reverse electrodialysis: A validated process model for design and optimization. *Chem. Eng. J.* **166,** 256–268 (2011).

47. Altamirano, M. Electrical properties of the innervated membrane of the electroplax of electric eel. *J. Cell. Comp. Physiol.* **46,** 249–277 (1955).

48. Morlock, N. L., Benamy, D. A. & Grundfest, H. Analysis of Spike Electrogenesis of Eel Electroplaques with Phase Plane and Impedance Measurements. *J. Gen. Physiol.* **52,** 22–45 (1968).

49. Veerman, J., de Jong, R. M., Saakes, M., Metz, S. J. & Harmsen, G. J. Reverse electrodialysis: Comparison of six commercial membrane pairs on the thermodynamic efficiency and power density. *J. Membr. Sci.* **343,** 7–15 (2009).

# CHAPTER 5

## Outlook

This dissertation has examined three different membrane-bound systems with the potential for use as functional, energy-transducing compartments. In Chapter 2, a polymer solution encased in a porous cellulose membrane caused an osmotic pressure gradient when submerged in pure water, which led to a buildup of hydrostatic pressure that could be used to actuate soft robots. Chapter 3 quantified permeability trends in liposomes composed of specialized extremophile-inspired lipids that may have future applications as nano-scale compartments for sensing or drug delivery. Chapter 4 presented a bio-inspired hydrogel-based setup that allowed the extraction of electrical power from ionic gradients using membranes of alternating selectivity, enabling the generation of high voltages when many unit cells were added in series. In each case, the permeability coefficient and geometry of the system had a profound effect on the kinetics of gradient equilibration, which defines the rate at which the system can perform useful work. Chapters 2 and 4 present quantitative treatments of analogous natural systems (plant extensor cells and the electric eel), which are shown to have optimal specifications for quick functional changes.

The projects presented in Chapters 3 and 4 in particular have potential for future extension; work on these topics is ongoing in our lab and in collaborating groups. Here, I will describe the scope of these efforts and discuss other possible directions for further development.

## 5.1. Directions for future work on lipid membrane systems

*Further characterization of archaea-inspired lipids*

Our colleagues in the Yang group have been continuing their investigation into archaea-inspired lipids in the context of drug encapsulation,[1,2] controlled release,[3] and further lipid design.[4–7] Major recent achievements in their work on lipid structures include the development of tethered lipids containing a central cyclohexane ring[4] and pendant cholesterol groups,[6] both of which are shown to reduce permeability to small ions compared to normal bilayer-forming lipids.

Our group has recently acquired a total internal reflectance fluorescent (TIRF) microscope, which we have begun to use to extend the simple cuvette-based assay reported in Chapter 3 into a monitoring scheme enabling the tracking over time of single liposomes tethered to a microscope slide (Figure 5.1). This approach was originally developed by Dimitrios Stamou's group at the University of Copenhagen and has been used for numerous studies of membrane biophysics and membrane protein action on a single-molecule level;[8–16] a similar approach has been demonstrated by Daniel Chiu's group at the University of Washington.[17] This system offers two primary benefits to our study of liposome membrane permeability. First, the use of a single-vesicle platform will allow us to interrogate and minimize the considerable spread to the permeability data shown in Figure 3.4. It is possible that separate fits of the decay function to individual vesicles, each with its own determined size value and calibration curve, will result in minimized error on even the first pass.

Second and more significantly, this platform allows precise temperature control over a range from 0 to 60 ˚C. As mentioned in Sections 3.1 and 3.4, the surprising result that tethering causes no apparent decrease in liposome permeability at room temperature may not extend to higher temperatures, as the results of many studies on both lipid expression and $H^+/OH^-$

permeability across a range of temperatures imply heavily that bolaamphiphilic lipids evolved to differentially slow pH gradient equilibration compared to bilayer-forming lipids at high temperatures in particular.[18–28] We intend to perform permeability studies across a range of temperatures using both the synthetic lipids discussed in Chapter 3 and a lipid extract from the thermoacidophile *Sulfolobus solfataricus*.

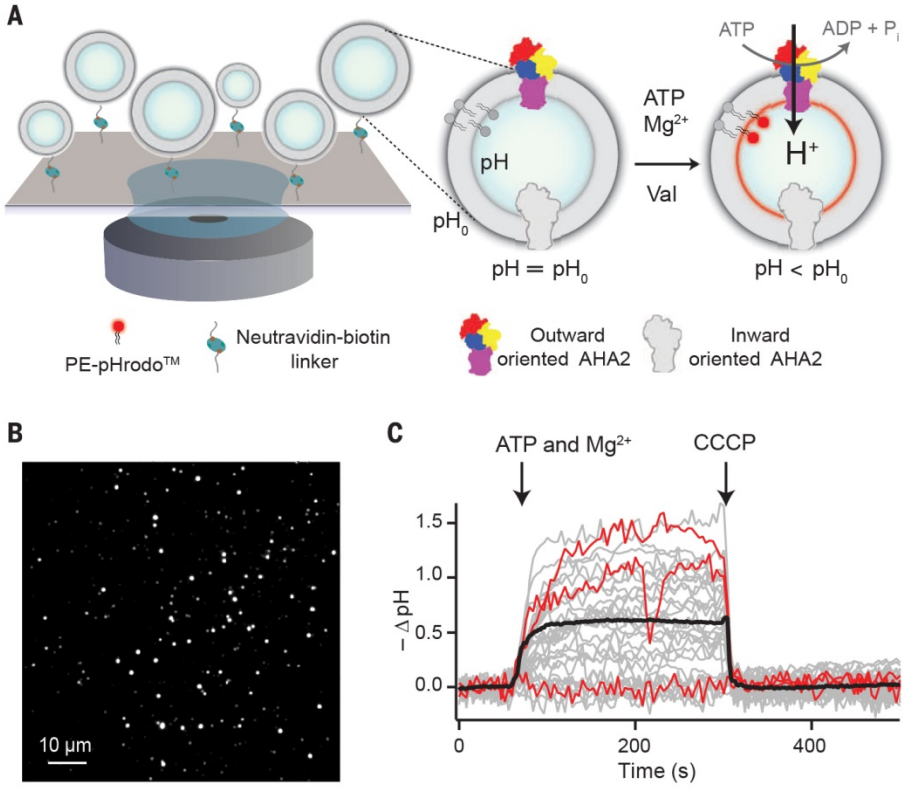


**Figure 5.1**. Liposome imaging technique based on total internal reflectance fluorescent (TIRF) microscopy. Image from Science, "Direct observation of proton pumping by a eukaryotic P-type ATPase," Veshaguri *et al*., Vol. 351, p. 1469-1473, 2016.[16] Reprinted with permission from AAAS. **A**. Tethered liposome setup for fluorescent measurement of pH changes on a single-liposome level. This image shows pH changes induced by active proton transport; our setup will measure passive proton/hydroxide permeation at various temparatures. **B**. Image of liposome array. **C**. Traces showing single vesicle pH changes over time.

*Shortcomings of liposomes as stable gradient supporters, and a suggested alternative*

This line of inquiry into the proton/hydroxide permeability of membranes with archaea-inspired lipid compositions has been an interesting foray into fundamental biophysics research, but this aspect was not the original application our group imagined for these lipids, which we erroneously hypothesized would form uniquely ion-impermeable membranes. Our original vision was to encapsulate redox-active ions in small unilamellar vesicles (SUVs) of these lipids in a gel on a test strip, which would also contain chemically-activated engineered ion channels of the type previously reported by our lab and the Yang group.[29–33] Upon exposure to a patient sample containing a small-molecule, macromolecular, or enzymatic biomarker, the ion channels would permeabilize the compartments, allowing the electrochemical detection of a disease state.

While the idea of a self-powered sensing platform using engineered ion channels to trigger gradient equilibration is attractive, the use of SUVs as a gradient-bearing architecture in this context is problematic in four main ways. First, passive ion permeation rates of lipid membranes are nontrivial, so a system which contains built-in gradients has a limited shelf life. Second, lipid membranes are susceptible to oxidation, so the proposed encapsulation of oxidizing metal ions limits this shelf life further by creating a self-degrading system. Third, SUVs have a high surface-area-to-volume ratio, speeding their equilibration. Finally, given that the potential produced by redox reactions on an electrode is proportional to the logarithm of the concentration according to the Nernst equation, the magnitude of the signal is severely limited by the construction of the system. In a solution of small unilamellar vesicles, the total encapsulated volume is typically on the order to 0.1% - 1% of the total system volume;[34] if the SUVs were laden with even a high concentration of redox-active ions, the effect on the concentration of the

bulk solution would be small and difficult to distinguish from the substantial leak mentioned above.

In order to circumvent these problems, I suggest the use of another lipid membrane-based strategy, the formation of droplet-interface bilayers (DIBs) at the point of care as demonstrated in Figure 5.2. Droplet-interface bilayers, first developed by Needham, Bayley,[35,36] Takeuchi,[37] and Tsofina[38] and since used to exploit the capabilities of lipid membrane-based molecular machines in a wide variety of contexts,[39–44] have none of these issues. In the proposed scheme (Figure 5.2), a patient sample is first mixed with a pH-sensitive dye and a pore-forming peptide whose activation can be triggered by competitive antibody binding or enzymatic activity. This mixture is added as one of two aqueous phases of a DIB; the other has a different pH, and equilibration will trigger a color change in the pH-sensitive dye. In this setup, the gradient and the bilayer are established at the same time, which is also the moment when the patient sample is introduced, so there should be no concerns about shelf life. The permeating species, protons, causes no damage to phospholipid membranes. Finally, the relative volumes of the aqueous compartments can be changed at will, and the signal is visual and clearly visible, so any concerns about its resolvability can be allayed by modifying the magnitude of the pH gradient and the concentration and identity of the reporting dye. The use of DIBs in conjunction with engineered ion channels was first proposed by Poulos *et al*. in the context of a high-throughput platform based on electrical recordings.[45]

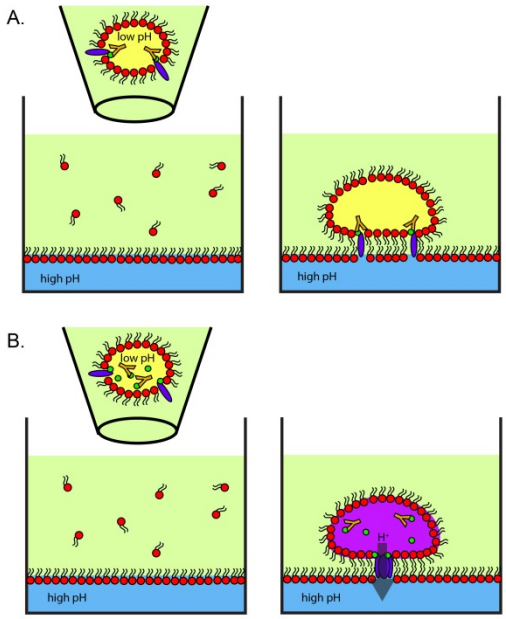


**Figure 5.2** Droplet interface bilayer (DIB)-based platform for analyte detection using engineered ion channels. A patient sample is pre-processed by mixing with a solution containing antibodies selective for a biomarker of interest, a biomarker-conjugated pore-forming peptide, and a pH-sensitive dye, then introduced as a droplet into an oil phase containing lipids and allowed to form a DIB with an aqueous phase at a different pH. **A**. In a patient sample lacking the biomarker, the antibodies prevent the formation of active pores. **B**. In a patient sample containing the biomarker, the biomarker out-competes the pore-former from the antibody's binding sites, freeing it to form pores that allow pH gradient equilibration, producing a visible signal.

We have begun early work on a DIB-based assay with a visual detection mode employing pH-sensitive dyes (Figure 5.2); however, repeatability issues involving bilayer formation and stability led to the project being shelved. It is clear that most DIB systems, whose bilayers are monitored electrically, benefit significantly from the mechanical and electrical control that electrodes provide as a bilayer is being formed. We recently received advice from Tae-Joon Jeon, an author of a particularly relevant journal article about a DIB-based high-throughput screening platform,[45] that using an oil phase less viscous than squalene and droplets larger than 0.5 µL (our previous experimental parameters) would more likely lead to bilayer formation; implementing this advice may make subsequent attempts more successful.

## 5.2 Directions for future work on the artificial electric organ

*Application development*

The artificial electric organ is exciting predominantly because of the characteristics it displays that conventional batteries do not: it is transparent, flexible, and potentially biocompatible, using no harmful electrochemical products or processes. As a result, its most interesting use cases are small-scale applications in which the use of a traditional battery would be difficult or undesirable. The most readily apparent application space in this category is that of wearable and implantable devices. As a basic example, pacemakers currently operate with power consumption under 10 μW,[46] the output of under 4 $cm^2$ of layered gel in the implementation described in Chapter 4. As research into next-generation medical implants and interest in "the internet of bio-nano things" continues to develop,[47,48] however, ultralow-power devices that monitor vital signs, detect disease states, and aid in therapies may proliferate if enabled by suitable power sources. Currently, the power schemes being considered for these applications[49] include near-field[50] or RF inductive coupling,[51] which both rely on an external power source and limit implant depth, and piezo- or triboelectric power generators,[52–54] which must be coupled to a mechanical actuation process in the body or powered externally using ultrasound.[55]

In Chapter 4, the artificial electric organ was mechanically actuated. However, gel-based RED setups can in theory be recharged in two ways: through an electrodialytic process by driving a current (see Section S4.3) or by rebuilding the electrolyte gradients via mass transfer to or from external sources. As a result, gel-based RED presents the enticing prospect of harnessing electrical power from natural electrolyte gradients between biological fluids, which may lead to a steady-state application with the ability to exploit physiological homeostatic mechanisms to transduce metabolic energy into different forms of usable work inside the body in a continuous

and long-term fashion. If successfully implemented, this aspect would be unique among the currently developing power strategies for implantable devices.

Clearly, a massive amount of feasibility evaluation, engineering, prototyping, and clinical testing would be necessary if such an idea were ever to approach reality, though the sophistication of today's MEMS and microfluidic technologies may make this future closer than one might think. A full account of the relevant factors is beyond the scope of this dissertation, which merely presents the gel-based reverse electrodialytic energy transduction system. One of the most pertinent considerations, however, is the driving gradient. Suitable bodily fluids – preferably expendable ones – must be identified with large differences in their concentration of small ions. Alternatively, depending on the application, induced gradient sources should also be considered; for example, a design involving the concentration of tears by evaporation at the eye surface could be useful for the "contact lens" implementation presented in Figure 4.4C. Advances in microfluidics could be used for the development of such gradients.

As a side note, two caveats must be taken into account when considering the artificial electric organ as reported here. First, the monomer solutions used here each contained acrylamide and N,N'-methylenebisacrylamide. In the polymerized form, these are not harmful, but the monomers are toxic, and some unreacted monomer can be expected to remain in solution. In an implantable implementation of this scheme, a base polymer with nontoxic monomers must be used. Second, the system as presented is not entirely free of electrochemistry, as it was always interrogated with Ag/AgCl electrodes at the terminal gels. Intriguingly, however, some recently developed gel-based actuators may not require metal leads to be connected to an artificial electric organ.[56]

*Minimizing resistance*

In the near term, we plan on characterizing the sources of impedance in the artificial electric organ in greater depth using electrochemical impedance spectroscopy (EIS) in response to recent reviewer comments on a submitted manuscript. Prior literature on EIS across ion exchange membranes indicates that we can expect a purely resistive component to the impedance attributable to the gels themselves and the solution within them, as well as a more complex contribution with capacitive components that can be attributed to the boundary layers that form in the selective gels.[57,58] The results of this characterization will help us minimize the overall impedance of the system for a higher power output.

Clearly, one obvious way to minimize the resistance per cell of the artificial electric organ setup is to devise a fabrication strategy for thinner hydrogel films. Numerous techniques for creating thin hydrogel films are known,[59] such as spin-coating monomers onto a surface with a radical initiator and a cross-linking agent,[60,61] using plasma deposition to simultaneously deposit and polymerize a film,[62,63] the self-assembly of block copolymers into a film,[64] and using "layer-by-layer" adsorption of oppositely charged organic chains (though this last strategy would likely not be suitable for hydrogels with immobilized charges of the same sign).[65] However, one difficulty we circumvented by using thicker films is the loss of water from the system via evaporation on time scales relevant to measurement. Making the films thinner than hundreds of microns will likely result in problematic dehydration.

Beyond this step, our expectation is that most of the impedance in the system comes from the compartment gel with lower salinity; as a result, any efforts to minimize the total overall resistance should focus on the low-salinity component. One result demonstrating this can be seen in Figure S4.6, which shows the resistance of a tetrameric gel cell as a function of the thickness

of the low-salinity compartment. Extrapolation from the black points on this graph to the (left) y-axis indicates that the total resistance of all the other gels combined is likely less than 0.05 $\Omega$ $m^2$, or less than 20% of the total resistance of any system investigated in this work. As discussed in Section 4.6, the eel's electric organ is a reverse electrodialytic system that maintains high ionic strengths in each compartment while preserving electroneutrality by using a cation-cation flux pair (as opposed to the cation-anion pair of sodium and chloride used in both traditional reverse electrodialysis and the artificial electric organ presented here). This is only possible because the exquisite selectivity of ion channels allows electrocyte membranes to differentiate between monatomic cations, with permeability ratios from tens to over one hundred (Table S4.1). As such, another future direction that would greatly benefit the development of this work would be the development of membranes that select for specific ions rather than for charge.

One means of accomplishing this could involve incorporating selective ionophores – either peptides such as valinomycin or synthetic coordinating compounds such as crown ethers or cryptands – into polymer membranes. A wide variety of ionophore-bearing polymer membranes have been developed for decades in the context of "ion-selective electrodes" used in analytical chemistry labs to determine the ionic composition of an electrolyte solution.[66,67] Using ionophores to impart selectivity for specific ions would enable the use of solutions of high ionic strength in both reservoirs, lowering the resistance of the system. The membranes, which are hydrophobic in the context of ion-selective electrodes, would likely have a higher impedance than selective hydrogels, so this scheme would likely require high ionophore concentrations and small thicknesses in order to produce a net benefit. To this end, lipid membrane-based gradient power generation platforms such as the DIB "protocells" presented by Xu *et al.* could be revisited,[68,69] though the utility of these systems may be hamstrung by the limits in mechanical

robustness and maximum area inherent to lipid membranes. In either case, however, such ion-specific membranes could greatly expand the scope of possible source biofluids for the implantable device application of the artificial electric organ, as gradients of specific ions within the body are far more plentiful than gradients of total ionic strength.

### 5.3 Final words

Given their ubiquity and utility as energy transducers in nature, semipermeable membranes should be considered as a fundamentally useful element in the design of systems that interact with gradients of various intensive quantities. The studies presented here vary widely in their scale and applications, demonstrating the versatility of this motif. Simple mass transfer has no harmful components or byproducts, unlike power generation and energy storage methods based on combustion or batteries. The renewability and safety of membrane-based energy transduction schemes at all scales makes them attractive in many contexts despite relatively low power densities; further engineering and study may prove such methods viable as distributed energy sources.

**References**:


1. Leriche, G. *et al.* Characterization of drug encapsulation and retention in archaea-inspired tetraether liposomes. *Org. Biomol. Chem.* **15,** 2157–2162 (2017).

2. Paolucci, V., Leriche, G., Koyanagi, T. & Yang, J. Evaluation of tetraether lipid-based liposomal carriers for encapsulation and retention of nucleoside-based drugs. *Bioorg. Med. Chem. Lett.* **27,** 4319–4322 (2017).

3. Koyanagi, T. *et al.* Thiol-Triggered Release of Intraliposomal Content from Liposomes Made of Extremophile-Inspired Tetraether Lipids. *Bioconjug. Chem.* **28,** 2041–2045 (2017).

4. Koyanagi, T. *et al.* Cyclohexane Rings Reduce Membrane Permeability to Small Ions in Archaea-Inspired Tetraether Lipids. *Angew. Chem.* **128,** 1922–1925 (2016).

5. Koyanagi, T. *et al.* Effect of Headgroups on Small-Ion Permeability across Archaea-Inspired Tetraether Lipid Membranes. *Chem. – Eur. J.* **22,** 8074–8077 (2016).

6. Koyanagi, T. *et al.* Hybrid Lipids Inspired by Extremophiles and Eukaryotes Afford Serum-Stable Membranes with Low Leakage. *Chem. – Eur. J.* **23,** 6757–6762 (2017).

7. Koyanagi, T. Design and Synthesis of Archaea-inspired Tetraether Lipids. *eScholarship* (2017).

8. Stamou, D., Duschl, C., Delamarche, E. & Vogel, H. Self-Assembled Microarrays of Attoliter Molecular Vessels. *Angew. Chem.* **115,** 5738–5741 (2003).

9. Christensen, S. M. & Stamou, D. Surface-based lipidvesicle reactor systems: fabrication and applications. *Soft Matter* **3,** 828–836 (2007).

10. Hatzakis, N. S. *et al.* Single Enzyme Studies Reveal the Existence of Discrete Functional States for Monomeric Enzymes and How They Are “Selected” upon Allosteric Regulation. *J. Am. Chem. Soc.* **134,** 9296–9302 (2012).

11. Kunding, A. H., Mortensen, M. W., Christensen, S. M. & Stamou, D. A Fluorescence-Based Technique to Construct Size Distributions from Single-Object Measurements: Application to the Extrusion of Lipid Vesicles. *Biophys. J.* **95,** 1176–1188 (2008).

12. Larsen, J., Hatzakis, N. S. & Stamou, D. Observation of Inhomogeneity in the Lipid Composition of Individual Nanoscale Liposomes. *J. Am. Chem. Soc.* **133,** 10685–10687 (2011).

13. Lohse, B., Bolinger, P.-Y. & Stamou, D. Encapsulation Efficiency Measured on Single Small Unilamellar Vesicles. *J. Am. Chem. Soc.* **130,** 14372–14373 (2008).

14. Mathiasen, S. *et al.* Nanoscale high-content analysis using compositional heterogeneities of single proteoliposomes. *Nat. Methods* **11,** 931–934 (2014).

15. Tonnesen, A., Christensen, S. M., Tkach, V. & Stamou, D. Geometrical Membrane Curvature as an Allosteric Regulator of Membrane Protein Structure and Function. *Biophys. J.* **106,** 201–209 (2014).

16. Veshaguri, S. *et al.* Direct observation of proton pumping by a eukaryotic P-type ATPase. *Science* **351,** 1469–1473 (2016).

17. Kuyper, C. L., Kuo, J. S., Mutch, S. A. & Chiu, D. T. Proton Permeation into Single Vesicles Occurs via a Sequential Two-Step Mechanism and Is Heterogeneous. *J. Am. Chem. Soc.* **128,** 3233–3240 (2006).

18. Komatsu, H. & Chong, P. L. Low permeability of liposomal membranes composed of bipolar tetraether lipids from thermoacidophilic archaebacterium Sulfolobus acidocaldarius. *Biochemistry (Mosc.)* **37,** 107–115 (1998).

19. van de Vossenberg, J. L. C. M., Driessen, A. J. M., Grant, D. & Konings, W. N. Lipid membranes from halophilic and alkali-halophilic Archaea have a low H+ and Na+ permeability at high salt concentration. *Extremophiles* **3,** 253–257 (1999).

20. van de Vossenberg, J. L. C. M., Ubbink-Kok, T., Elferink, M. G. L., Driessen, A. J. M. & Konings, W. N. Ion permeability of the cytoplasmic membrane limits the maximum growth temperature of bacteria and archaea. *Mol. Microbiol.* **18,** 925–932 (1995).

21. Sprott, G. D., Meloche, M. & Richards, J. C. Proportions of diether, macrocyclic diether, and tetraether lipids in Methanococcus jannaschii grown at different temperatures. *J. Bacteriol.* **173,** 3907–3910 (1991).

22. Langworthy, T. A. [52] Lipids of Thermoplasma. in *Methods in Enzymology* **88,** 396–406 (Academic Press, 1982).

23. Svobodová, J. & Svoboda, P. Membrane fluidity inBacillus subtilis. Physical change and biological adaptation. *Folia Microbiol. (Praha)* **33,** 161 (1988).

24. Prado, A., Da Costa, M. S. & Madeira, V. M. C. Effect of Growth Temperature on the Lipid Composition of two Strains of Thermus sp. *Microbiology* **134,** 1653–1660 (1988).

25. Reizer, J., Grossowicz, N. & Barenholz, Y. The effect of growth temperature on the thermotropic behavior of the membranes of a thermophilic Bacillus. Composition-structure-function relationships. *Biochim. Biophys. Acta BBA - Biomembr.* **815,** 268–280 (1985).

26. Uda, I., Sugai, A., Itoh, Y. H. & Itoh, T. Variation in Molecular Species of Core Lipids from the Order *Thermoplasmales* Strains Depends on the Growth Temperature. *J. Oleo Sci.* **53,** 399–404 (2004).

27. De Rosa, M., Esposito, E., Gambacorta, A., Nicolaus, B. & Bu'Lock, J. D. Effects of temperature on ether lipid composition of Caldariella acidophila. *Phytochemistry* **19,** 827–831 (1980).

28. De Rosa, M. & Gambacorta, A. The lipids of archaebacteria. *Prog. Lipid Res.* **27,** 153–175 (1988).

29. Blake, S., Mayer, T., Mayer, M. & Yang, J. Monitoring Chemical Reactions by Using Ion-Channel-Forming Peptides. *ChemBioChem* **7,** 433–435 (2006).

30. Mayer, M., Semetey, V., Gitlin, I., Yang, J. & Whitesides, G. M. Using Ion Channel-Forming Peptides to Quantify Protein−Ligand Interactions. *J. Am. Chem. Soc.* **130,** 1453–1465 (2008).

31. Blake, S., Capone, R., Mayer, M. & Yang, J. Chemically Reactive Derivatives of Gramicidin A for Developing Ion Channel-Based Nanoprobes. *Bioconjug. Chem.* **19,** 1614–1624 (2008).

32. Capone, R., Blake, S., Restrepo, M. R., Yang, J. & Mayer, M. Designing nanosensors based on charged derivatives of gramicidin A. *J. Am. Chem. Soc.* **129,** 9737–9745 (2007).

33. Macrae, M. X. *et al.* A Semi-Synthetic Ion Channel Platform for Detection of Phosphatase and Protease Activity. *ACS Nano* **3,** 3567–3580 (2009).

34. Szoka, F. & Papahadjopoulos, D. Comparative Properties and Methods of Preparation of Lipid Vesicles (Liposomes). *Annu. Rev. Biophys. Bioeng.* **9,** 467–508 (1980).

35. Bayley, H. *et al.* Droplet interface bilayers. *Mol. Biosyst.* **4,** 1191 (2008).

36. Holden, M. A., Needham, D. & Bayley, H. Functional Bionetworks from Nanoliter Water Droplets. *J. Am. Chem. Soc.* **129,** 8650–8655 (2007).

37. Funakoshi, K., Suzuki, H. & Takeuchi, S. Lipid Bilayer Formation by Contacting Monolayers in a Microfluidic Device for Membrane Protein Analysis. *Anal. Chem.* **78,** 8169–8174 (2006).

38. Tsofina, L. M., Liberman, E. A. & Babakov, A. V. Production of Bimolecular Protein-Lipid Membranes in Aqueous Solution. *Nature* **212,** 681–683 (1966).

39. Szabo, M. & Wallace, M. I. Imaging potassium-flux through individual electropores in droplet interface bilayers. *Biochim. Biophys. Acta BBA - Biomembr.* **1858,** 613–617 (2016).

40. Castell, O. K., Berridge, J. & Wallace, M. I. Quantification of Membrane Protein Inhibition by Optical Ion Flux in a Droplet Interface Bilayer Array. *Angew. Chem. Int. Ed.* **51,** 3134–3138 (2012).

41. Tonooka, T., Sato, K., Osaki, T., Kawano, R. & Takeuchi, S. Lipid Bilayers on a Picoliter Microdroplet Array for Rapid Fluorescence Detection of Membrane Transport. *Small* **10,** 3275–3282 (2014).

42. Baxani, D. K. *et al.* Bilayer Networks within a Hydrogel Shell: A Robust Chassis for Artificial Cells and a Platform for Membrane Studies. *Angew. Chem. Int. Ed.* **55,** 14240–14245 (2016).

43. Villar, G. & Bayley, H. Functional Droplet Interface Bilayers. in *Encyclopedia of Biophysics* (ed. Roberts, G. C. K.) 861–868 (Springer Berlin Heidelberg, 2013).

44. Heron, A. J., Thompson, J. R., Mason, A. E. & Wallace, M. I. Direct Detection of Membrane Channels from Gels Using Water-in-Oil Droplet Bilayers. *J. Am. Chem. Soc.* **129,** 16042–16047 (2007).

45. Poulos, J. L. *et al.* Ion channel and toxin measurement using a high throughput lipid membrane platform. *Biosens. Bioelectron.* **24,** 1806–1810 (2009).

46. Chandrakasan, A. P., Verma, N. & Daly, D. C. Ultralow-Power Electronics for Biomedical Applications. *Annu. Rev. Biomed. Eng.* **10,** 247–274 (2008).

47. Akyildiz, I. F., Pierobon, M., Balasubramaniam, S. & Koucheryavy, Y. The internet of Bio-Nano things. *IEEE Commun. Mag.* **53,** 32–40 (2015).

48. Ali, N. A. & Abu-Elkheir, M. Internet of nano-things healthcare applications: Requirements, opportunities, and challenges. in *2015 IEEE 11th International Conference on Wireless and Mobile Computing, Networking and Communications (WiMob)* 9–14 (2015). doi:10.1109/WiMOB.2015.7347934

49. Lundager, K., Zeinali, B., Tohidi, M., Madsen, J. K. & Moradi, F. Low Power Design for Future Wearable and Implantable Devices. *J. Low Power Electron. Appl.* **6,** 20 (2016).

50. Sauer, C., Stanacevic, M., Cauwenberghs, G. & Thakor, N. Power harvesting and telemetry in CMOS for implanted devices. *IEEE Trans. Circuits Syst. Regul. Pap.* **52,** 2605–2613 (2005).

51. Heetderks, W. J. RF powering of millimeter- and submillimeter-sized neural prosthetic implants. *IEEE Trans. Biomed. Eng.* **35,** 323–327 (1988).

52. Jie, Y., Jiang, Q., Zhang, Y., Wang, N. & Cao, X. A structural bionic design: From electric organs to systematic triboelectric generators. *Nano Energy* **27,** 554–560 (2016).

53. Jung, W.-S. *et al.* High Output Piezo/Triboelectric Hybrid Generator. *Sci. Rep.* **5,** srep09309 (2015).

54. Fan, F. R., Tang, W. & Wang, Z. L. Flexible Nanogenerators for Energy Harvesting and Self-Powered Electronics. *Adv. Mater.* **28,** 4283–4305 (2016).

55. Kawanabe, H., Katane, T., Saotome, H., Saito, O. & Kobayashi, K. Power and Information Transmission to Implanted Medical Device Using Ultrasonic. *Jpn. J. Appl. Phys.* **40,** 3865 (2001).

56. Keplinger, C. *et al.* Stretchable, transparent, ionic conductors. *Science* **341,** 984–987 (2013).

57. Długołęcki, P. *et al.* On the resistances of membrane, diffusion boundary layer and double layer in ion exchange membrane transport. *J. Membr. Sci.* **349,** 369–379 (2010).

58. Park, J.-S., Choi, J.-H., Woo, J.-J. & Moon, S.-H. An electrical impedance spectroscopic (EIS) study on transport characteristics of ion-exchange membrane systems. *J. Colloid Interface Sci.* **300,** 655–662 (2006).

59. Tokarev, I. & Minko, S. Stimuli-responsive hydrogel thin films. *Soft Matter* **5,** 511–524 (2009).

60. Zheng, J., Odake, T., Kitamori, T. & Sawada, T. Miniaturized Ultrathin Slab Gel Electrophoresis with Thermal Lens Microscope Detection and Its Application to Fast Genetic Diagnosis. *Anal. Chem.* **71,** 5003–5008 (1999).

61. Harmon, M. E., Jakob, T. A. M., Knoll, W. & Frank, C. W. A Surface Plasmon Resonance Study of Volume Phase Transitions in N-Isopropylacrylamide Gel Films. *Macromolecules* **35,** 5999–6004 (2002).

62. Tamirisa, P. A. & Hess, D. W. Water and Moisture Uptake by Plasma Polymerized Thermoresponsive Hydrogel Films. *Macromolecules* **39,** 7092–7097 (2006).

63. Pan, Y. V., Wesley, R. A., Luginbuhl, R., Denton, D. D. & Ratner, B. D. Plasma Polymerized N-Isopropylacrylamide: Synthesis and Characterization of a Smart Thermally Responsive Coating. *Biomacromolecules* **2,** 32–36 (2001).

64. Nykänen, A. *et al.* Phase Behavior and Temperature-Responsive Molecular Filters Based on Self-Assembly of Polystyrene-block-poly(N-isopropylacrylamide)-block-polystyrene. *Macromolecules* **40,** 5827–5834 (2007).

65. Sukhishvili, S. A. Responsive polymer films and capsules via layer-by-layer assembly. *Curr. Opin. Colloid Interface Sci.* **10,** 37–44 (2005).

66. Bakker, E., Bühlmann, P. & Pretsch, E. Carrier-Based Ion-Selective Electrodes and Bulk Optodes. 1. General Characteristics. *Chem. Rev.* **97,** 3083–3132 (1997).

67. Bühlmann, P., Pretsch, E. & Bakker, E. Carrier-Based Ion-Selective Electrodes and Bulk Optodes. 2. Ionophores for Potentiometric and Optical Sensors. *Chem. Rev.* **98,** 1593–1688 (1998).

68. Xu, J., Sigworth, F. J. & LaVan, D. A. Synthetic Protocells to Mimic and Test Cell Function. *Adv. Mater.* **22,** 120–127 (2010).

69. Xu, J., Vanderlick, T. K. & LaVan, D. A. Energy Conversion in Protocells with Natural Nanoconductors. *Int. J. Photoenergy* **2012,** e425735 (2011).